RUPRECHT-KARLS-UNIVERSITÄT HEIDELBERG

Nadia Bludau

# Calibration of Jets at Trigger-Level for a Low Mass Dijet Search at ATLAS

Masterarbeit

HD-KIP-17-48

KIRCHHOFF-INSTITUT FÜR PHYSIK

Department of Physics and Astronomy

University of Heidelberg

Master thesis

in Physics

submitted by

Nadia Bludau

born in Lünen

2017

# Calibration of Jets at Trigger-Level

# for a Low Mass Dijet Search at ATLAS

This Master thesis has been carried out by Nadia Bludau

at the

Kirchhoff-Institute for Physics

under the supervision of

Dr Monica Dunford

**Abstract**

The Trigger-object Level Analysis (TLA) is a dijet-analysis that searches for resonances in the low mass dijet spectrum. Due to the large contribution of quantum chromodynamics processes, the data recording rate of dijet events with masses below 1 TeV is limited. Hence, the sensitivity of low mass dijet searches is limited. To increase the data read out rate, the TLA exploits a new data taking strategy, which records information about jets reconstructed at trigger level only. But due to the reduced information, the well established ALTAS jet calibration scheme has to be modified to a TLA calibration scheme to be applicative to the jets used in the TLA. In this thesis, the TLA calibration scheme for jets at trigger level is discussed. It is shown that the energies of the jets calibrated using the TLA calibration scheme are within a 1% agreement with the energies of jets calibrated using the established ATLAS calibration scheme. The resolution is shown to be within the same order of magnitude and no large additional uncertainties for the jet energies arise due to the TLA calibration scheme.

**Zusammenfassung**

Die Trigger-Objekt Level Analyse (TLA) ist eine Dijet Analyse, die nach Resonanzen im niedrigen Dijet Massenspektrum sucht. Da im niedrigen Massenspektrum eine großen Anzahl an Quantenchromodynamik Ereignissen erwartet wird, ist die Archivierungsrate für Ereignisse mit Massen niedriger als 1 TeV limitiert. Dadurch wird die erreichbare Sensitivität einer Dijet Analyse bei entsprechenden Massen eingeschränkt. Um die Sensitivität zu erhöhen, nutzt die TLA eine neue Datennahmen Strategie, die die Datenmenge pro Ereignis reduziert. Die gepeicherten Informationen beschränken sich auf Jets, die auf Trigger Ebene rekonstruiert werden. Dadurch muss das etablierte ATLAS Kalibrierungsverfahren verändert werden, welches zusätzliche Informationen über ein Ereignis benötigt. Das TLA Kalibrierungsverfahren ergibt sich aus diesen Veränderungen. In dieser Masterarbeit werden das TLA Kalibrierungsverfahren und Studien zu dessen Validierung vorgestellt. Es stellt sich heraus, dass die Energien der Jets, die nach dem TLA Kalibrierungsverfahren kalibriert wurden, innerhalb 1% mit den Energien der Jets übereinstimmen, die nach dem etablierten ATLAS Verfahren kalibriert wurden. Die Energieauflösungen befinden sich innerhalb der selben Größenordnung und keine größeren Unsicherheiten werden den Energien der Jets durch das neue Kalibrierungsverfahren hinzugefügt.

# Contents

# Chapter 1

# Motivation and Theory

The Standard Model of particle physics (SM) is a mathematical description of all fundamental particles known to date. And while it predicts almost all measurements with high precision, a couple of observations are not explained. These observations can only be explained with new theories, with physics beyond the SM.
The Large Hadron Collider (LHC) is a particle accelerator, which accelerates protons and causes them to collide at a rate of 1 MHz and with a center-of-mass energy of 13 TeV. These conditions allow high precision tests for SM predictions as well as new theories. However, an event rate of 1 MHz is with current technical standard not processable. The ATLAS detector, one of four experiments located at the LHC, manages to process a total event rate of 1 kHz.
Because of this bandwidth limitation, the number of events that is recorded has to be restricted in certain energy ranges. As most new theories predict new particles with high masses, lower energetic events are restricted by a prescale rate in the trigger system. Especially events containing only strong interacting particles, which are reconstructed as jets, with a transverse momentum below 300 GeV, have a high prescale rate. Consequently, the event rate is too low to set stronger limits on theories predicting a new low mass particle with a respective coupling to jets. Only since last year, new searches are performed that exploit different techniques to reach these regions.
One of these searches is the Trigger-object Level Analysis (TLA). It uses only partial event information so that the amount of data to be stored is reduced. This allows to increase the event recording rate. The drawback is that the reduced amount of information complicates jet calibration and the jet reconstruction after data-taking is not feasible. Instead the TLA exploits jets reconstructed with the high-level trigger during data-taking, so called jets at trigger level or "HLT jets".
In this thesis, the new technique of the TLA is presented and the analysis procedure discussed. The TLA calibration scheme for HLT jets is introduced for the analysis performed on data taken in 2016, which expands the calibration scheme applied to data taken in 2015. The single steps are explained and the performance of the calibration is validated.

This thesis is structured as followed: This chapter introduces the SM with special focus on the jet production in proton-proton collisions. In addition, a short introduction into dark matter and a simplified benchmark model predicting a low mass particle is presented. Chapter 2 introduces

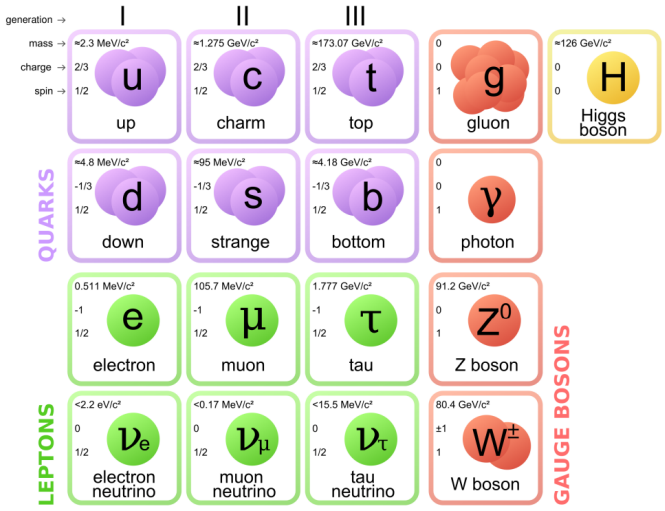


**Figure 1.1:** The fundamental particles of the Standard Model of particle physics and their characteristics. Taken from [29].

the experimental set-up: the Large Hadron Collider and the ATLAS detector. Chapter 3 describes the the standard ATLAS reconstruction and calibration scheme for jets, and quality selections. In chapter 4 a short overview of the MC simulation and different data samples used in this thesis is given. Chapter 5 presents the TLA performed on data taken in 2015 (2015 TLA), including calibration scheme for HLT jets and results. In chapter 6 the differences between HLT and standard ATLAS jet reconstruction and quality selections are listed. Chapter 7 describes the TLA calibration scheme performed on data taken in 2016 (2016 TLA) and its validation. Finally, a short summary of the thesis is given in chapter 8.

## 1.1 Quantum Chromodynamics and Jet Production in Proton-Proton Collisions

The Standard Model of particle physics is an effective mathematical description of the fundamental particles and their interactions. It is a relativistic quantum field theory describing the electromagnetic (EM), the weak and the strong force with the gauge symmetry group $SU(3)_C \times SU(2)_L \times U(1)_Y$. The SM consists of 12 spin 1/2 fermions (six leptons and six quarks) and their respective anti-particles, 12 spin 1 bosons (eight gluons, three weak bosons and one photon) and one spin 0 boson (the higgs-boson). An overview is given in Figure 1.1.

Three generations of leptons are known: electron $e$, muon $\mu$ and the tauon $\tau$. They all carry the EM and the weak charge and therefore interact via the EM and the weak force. In each generation a respective neutrino exists: $\nu_e, \nu_\mu, \nu_\tau$. Neutrinos carry no EM charge, they only interact via the weak force.

The six quarks are the only particles that interact in addition to the EM and weak force via the strong force. They are carrying in addition to EM and weak charge the color charge. The six quarks are: up (u), down (d), charm (c), strange (s), bottom(b) and top (t). Due to the color

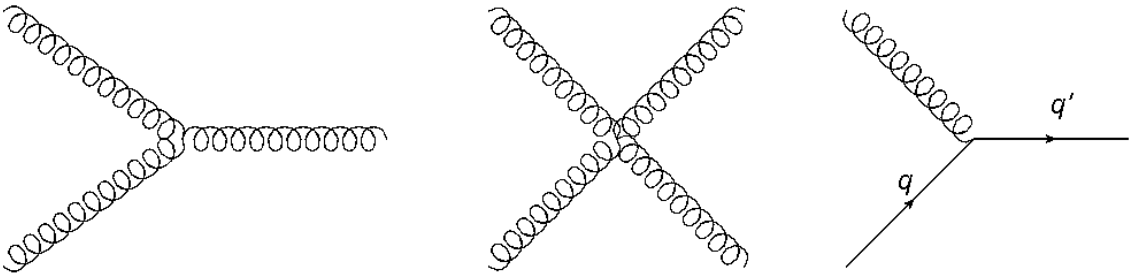


**Figure 1.2:** Illustration of three leading order three-level QCD interactions. From left to right: Two different gluon-gluon interactions and quark-gluon interaction.

confinement, a characteristic feature of the strong force, quarks can not be observed freely in nature - they are only observed bound in color neutral hadrons.
The interactions of fermions are described in quantum field theories by the exchange of a force mediator, a spin 1 boson. The electroweak force is described in a $SU(2)_L \times U(1)_Y$ symmetry. This symmetry generates four bosons, the photon $\gamma$, two $W$ bosons - one with positive one with negative EM charge - and the $Z$ boson. The strong force is described by an $SU(3)_C$ symmetry. The symmetry generates eight bosons, all gluons ($g$) but with different color charge. As a consequence of carrying their own charge, gluons and the weak bosons are self-interacting.
The last particle contained in the SM was only recently discovered in 2012, the higgs boson. The masses of the particles are generated by the higgs boson breaking the $SU(2)_L \times U(1)_Y$ symmetry. It is also self-interacting.

### 1.1.1 Quantum Chromodynamics

The interactions of quarks and gluons are described by the quantum chromodynamics (QCD), a quantum field theory. The main characteristics of QCD are the color confinement of quarks and gluons and the asymptotic freedom at high energies. Both characteristics are consequences of the self-interacting nature of gluons.

At leading order, QCD interactions are described by three level diagrams of quark-quark, quark-gluon and gluon-gluon interactions. At higher order more and more loop corrections contribute, and if all orders are taken into account, an infinite amount of loop corrections contribute. This would lead to a non-physical infinite probability for strong interactions or, in other words, an infinite strong coupling $\alpha_s$ for every QCD process at any energy $Q^2$. To avoid this, a correction factor to the strong coupling, the renormalization scale $\mu_R$, is introduced to cancel higher non-physical loop contributions.
The renormalization scale changes the behavior of the coupling: At low energies (or great distance between the interacting quarks/gluons) the coupling is large. At high energies (or small distances) the coupling is infinitesimal small. The later is called asymptotic free.
The "running" of $\alpha_s$ can be described more visually. Two quarks are bound together by a strong field, the gluons. Because of the self-interacting nature of gluons, the field is formed as a tube. The gluon loops within the field are enhancing the field energy and therefore the coupling, as they themselves carry the strong charge. At small distance, only a few gluon loops are within the field, so the field energy and the coupling is weak. At greater distances, more gluon loops are "seen",

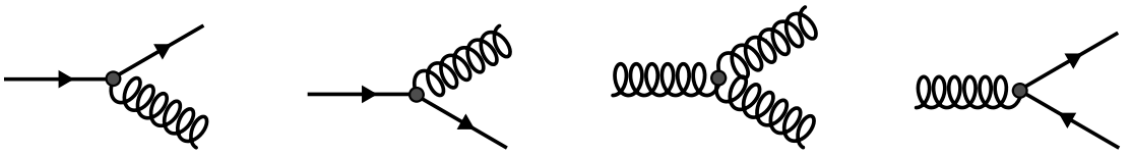

(a) $P_{q\leftarrow q}(z)$ (b) $P_{g\leftarrow q}(z)$ (c) $P_{g\leftarrow g}(z)$ (d) $P_{q\leftarrow g}(z)$

**Figure 1.3:** Illustration of leading order splitting processes: Gluon radiation (a,b), gluon splitting (c) and quark pair productions (d). Taken from [29]

the field is more energetic and the coupling is stronger. The greater the distance, the more gluons are within the field. At some distance, quark-anti-quark pairs are created by the gluons, which are energetically more favored than further gluon loops. This process stops as soon as only color neutral objects - hadrons - are formed. This effect is called color confinement.

### 1.1.2 Jet Production at a Proton-Proton Collider

A proton consists of three valence quarks (uud), which determine the outer properties of a proton (charge, spin, e.g.). The quarks are bound by gluons, which generate quark-anti-quark pairs (quark pair production) in vacuum fluctuations. These quarks are called sea quarks. All constituents of the proton (valence and sea quarks, as well as gluons) are referred to as partons in the following. The partons are bound in a very close proximity (1 fb) and are therefore approximately free. They are constantly interacting with each other. At leading order these interactions are defined as 1->2 splitting processes: gluon radiation, gluon splitting and quark pair production (see Figure 1.3). In a proton-proton collision at sufficiently high energy, two partons are colliding, as consequence of the asymptotic freedom. This collision is the so called "hard scatter" collision, which can be described as an elastic scattering of two point like objects. Hence, the cross section depends on the energy of the colliding partons. Each parton is carrying a fraction x of the protons momentum with it. At each splitting process, the momentum of the initial parton x is "split" between the outgoing partons. As the splitting processes can happen at arbitrary low energies, a scale is needed to define which splitting processes are considered as part of the proton (parton density functions (PDF)) and which are part of the hard interaction. This scale is called fragmentation scale $\mu_F$. The total cross section of two protons A, B with momentum $p_A$ and $p_B$, depends on the hard scatter cross section $\widehat{\sigma}$ of two partons a, b, and the PDFs $q_a$, $q_b$. Both depend on the parton momenta $p_a = x_a p_A$ and $p_b = x_b p_B$ and the fragmentation scale $\mu_F$. In addition, the hard scatter process depends on the center-of-mass energy of the proton interaction $Q^2$ and the renormalization scale $\mu_R$. All together, the cross section can be expressed as:

$$\sigma(p_A, p_B, Q^2) = \Sigma_{a,b} \int_{x_a, x_b=0}^{1} dx_a dx_b \underbrace{q_a(x_a, \mu_F^2) q_b(x_b, \mu_F^2)}_{PDFs} \times \underbrace{d\widehat{\sigma}(p_a, p_b, \alpha_s(\mu_R^2), Q^2/\mu_F^2, Q^2/\mu_R^2)}_{\text{hard scatter}} \tag{1.1}$$

In a hard scatter collision at high energies any particles of the SM or of new theories that interact with partons can be generated directly. However, the most dominant process in a proton-proton collision is the generation of two partons. Such a hard scatter process is called QCD process

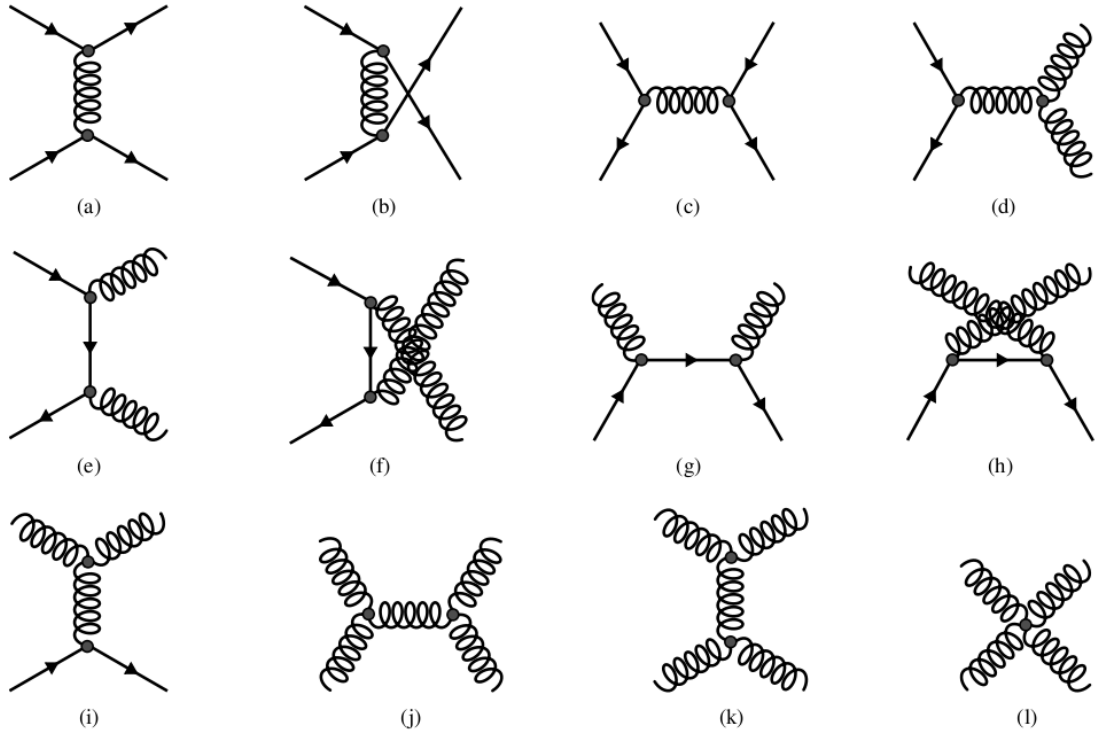


**Figure 1.4:** Leading order QCD process dominating in proton proton collisions. Taken from [29].

- all leading order QCD processes are shown in Figure 1.4.

In a QCD process the final state particles are partons. But partons are color confined, therefore as soon as a parton separates from the interaction, the strong field increases. A higher field energy enhances the probability for splitting processes. And with each splitting process, the momentum carried by each parton decreases. The process stops as soon as all created partons are bound in color neutral hadrons. Each hadron can decay further, and the final collimated hadron shower - a jet - is measured with a detector. The jet production is illustrated in Figure 1.5.

The splitting processes after the partons are generated can be separated depending on the angle between the created partons and the energy of the process in three different categories. If a splitting process is not collinear, two jets are generated and measured instead of one. Such a process is called "final-state-radiation" (FSR). A similar non-collinear splitting can happen within the proton, right before the hard scatter collision, and is called "initial-state-radiation" (ISR). ISR generates jets as well.

Additional to the FSR, shower building and hadronisation are differentiated. Both are collinear splitting processes. The hadronisation describes splitting processes at low energies, where bound hadrons a formed. Hence, the coupling is too strong and the processes are not perturbative anymore. Hadronisation, in contrast to shower building, is not analytical predictable, only iterative using algorithms. The energy scale used to distinguish between shower building and hadronisation is the fragmentation scale $\mu_F \approx 1\text{GeV}$.

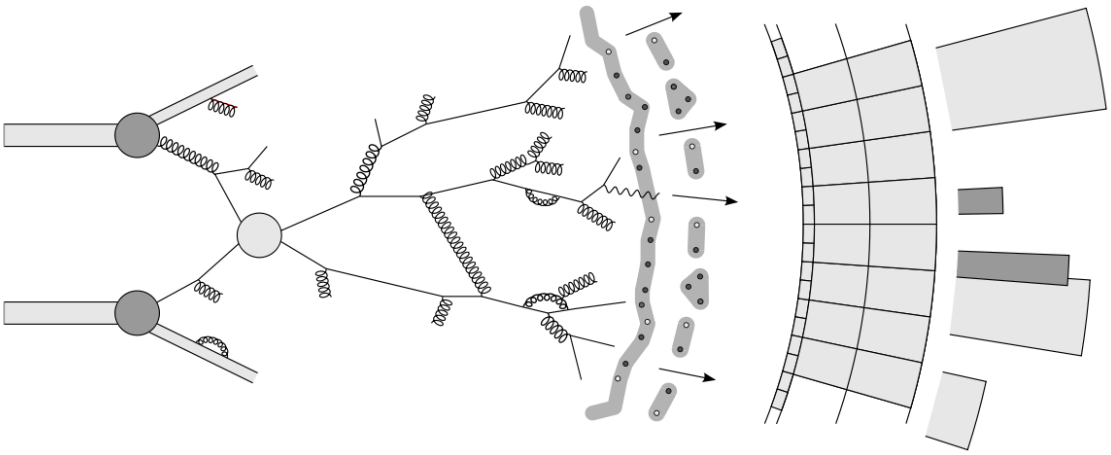

**Figure 1.5:** Illustration of the hard interaction of two partons, shower building and hadronisation at particle level before the energy is measured by a detector. Taken from [29]

## Monte Carlo Simulations

A Monte Carlo (MC) simulation as known in particle physics, is a simulation of particles created in a high energy collision of two particles. MC simulations are implementing theories describing particle processes, e.g. the SM but also new theories. The main purpose of a MC simulation is to compare the theoretical description with measured data.
However, a simulation of particle interactions includes a couple of choices. For a proton-proton collision, the simulation starts with a simulation of the proton itself. In here different sets of PDFs can be used, which can be tuned to describe the measured data better. In addition, right before the collision the modulation of the splitting processes within the proton are of special interest, as ISRs can be produced. Some simulations chose not to model the ISRs. The next simulation step models the hard scattering. The hard scatter process is fully described in theories, but for simulation only a certain degree of accuracy is feasible, as processes from all orders cannot be taken into account. For QCD processes mostly only leading order or next-to-leading order processes are simulated. Further, the simulation of the jet production depends on the chosen differentiation between FSR, shower building and hadronisation, and whether the FSR is modeled at all. In here, the hadronisation can be modeled by different algorithms. All these choices can lead to a different description of jets, which mainly changes the kinematic behavior at low energies ($< 20$GeV), but also the number of jets produced in a QCD process and more sophisticated variables like the shape of jets.
MC simulations predict the final states of particles, which are created during the hadronisation process. To be able to compare the predictions with measured data directly, an additional detector simulation, GEANT4 [24], is appended, which simulates the interactions of the final state particle with the detector material. Furthermore, the conditions within the LHC are simulated with respect to additional interaction contributions to the energy measurement in the detector. These additional interactions can be hard interactions of other protons colliding within a close time range of the main hard scatter interaction or the interactions of the remnants partons within the colliding proton. In following both are refereed to as "pile-up" events.

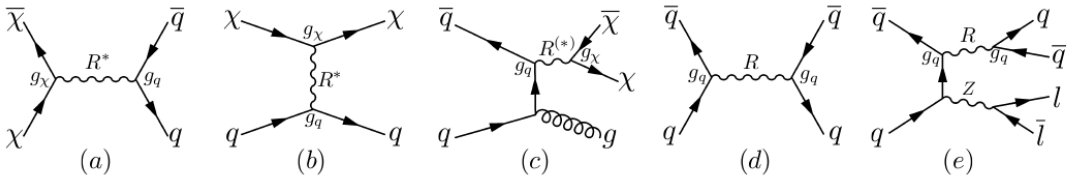


**Figure 1.6:** Leading order processes with dark mass mediator $R*$ (in text called $Z_B$). Taken from [20]

## 1.2 Dark Matter

The SM describes the known particles with an impressive accuracy, and since its inception in 1967 no significant deviations have been found. But even before the SM was created, the existence of matter not described in the SM was suspected: the dark matter. Under the assumption that gravity interacts with matter as predicted, the existence of dark matter has been suspected since 1930. A main evidence is the rotational velocity of galaxies. Due to gravitational force of the observable luminous mass alone, galaxies rotating at the measured velocities would not be stable. To guarantee the stability, six times more mass is needed. As this additional mass is not observed, it is suspected that dark matter particles exist, which do not interact via the EM force and, if at all, only weakly via the strong and weak force [28][34].

Different theories are trying to describe the dark matter and searches are trying to proof these theories. The most common theories are describing dark matter as "cold" non-relativistic matter. Suitable candidates for dark matter particles are weakly interacting particles (WIMPs), like sterile neutrinos. Further theories are exploiting super-symmetry particles as candidates, or explain the phenomena with extra dimensions.

In many theories the predicted dark matter particles ($\chi$) have a mass in the range to be created in high-energy collisions. As $\chi$ does not interact via EM or strong interactions it would escape any detector. This fact allows for direct searches via missing energy in the detector. But because of the challenges included in measuring missing energies, other search strategies are employed, e.g. indirect ones for dark mass mediators.

For a mediator search, a simplified bench mark model [20] is introduced. This model describes the interaction of the dark matter particle via an additional $U(1)$ symmetry, which generates the mediator gauge boson $Z'$. The charge of this group are carried by $\chi$ and quarks. $\chi$ would therefore be able to interact with quarks and with itself. And - most important for indirect dark matter searches, quarks would interact with themselves via the new mediator. The different interactions are illustrated in Figure 1.6, the important interactions for indirect searches are shown in (d) and (e).

In this theory, the parameters to be measured are the mass of the dark matter particle $M_\chi$, the mass of the mediator $M_{Z_B}$, the coupling between mediator and dark matter particle $g_\chi$ and the coupling between mediator and quarks $g_B$. In a dijet search, which analyzes events with two jets in the final state, a mediator would be observed as a resonance in the invariant mass distributions of the two jets ($m_{jj}$) at the mass $M_{Z_B}$, with a width depending on the coupling strength $g_B$. The other two parameters can be fixed with negligible effect on the resonance prediction on top of the dijet mass spectrum.

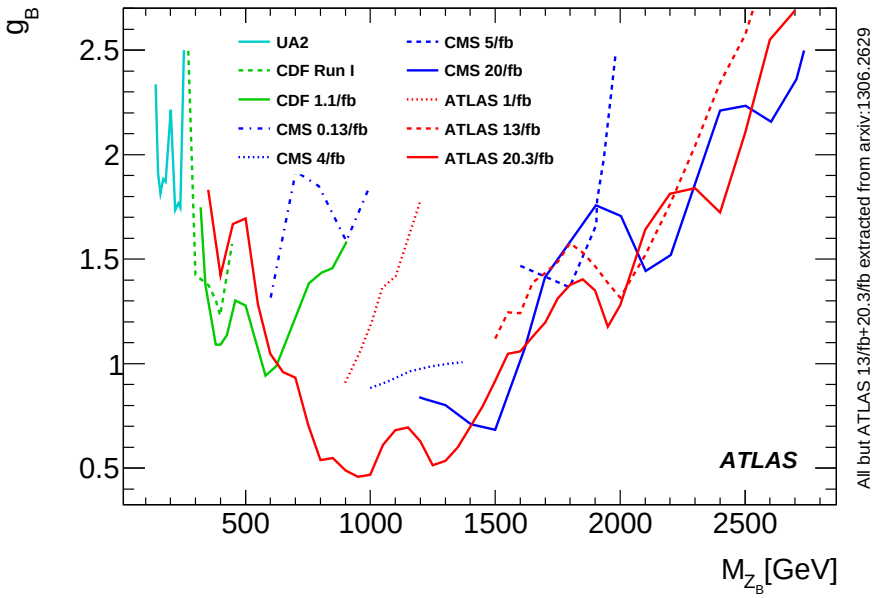


**Figure 1.7:** Upper limits set on the mediator mass $Z_B$ and the mediator-quark coupling $g_B$ in dijet-searches by different experiments. Latest included limits are set by 8 TeV searches at the Large Hadron Collider with the ATLAS and CMS experiment. Taken from [17].

Any findings in the dijet mass spectrum would result in a first evidence for the existence of a dark matter particle or more general for physics beyond the SM. Figure 1.7 shows the history of upper limits set on $M_{Z_B}$ and $g_B$ in dijet searches up to searches at the LHC with center-of-mass energy of 8 TeV. The best limits toward lower couplings at masses below 700 GeV are still set by earlier experiments, because in high-energy experiments, e.g. ATLAS, the bandwidth limitation prevents the necessary high event rate at low dijet masses, which is needed for stronger limits. Only recently, new dijet-searches like the TLA, started to make progress on dijet resonances at masses below 1 TeV.

# Chapter 2

# The ATLAS Detector

The analysis discussed here uses data created by proton-proton collisions in the LHC and recorded with the ATLAS detector. For a better understanding of the reconstruction and calibration of jets discussed later, the circumstances and relevant technical details of the LHC and the ATLAS detector are discussed in this chapter. First, the LHC is introduced. Then, an overview of the ATLAS detector with focus on the calorimeter system is given. Finally, the ATLAS trigger system and read out streams are introduced.

## 2.1 The Large Hadron Collider

The LHC is a proton synchrotron located near Geneva in a circular tunnel with a circumference of 27 km, 100 m under the earths surface. It accelerates and collides bunches of protons at a center-of-mass energy of $\sqrt{s}$ =13 TeV at four different interaction points (IP). At these IP the four main experiments of the Europe Organization for Nuclear Research (CERN) are situated: LHCb, ALICE, CMS and ATLAS.
The LHC accelerates protons to their final collision energy. It is filled by pre-accelerators with protons already at high energies. A proton beam consists of bunches and bunch trains, small packages of collimated protons. The bunches within a bunch train are separated by 25 ns, the bunch trains are separated by a short gap over a few bunches or by a larger gap over 450 ns. The proton beam is stable for a few hours, before the beam diffuses, because of proton interactions (planned ones as well as not planned ones). The diffused beam is ejected from the LHC and a new beam can be filled in. As a filling cycle including the acceleration of the protons takes a few hours, the data taking is separated into distinct periods called "runs". Runs are further summarized in run periods differentiating special setups in the LHC.
In the LHC a high event rate at the IP is important for high precision tests as well as for searches for new particles with low cross sections. The figure of merit of a circular collider is its luminosity $\mathcal{L}$, which connects the number of events per unit time $\frac{dN}{dt}$ and the cross section $\sigma$ of a given process:

$$\mathcal{L}\sigma = \frac{dN}{dt} \tag{2.1}$$

The luminosity itself depends on the number of protons per colliding bunch ($N_i$), the number of bunches per beam ($n$), the bunch spacing ($t_{\text{spacing}} = 1/f_{LHC}$) and the effective cross section area $A$ of the colliding bunches:

$$\mathcal{L} = \frac{nN_1N_2f_{LHC}}{A} \tag{2.2}$$

The luminosity can therefore be influenced by different settings of the collider. For example, the LHC can focus the proton bunches orthogonal to the beam pipe, which would decrease the effective area or increase the number of protons within a bunch. Another way would be to increase the bunch crossing frequency, which means shorter bunches or a smaller bunch spacing. All options are highly dependent on the focus power of the LHC, which is limited by the maximal achievable magnetic fields in the magnets.
A higher luminosity also has a downside. The average number of events per bunch crossing, $\mu$, is also related to the luminosity and the total inelastic scattering cross section $\sigma_{inel.}$ [14].

$$\mu = \frac{\mathcal{L}\sigma_{inel.}}{nf_{LHC}} \tag{2.3}$$

This number is averaged over a lager time ($> 600$ns) and estimates the number of pile-up events. Pile-up events are hard scatter events of two protons additional to the most-energetic hard scatter event. Two categories are distinguished: "in-time" and "out-of-time" pile-up events. In-time pile-up events are additional hard scatter events at the same bunch crossing. This event rate is increased with more protons or higher proton density within a bunch. Out-of-time pile-up events are additional hard scatter events in preceeding and succeeding bunch crossings. This event rate is increased with more bunches within a beam or a shorter bunch spacing.
In the last years, the luminosity was increased and the pile-up events became an increasing issue for the experiments within the LHC. The pile-up events complicate the energy measurements of particles created in the highest energetic hard scatter event. In 2015, the mean number of additional events were 14 at an integrated luminosity of $\mathcal{L} = 3.9$ fb$^{-1}$. In 2016, the mean number of additional events were 25 at an integrated luminosity of $\mathcal{L} = 36$ fb$^{-1}$ [21].

## 2.2 Overview and Coordinate System of the ATLAS Detector

ATLAS is a multi purpose experiment built for high precision SM tests and new physic searches. The ATLAS detector is build cylindrical around the beam pipe with different layers of detectors. From inside to outside, it consists of a tracking system (or inner detector) located inside a solenoid magnet, an EM calorimeter, a hadronic calorimeter and muon chambers. An overview is given in Figure 2.1. The different parts are discussed briefly in the following with focus on the calorimeter system. A full detailed description is provided in [8].

ATLAS uses a right handed orthogonal coordinate system with origin at the IP, the center of the detector. The z-axis runs along the beam pipe, the x-axis towards the center of the LHC ring and the y-axis points upward. The azimuthal angle $\phi$ starts ($\phi = 0$) parallel to the x-axis and turns towards positive z-direction. The polar angle $\theta$ starts in the transverse plane (x-y plane) and turns also towards positive z direction. Instead of $\theta$, the pseudorapidity $\eta = -\ln\tan\frac{\theta}{2}$ is more

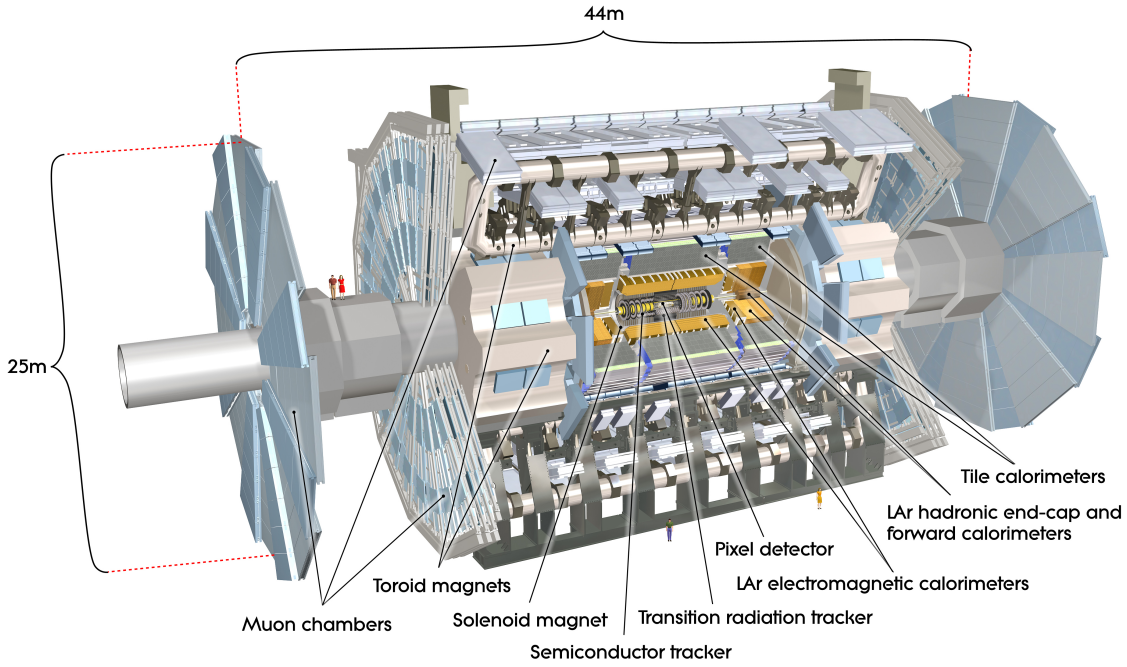


**Figure 2.1:** A computer generated image from the whole ATLAS detector. Taken from [31].

commonly used, because it is equal to the rapidity $y = \frac{1}{2}\ln\frac{E+p_z}{E-p_z}$ at high energies.
The detector is ordered into separate regions depending on $\eta$. The term barrel describes a central $\eta$ region, $|\eta| < 1.5$. The term end-cap describes the region $1.5 < |\eta| < 2.5$ and the term forward describes the region $2.5 < |\eta|$. In general, the locations within the detector are only defined via $\eta$ as the detector is symmetrical in $\phi$.

## 2.3 The Tracking System

The tracking system of the ATLAS detector is closest to the IP. It covers the range $|\eta| < 2.5$ and is used to locate the interaction points of the hard scatter events, which are called primary vertices (PV). A PV is mostly displaced relative to the designed IP. To be able to reconstruct a PV and also secondary vertices of long lived particles, the inner detector consists of high-resolution silicon detectors (pixel and strips). In addition, for a precise momentum measurement, the tracking system is located inside a solenoidal magnetic field of 2 T.

## 2.4 The ATLAS Calorimeter System

The ATLAS calorimeter system measures the energy and position of incident particles. It exploits the interactions of particles with different material that cause the creation of a cascade of particles and energy deposits through ionization.
In the ATLAS calorimeter system, two materials are used in sequences. An active medium, which

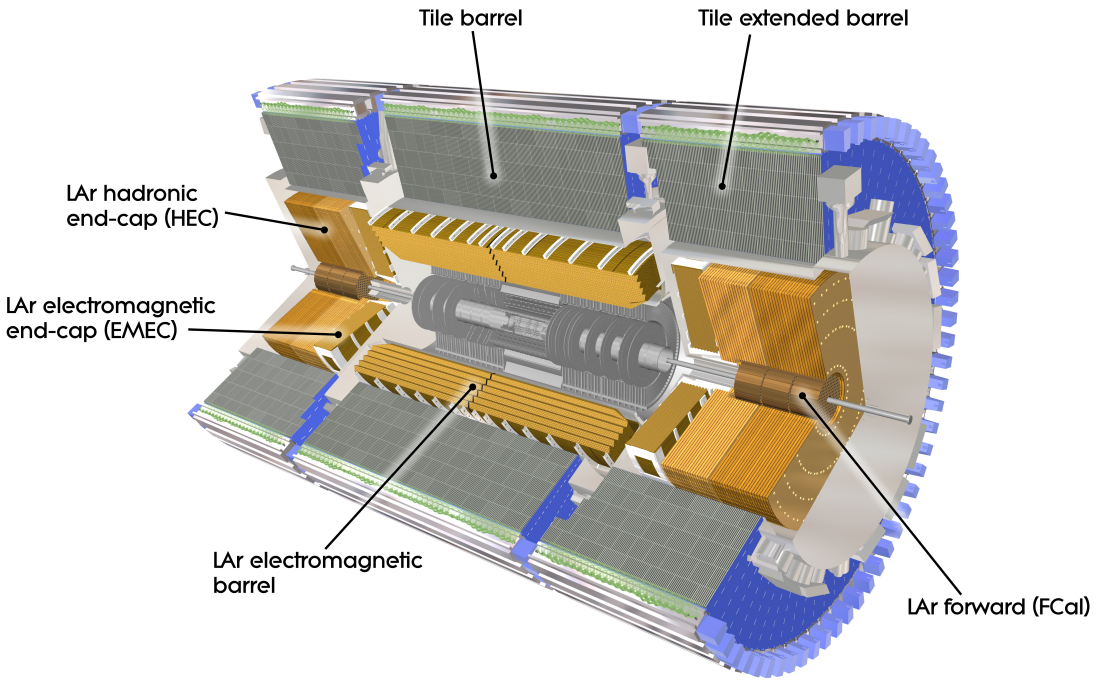


**Figure 2.2:** A computer generated image from the ATLAS calorimeter, taken from [30].

injects a signal proportional to the energy of the incident particle, and a passive medium, which absorbs the energy of the incident particle. As passive and active material are located in alternate layers, the calorimeter system consists of so called sampling calorimeters.
As EM and strong interactions with material leads to different shower properties (e.g. the radiation length of a shower), calorimeters with different materials are employed. They are differentiated into EM calorimeters and hadronic calorimeters. The different calorimeter sections are shown in Figure 2.2.

An important feature of all calorimeters is that they are non-compensating. While the EM shower is mostly fully detected by the EM calorimeters, the hadronic shower is not fully detected in EM and hadronic calorimeters. Hadronic showers create partly invisible energies ($\mu$ and $\nu$) due nuclear excitations and breakdowns, which escape detection. Consequently, the energy of hadron showers a underestimated.
In the following, the different calorimeters of the ALTAS detector are described. Each of them is a sampling calorimeter, but with different segmentation of active and passive mediums and different mediums. A coarser segmentation worsens the granularity of the calorimeter cells, in which the energy is measured. An overview of the evolution of the granularity is given in Figure 2.3.

### 2.4.1 Electromagnetic Calorimeters

Electromagnetic calorimeters are using liquid argon (LAr) at 8 K as active material. As the passive absorber lead is exploited in the barrel region. The LAr is within an electrical field, which causes the electrons created by incident charged particles ionizing the LAr to drift towards copper

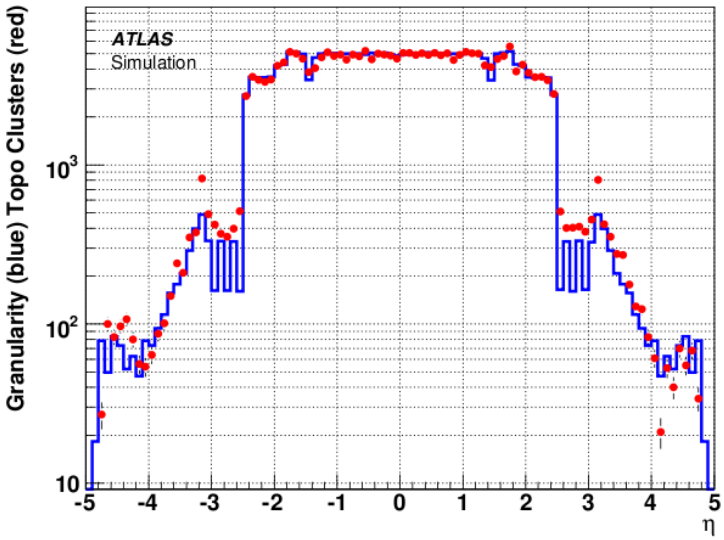


**Figure 2.3:** Granularity of the calorimeter cells with respect to $\eta$. Taken from [12].

electrodes. As the drift velocity of the electrons is part of the energy reconstruction, the electrical field and temperature of the LAr have to be closely monitored.
The electromagnetic calorimeters consists of two barrel calorimeters covering the range $|\eta| < 1.475$ and two end-cap regions covering $1.375 \leq |\eta| < 3.2$. The end-caps are split into two coaxial wheels. Between the barrel and the end-cap region, the "transition $\eta$ region" is located. This region is used to monitor, cool and instrument the tracking system and therefore contains additional "inactive" material. The energy measurement in the transition $\eta$ region is underestimated.
The EM calorimeter is divided into three layers and each layer is build with an accordion structure to ensure full symmetry in $\phi$ and a fast read out. The structure is illustrated in Figure 2.4. The LAr is located within the gaps (2.1 mm) of the absorbers leading to an average drift time around 450 ns.
The strips are segmented differently in each layer. In the first layer, the segmentation is very fine $\Delta\eta \times \Delta\phi = 0.0031 \times 0.098$. With information gathered in this layer, particles are reconstructed and identified. The second layer is the highest layer and most of the energy of incident particles is deposit here. The stripes are separated less fine with $\Delta\eta \times \Delta\phi = 0.0245 \times 0.025$. The third layer is constructed to contain shower tails and is separated in stripes of $0.0245 \times 0.05$. This structure is the same in the first LAr end-cap wheel calorimeter. The second wheel around $2.5 < |\eta| < 3.2$ has a coarser granularity in the stripes of each layer.
For $|\eta| < 1.8$ an additional LAr calorimeter is installed, the presampler. It is composed of 1.1 cm (0.5 cm) thick layers of LAr in the barrel (end-cap) region. It is placed directly in front of the EM calorimeters to measure the energy lost before the calorimeters.

### 2.4.2 Hadronic Barrel Calorimeters

The hadronic barrel calorimeter (Figure 2.5) exploits plastic scintillator tiles as active medium, therefore these parts of the ALTAS detector are also called tile calorimeters. As the passive

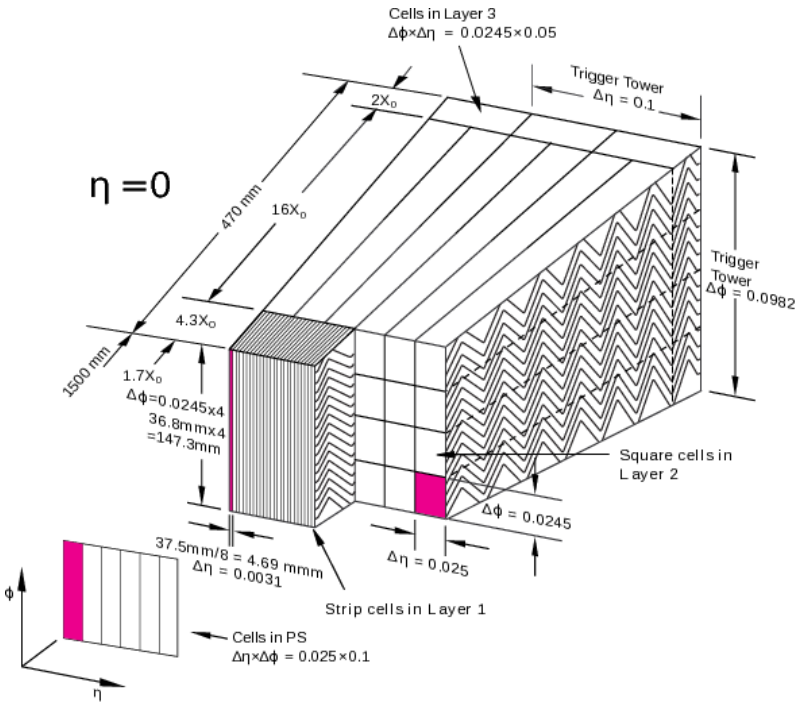


**Figure 2.4:** Illustration of the LAr calorimeter barrel, showing structure and granularity of the different layers. Taken from [7].

absorber steel is used. The tile calorimeter consists out of a barrel ($0 < |\eta| < 0.8$) and an extended barrel ($0.8 < |\eta| < 1.7$) region.
The tiles in the calorimeter are 3 mm thick and arranged orthogonal to the beam pipe. The scintillation light created by particles interacting with the tiles is caught by wavelength shifting fibers. With the fibers the light is guided to photomultiplier located at the ends of the tiles. A group of fibers represent one tile calorimeter cell.
The tile calorimeters consists of three layers with varied granularity. $\Delta\eta \times \Delta\eta = 0.1 \times 0.1$ in first two and $0.1 \times 0.2$ in the third layer.

### 2.4.3 Hadronic End-Cap and Forward Calorimeter

To be able to fully contain a hadronic shower in all regions of the detector, a special detector located in the forward region is needed. Two additional calorimeter types are installed: The hadronic end-cap calorimeter (HEC) and the forward calorimeter (FCal).
HEC is placed at the region $1.5 < |\eta| < 3.2$, 2.03 m away from the IP. It uses copper plates, which are arranged with 8.5 mm gaps in which the active medium LAr is placed. The copper plates thickness increases with the distance to the IP (from 25 mm to 50 mm).
The forward calorimeter (FCal) is placed 4.7 m from the IP and covers the region $3.1 < |\eta| < 4.9$. It also uses LAr as the active medium, which is located in 270 µm gaps within copper and tungsten plates. For FCal dense absorbers are chosen to provide shower containment.

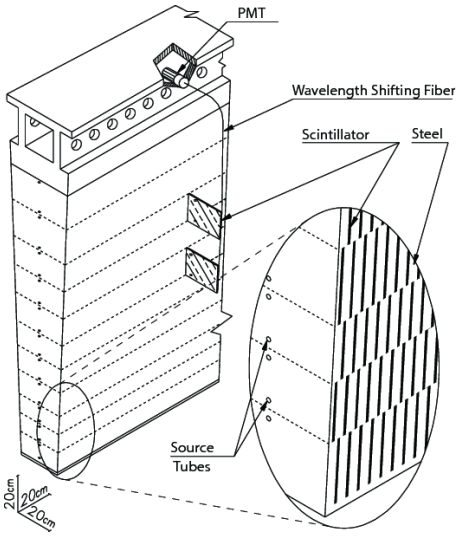


**Figure 2.5:** Illustration of the Tile Calorimeter. Taken from [7].

### 2.4.4 Calorimeter Pile-Up Sensitivity

The energy deposited in the calorimeters is measured either through electrical signals induced by ionized electrons of the LAr or scintillation light in the tiles. Both produce a pulse with an amplitude proportional to the energy of the incident particles hitting the cell. In both cases the signals are amplified and shaped for every bunch crossing, every 25 ns. The shaping is done by measuring 5 or 7 different points in each pulse. On these points weights are applied, that are calculated during a special calibration measurement beforehand.
For an ideal pulse in a tile cell, this procedure results in a reconstructed shape as illustrated in Figure 2.6. The energy and the timing of the pulse is calculated via the 5 or 7 recorded points of the pulse, only. Simplified, the energy is proportional to the amplitude, which is calculated using the difference between the pedestal and the maximum value of the pulse. The pedestal accounts for electrical noise and pile-up induced noise, which are measured separately. The timing or phase of the pulse is represented by the width of the pulse. It is calculated depending on the amplitude and the pedestal of the pulse. The exact energy and timing reconstruction method of the tile calorimeter is described in [10].

A pulse in a LAr calorimeter cell is shaped to a bipolar signal shape (Figure 2.7) with a net zero integral over the time. Due to the long drift time of an ionization electron in the LAr (450 ns), the LAr cells are sensitive to pile-up interaction, especially to out-of-time pile-up. The bunch crossings are separated by 25 ns, a fraction of the collection time of the calorimeter cells. Therefore, the energies of particles created in preceding and following bunch crossings increase the energy in one cell as well as additional interactions in the same bunch crossing. Tile calorimeters are hardly affected by pile-up, because most pile-up interactions are low energetic and deploy most of their energies in the EM calorimeters.

The bipolar shaped pulse is designed to cancel on average the in-time pile-up with the out-of-time pile-up. As the pulses of the different bunch crossings overlay with each other slightly shifted, the positive weighted pulses are added to the negative weighted pulses. However, this procedure only

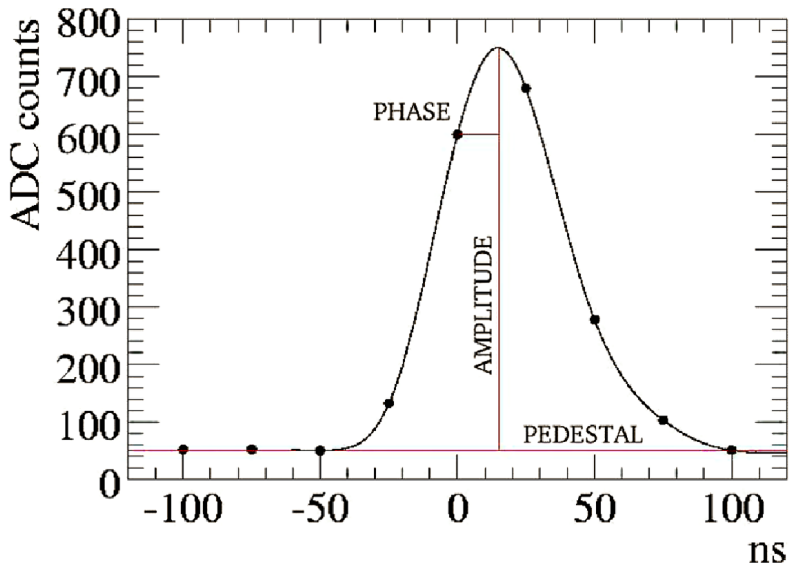


**Figure 2.6:** Sketch of a tile calorimeter cell pulse. Taken from [1].

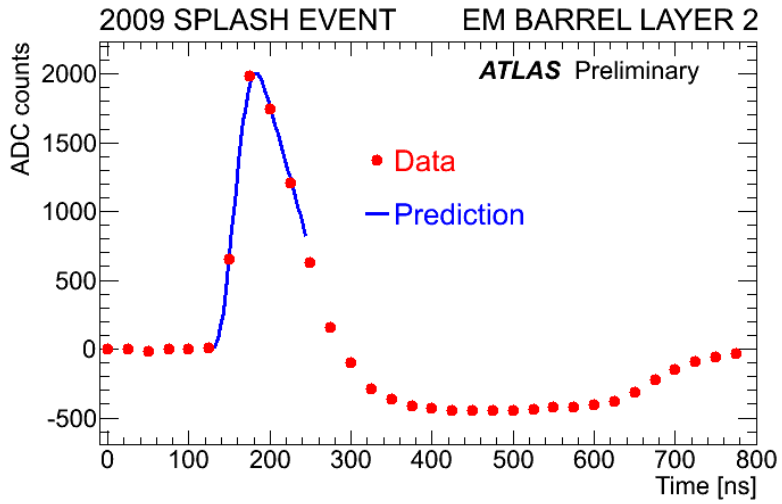


**Figure 2.7:** Bipolar pulse in a LA barrel calorimeter cell. Taken from [6].

works on average. Due to pile-up fluctuation from bunch crossing to bunch crossing, a certain pile-up sensitivity in the cells remains. This sensitivity varies with the exact bipolar pulse shape. Within the forward region, the amplitudes of the pulses are higher than in the barrel or central region to account for worse granularity and higher pile-up rate[1]. Consequently, the forward region is more sensitive to pile-up than the central or barrel region.
In addition, for the first bunch crossing in a bunch train, the averaging does not work as no negative weighted pulses from preceding bunch crossings could cancel the positive weighted pulse. In the first bunch crossings in a bunch train, the energy in a LAr cell is overestimated. The additional energy dependency on the number of bunch crossing (BCID), is called BCID dependent pile-up.

## 2.5 The Muon Chambers

The muon champers is the outermost detector region. In here the muons deposit their energies. As muons are quite heavy and hardly ionizing, they pass mostly all previous calorimeters and reach the muon chambers. In here, their energies are measured by high precision gaseous detectors, which include monitored drift tubes and cathode stripes for the region $|\eta| < 2.7$. For a selection of interesting muon events, corse chambers are used, either resistive plates chambers or thin gaps chambers.

## 2.6 Trigger System and Read Out Streams

In the LHC over $10^{13}$ protons are colliding every second. To record every event, a read out rate of over 1 MHz would be needed. The possible bandwidth at ATLAS is only around 1 kHz, though. The aim of the trigger system is therefore to decide within the shortest possible time which events are interesting and should be kept. The events, that are kept, are written out to data streams.

### 2.6.1 Level 1 Trigger

The trigger system is split into two levels. Level one (L1) is a trigger system implemented in hardware. It has 2.5 µs to reduce the event rate to 100 kHz. For this purpose, it reconstructs high energetic objects (photons, muons, electrons, taus, jets and missing energy) using only calorimeter and muon information with reduced granularity. If the energy of the object is above a certain threshold, the event is declared as interesting and passed to the next trigger level.
The reconstruction of objects is separated in different blocks. First, the signal in the cells are digitized. Then, the energies of each cell are calibrated and aligned. Next, the high energetic objects are searched and energies of the objects calculated.
There are a couple of different thresholds implemented on different triggers. As example, the L1-J100 trigger fires on all events with an high energetic object over 100 GeV. This energy refers to the energy at the detector level with different calibrations and corrections applied than on objects after data taking. The actual energy an object has to have to be selected by a trigger is calculated

[1] Most additional hard scatter events create low-energetic jets at a small scattering angle, which end up in the forward region.

for every trigger respective. The efficiency of a trigger selecting (fully calibrated) objects with certain energies is described in "turn-on curves". In addition to the threshold values, most low energetic triggers include a prescale rate. As example, a prescale rate of 100 means only every 100th event, that would pass the threshold of a trigger, is actually selected.

### 2.6.2 High-Level trigger

If an event passed the L1 trigger, the detector data and the region of interes (RoI) of the detector is passed to the second and last level of the trigger system: the high-level trigger (HLT), a purely software based system. In this stage, the remaining bandwidth is reduced to 1 kHz. The HLT consists of an event building block, in which the data fragments assigned to each BCID are combined to an event, and several trigger object algorithms. The HLT uses the full granularity of the calorimeter.
Different triggers for different particles exists, e.g. charged lepton triggers and jet triggers. In the jet trigger system, events are selected purely on the jet energies and/or on their $\eta$ location. Therefore, the jet energy and direction reconstruction is of main importance already during data taking. The jet reconstruction used in the HLT during data taking (online) is very similar to the jet reconstruction done after data taking (offline). The procedure of the offline reconstruction is described in section 3.1 and the differences to the online reconstruction are described in chapter 6. The jet-trigger decisions is made on calibrated HLT jets. The online calibration scheme is a slimmed version of the offline calibration scheme, which is described in section 3.2. It only contains the "jet area correction" and the "jet energy scale calibration derived on MC simulations". The MC simulation used for the calibration was derived in 2012.
Like L1 triggers, there are many different single jet triggers, which are looking for jets with an energy over a threshold and/or within a certain $\eta$ region. As example, the HLT-j110 is "seeded" by the L1-J25 trigger, meaning only events passing the L1-J25 trigger are evaluated with the HLT-j110. Only jets with a momentum of at least 110 GeV are selected by the HLT-j110.
In total, the jet trigger system is limited to an event rate of 80-100 Hz [3], which can only be archived due prescale rates on single jet triggers. The first jet trigger without a prescale rate applied requires a transverse momentum of at least 400 GeV. The remaining bandwidth are needed for other HLT systems.

### 2.6.3 Data Streams and Reprocessing

Events selected by an HLT are written to the "data stream" the relevant trigger is assigned to. In this way, the data is first saved and later reprocessed with offline reconstruction and calibration methods. Then, the reprocessed data is either directly used for an offline analysis or a pre-selection for special events are applied to create a "derivation".
There are different streams an event can be written to; some events are also written to more than one stream, if they were selected by more than one HLT. Here listed are the most important stream for this thesis:

- physics-main stream: Most events are saved in the physics-main stream (or main stream). Events are reprocessed with the "bulk" reprocessing, which contains various offline jet reconstruction and calibration schemes.

- express stream: Triggers assigned to the express stream have a higher prescale than triggers assigned to the main stream, and so less events are written to the express stream (10 Hz [3]). The express stream is needed for the sign-off procedure of the data: if problems occurre due to detector or accelerator issues, they are seen (if not online) in the express stream. In addition, the reconstruction and calibration methods are tested and improved, e.g. by excluding noisy cells for jet reconstruction. There are two reprocessing procedures, that can be applied to express stream data: the express reprocessing and the bulk reprocessing.

- data-scouting stream: The data-scouting (DS) stream is a special stream introduced for TLA purposes. In here, only partial information about an event is written to. Events are selected by a special HLT. This trigger is seeded by L1-J75 or L1-J100 and selects all events containing a jet with at least 20 GeV. The calibration of HLT jets written to the DS stream is the main topic in this thesis and discussed in chapter 5 to chapter 7.

In addition to the streams, some information about detector or accelerator conditions, e.g. the averaged number of events per bunch crossing, are written to the "data base". Information written to the data base are available to all streams.

# Chapter 3

# Jet Reconstruction, Offline Calibration Scheme and Quality Selection

In a proton-proton collision at the LHC the most dominant process creates jets, a collimated shower of hadrons. These hadrons reach the ATLAS detector and deposit their energies within the calorimeters. To obtain information about the initiated parton, the energy deposits have to be reconstructed to a jet. Depending on the algorithm used for the reconstruction, the shape and energy of the reconstructed jet varies. These variations are large, so that jets are in principle only comparable to jets reconstructed with the same algorithm. In other words, the reconstruction of a jet defines it.
To be able to compare measurements using jets the calibration of the jets has to be known, in addition to the reconstruction algorithm. As the ATLAS detector is non-compensating, only a fraction of the jets energy is actually measured. The rest of the energy has to be calibrated. Jet energies are only comparable, if the jets are calibrated to the same "energy scale".
In this thesis, the TLA calibration scheme for HLT jets is discussed. As this scheme is new, the performance has to be validated by comparing the energy of HLT jets to the energy of well calibrated jets. For this purpose, HLT jets are compared to "offline jets", which are reconstructed very similar like HLT jets and calibrated with a well established calibration scheme. In this chapter, the jet reconstruction and the offline calibration scheme is presented. In addition, the standard ATLAS quality selection for events and jets is presented.

## 3.1 Jet Reconstruction

The reconstruction and therefore the definition of a jet depends on the algorithm used and the objects being reconstructed - the input of the algorithm. On data, the inputs are either calorimeter cells, calorimeter towers, topo-clusters or tracks. A jet reconstructed based on these objects is called accordingly, e.g. a track jet. In MC simulation, additional inputs can be particles or the initiating parton. In the last case, the jet is called "truth" jet and represents the parton itself.

Apart from truth jets, all other jets need to specify the jet algorithm with which they are reconstructed. Offline jets as well as HLT jets are AntiKtTopoCluster jets, which means they are reconstructed using topo-clusters as input and the "anti-$k_T$" algorithm as recombination scheme. In the following, the reconstruction of an AntiKtTopoCluster jet is presented. It starts after the cell energy reconstruction, which is roughly introduced in section 2.4.

### 3.1.1 Topo-Clusters

Topo-clusters [25] are calorimeter cells clustered into three-dimensional energy deposits. The clustering method includes a noise and pile-up suppression and follows the shower development of the incident particles. It exploits the fine segmentation in the calorimeters.
The clustering to topo-clusters consists of two iterations. The first iteration starts from a "seed cell" with a signal-to-noise ratio above 4 ($S/N > 4$). Then, all adjacent cells with $S/N > 2$ and finally, all adjacent cells with $S/N > 0$ are clustered together. The signal-to-noise ratio is calculated by dividing the energy of the cell by the cell noise. The noise is estimated by measuring the RMS of the energy distribution in a cell, which is simulated in MC simulations with a fixed value for the average number of additional events per bunch crossing $\langle\mu\rangle$. With the high signal-to-noise ratio for the seed cells, events containing electrical noise and pile-up events are suppressed. The second iteration is a splitting step, in which the clusters found are split into several clusters, if they include more than one cell with an energy higher than a few hundred MeV and higher than the energy in adjacent cells.
A topo-cluster is defined as an object with no mass. Its energy corresponds to the sum over all energy deposits within the cluster. The coordinates of topo-clusters are reconstructed to point from the IP to the center-of-energy of the cluster.

### 3.1.2 The Anti-$k_T$ Algorithm

The anti-$k_T$ algorithm [27] is used to recombine topo-clusters to a jet. It is a successive recombination algorithm, which is infrared and collinear safe and combines objects depending on their distances.
The distance of two topo-clusters i and j is defined by combining the physical distance in the detector $\Delta R = \sqrt{(\phi_i - \phi_j)^2 + (y_i - y_j)^2}$ with the transverse momenta $p_T$ of the topo-clusters:

$$d_{i,j} = min(p_{T,i}^{-2}, p_{T,j}^{-2}) \frac{\Delta R}{R} \tag{3.1}$$

with the radius $R$, the defining parameter of the algorithm. The distance of one topo-cluster i to the IP, is defined as the transverse momentum of the cluster:

$$d_{i,det} = p_{T,i}^{-2} \tag{3.2}$$

The algorithm merges cluster $i$ and cluster $j$ if they fulfill the requirement $d_{i,j} < d_{i,det}$. If no cluster j fulfilling this requirement is found, cluster i is defined as a jet. The minimum criteria within the distance $d_{i,j}$ (Equation 3.1) ensures that the algorithm starts with the cluster with the highest transverse momentum. Simplified, all clusters within a radius R around it are combined.

With this approach the energy flow of particles is followed and the reconstructed jets have a circular area. In Figure 3.1 an example of recombined topo-clusters are shown. The colored areas indicate the reconstructed jet area.
In practice, the ATLAS anti-$k_T$ algorithm is implemented using the FastJet package [26]. In here, only topo-clusters with a transverse momentum of at least 7 GeV are taken into account. Further, the algorithm is implemented with two different radii: 0.4 and 0.6. In this thesis only jets reconstructed with R = 0.4 are taken into account, as they are less sensible to pile-up effects.

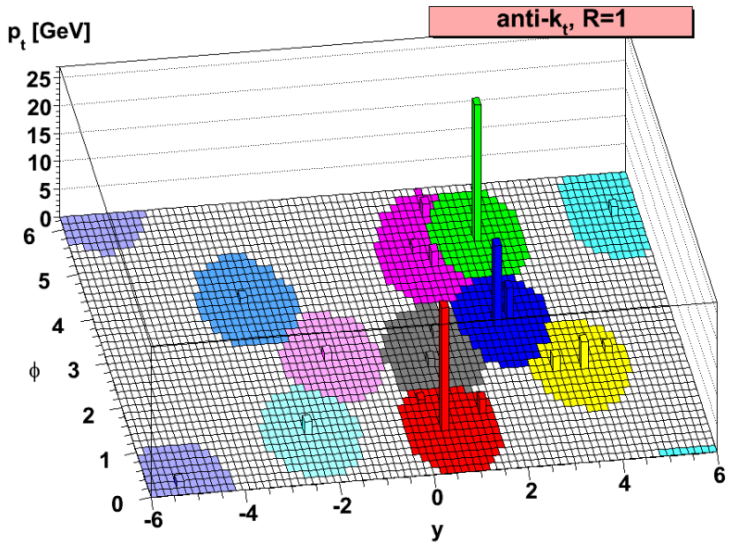


**Figure 3.1:** Topo-clusters combined with the anti-$k_T$ algorithm with $R = 1$. The colored areas represent the reconstructed jets in the calorimeter in the $y$ - $\phi$ plane. Taken from [27].

## 3.2 Offline Jet Calibration

A calibration describes the comparison of a measured value with a reference value with a calibration standard of known accuracy. If a significant deviation is noted, the measured value is adjusted to agree with the value of known accuracy. Following this definition, the jet calibration describes the comparison of the jet energy measured with the ATLAS detector with the energy of a chosen reference object. This reference object is a truth jet, which is defined to be calibrated with a 100% accuracy in MC simulation. But as a 100% accuracy in MC simulation does not represent a 100% accuracy in data, jets are calibrated with more than one reference object. Hence, the total calibration of jet energies consists of different calibration and correction steps, all summarized in a calibration scheme.
In general, jets have to be calibrated, because of the non-compensating nature of the detector. The jet energy measured in the calorimeters consist of only 50% (for jets with low momentum) up to 90% (for jet with high momentum) of their true, hadronic energies. But also other effects biases the jet energy measurement further and need to be accounted for by the jet calibration.

The main issues are listed in the following.

- Calorimeter-non compensation: Jet energy is only partial measured by the detector.
- Inactive material: Jet energy is lost in inactive areas of the detector. The inactive areas are not distributed uniform over the calorimeter regions, e.g. the transition $\eta$ region ($1.4 < |\eta| < 1.6$) contains more dead material than other regions.
- Leakage (or punch-through): Jets are not fully contained in the calorimeter.
- Out-of-cone effect: Particles are not reconstructed as part of the jets, because of magnetic deflections or FSR.
- Energy deposits below noise threshold: Cells with a too high noise threshold are not combined to topoclusters.
- Pile-up: Additional particles, that do not originating from the same hard scatter event, are included in the jet reconstruction.

### 3.2.1 Energy Scale, Response and Resolution

The energy of a jet is measured at EM scale and needs to be calibrated to hadronic scale, which represents the true energy of the initiated parton. The hadronic scale is an ambiguous term, as different calibration methods exist, which all calibrate the jets to hadronic scale. Therefore, additional scales are introduced within this thesis, to define the calibrations applied to a jet. In ATLAS, the jet energy scale is defined as the average "response" of the reconstructed jets to truth jets. Ideally, if the jet is fully calibrated, the energy scale is around one. In data, the scale can not be evaluated directly, as truth jets are not defined. The scale can therefore only be compared with an other object reconstructed on data, with an other reference jet.
The response of a jet is calculated by dividing the reconstructed jet energy $E^{jet}$ by the energy of a reference jet $E^{ref}$ in bins of $E^{ref}$ and (most commonly) the location within the detector $\eta_{det}$.

$$R(E^{ref}, \eta_{det}) = \frac{E^{jet}(\eta_{det})}{E^{ref}(\eta_{det})} \tag{3.3}$$

The ratio is calculated for jets within a certain distance $\Delta R$ of each other: jets that match each other and therefore are likely to describe the same detector object. The jets closest to each other are called matched. The mean of the response distribution is the mean response, or if the reference jets are truth jets, the energy scale. The response can also be calculated with momentum ratios.
The jet energy resolution (JER) is defined as the width of the response distributions with truth jets as reference objects. It reflects the fluctuations of the reconstructed calibrated energy with respect the truth energy of the object. The resolution cannot be avoided, as the calibration constants are calculated using the mean of the response distribution. The resolution can be reduced though, by accounting for specific jet characteristics, e.g. the flavor of the initial jet, to which the energy measurement of the calorimeter, the calorimeter response, is sensitive to. These characteristics are described in more detail in [15].

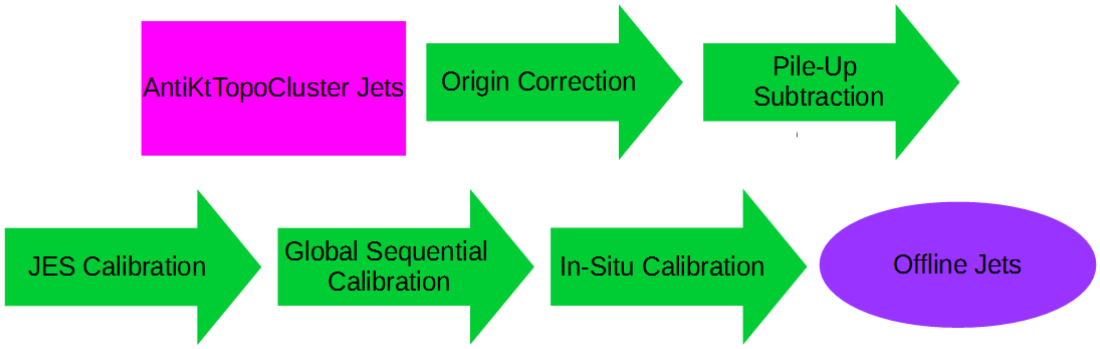


**Figure 3.2:** The calibration scheme for offline jets.

### 3.2.2 Offline Jet Calibration Scheme

The calibration aims to correct reconstructed offline jets to hadronic scale as well as to reduce the JER as much as possible. In the following, the single steps of the offline calibration scheme are introduced, which consist of the EM+JES scheme in addition to global and in situ corrections. In Figure 3.2 an overview of the offline calibration scheme is given.

In general, the single calibration step leads to correction factors that are applied depending on $p_T$ (or $E$) and $\eta$ of the offline jet at EMS. The largest correction factors of up to 80% are calculated in the main calibration, the jet energy scale calibration (JES calibration). This calibration is chosen to be calculated with MC simulation and truth jets as reference values, as the simulations are very sophisticated. The subsequent calibrations are within a few percent, and correct for uncertainties induced by MC simulations. Preceding to the JES calibration, the pile-up correction are applied to the reconstructed jets at EM scale. It calculates an energy offset to the jet energy ($E_{EM,\text{offset}}$), which is subtracted from the total jet energy at EM scale ($E_{EM}$).

The total calibration to reach hadronic scale is applied using:

$$E_{had} = (E_{EM} - E_{EM,\text{offset}}) \cdot c(E^{EM}, \eta) \tag{3.4}$$

with $E_{had}$ being the jet energy at the hadronic scale. The calibration scheme EM+JES, which consist of the pile-up corrections and the JES calibration, applies correction factors to jet energy and transverse momentum. Other calibration schemes, like the local cell weighting (LCW) or global cell density weighting (GCW), calculate corrections based on cell or cluster level information in the detector. The LCW weights clusters depending on hadronic or EM energy before summing them up and applying further corrections based on energy loss to the clusters. The GCW calculates the energy loss in each cell, and applies an overall correction to each jet. Consequently, the jet energy resolution of LCW or GCW scheme is up to 2% better than in EM+JES. The drawback though, is an increased JES uncertainty, especially at $p_T < 600$ GeV [25]. For later comparisons to HLT jets it is important that the reconstruction done online is the same as done offline. LCW and GCW are not implemented for the HLT jet reconstruction, therefore the well understood and reliable EM+JES scheme is used to calibrate offline jets in this thesis.

### 3.2.3 Origin Correction

The first calibration step is the origin correction, during which the jet coordinates are modified. All constituents and thus all jets are reconstructed to originate from the center of the detector, the designed IP. But the physical interaction point (PV), is shifted with respect to IP along the beam pipe around $RMS^z_{PV} = 29.7$ mm [14]. Consequently, the jet coordinates have to be corrected to point back to the actual PV. This correction does not affect the energy, only the angular resolution.

### 3.2.4 Pile-Up Subtraction

In the last years, the LHC has reached higher and higher luminosity. With higher luminosity, the number of pile-up interactions rises, as described by Equation 2.3. The subtraction of pile-up events, which are either reconstructed as additional jets or as additional energy within a jet, is one of the main challenges in the jet calibration.
The procedure is split in two main parts: the jet area subtraction and the residual offset correction. The jet area subtraction measures the general susceptibility within a jet to additional pile-up energy by calculating the jet area. The residual offset correction is an event-by-event correction, calculating the jet energy offset caused by in-time and out-of time pile-up.
In addition to the calorimeter signal read out (bipolar signal shaping) and the clustering algorithm (signal-to-noise thresholds) are set up to suppress pile-up signals. Additional criteria, like the jet vertex fraction criteria [5], can be applied to avoid jets not likely to origin from hard scatter events in the current bunch crossing.

#### Jet Area Subtraction

The jet area subtraction [12] treats pile-up as a uniformly distributed background. It is preformed during data-taking, as an implementation of the FastJet algorithm. First, the jet area is estimated by inducing a dense, uniform population of "ghost" particles with infinitesimal transverse momenta in the calorimeter, before the jet reconstruction is done. The result of the anti-$k_T$ algorithm is not changed by the additional soft particles, and therefore the jets are kinematic unchanged. The number of the ghost particles within a jet, or more exactly the combined four-momentum, gives an estimate of the area $A_i^{jet}$.
Second, the event mean $p_T$ density is calculated using

$$\rho = \text{median} \left\{ \frac{p_{T,i}^{jet}}{A_i^{jet}} \right\} \tag{3.5}$$

where the index i enumerates the jets within $\eta \leq 2.0$ included in the event. The $p_T$ density estimates the event wide pile-up density, assuming that pile-up behaves like an uniformly distributed background.
Third, the mean pile-up contribution $\rho \cdot A$ of a jet is subtracted from jet momenta:

$$p_T^{\text{jet,corr}} = p_T^{\text{jet}} - \rho \cdot A \tag{3.6}$$

The jet area correction is very successful in suppressing in-time as well as out-of-time pile-up contributions in the central region. The procedure corrects for event-by-event fluctuations of the

number of pile-up events, but not for local fluctuations.

**Residual Offset Correction**

In the forward region more pile-up events are expected and the cell occupancy is higher. The LAr end-cap calorimeters counter the increased pile-up with a higher amplitude for the bipolar signal shape (section 2.4). Isolated out-of-time pile-up fluctuations, that are not averaged out by the pulse shape and are overlaying with hard scatter energy deposits, lead to negative energy modulation in corresponding cells and consequently to an underestimation of the total jet energy. Neither these negative energy contributions nor local pile-up fluctuations are corrected for in the jet area pile-up subtraction. A residual offset correction is needed to account for these effects [13]. The residual offset correction [14] depends on the number of primary vertices ($N_{PV}$) and the average number of interactions per bunch crossing ($\langle\mu\rangle$). The number of in-time pile-up events $N_{PV} - 1$ is determined using the tracking system, whose time resolution is sufficiently good to only count the in-time vertices. The number of interaction per bunch crossing $\mu$ is averaged by choice over a rather long time period and estimates the number of out-of-time pile-up events.
The residual correction is computed using MC simulation. The offset is calculated according to

$$\begin{aligned} O(N_{\mathrm{PV}}, \langle\mu\rangle, \eta_{\mathrm{det}}) &= p_T^{\mathrm{jet}}(N_{\mathrm{PV}}, \langle\mu\rangle, \eta_{\mathrm{det}}) - p_T^{\mathrm{truth}} \\ &= \frac{\delta p_T^{\mathrm{jet}}(\eta_{\mathrm{det}})}{\delta N_{\mathrm{PV}}}(N_{\mathrm{PV}} - N_{\mathrm{PV}}^{\mathrm{truth}}) + \frac{\delta p_T^{\mathrm{jet}}(\eta_{\mathrm{det}})}{\delta \langle\mu\rangle}(\langle\mu\rangle - \langle\mu^{\mathrm{truth}}\rangle) \end{aligned} \tag{3.7}$$

and later subtracted from the total jet momentum. Equation 3.7 shows that the offset correction can be split in two parts: one depending on $N_{\mathrm{PV}}$ and one depending on $\langle\mu\rangle$. The momentum dependence on each variable is shown in Figure 3.3 before any pile-up correction (red), after the jet area subtraction (blue) and after jet area subtraction and residual pile-up correction (red). In both figures the dependence of the momentum response in the forward region is visible. If only in-time pile-up would occur, the response would be overestimated (red). But out-of-time pile-up occurs and leads to a negative energy modification, if isolated from in-time pile-up. As consequence, the transverse momentum shows a negative dependence (right). The jet area subtraction only subtracts pile-up contributions. This works for both variables in the central region, but worsens the dependence on $\mu$ in the forward region. The residual offset correction is able to correct for these issues.

### 3.2.5 Jet Energy Scale Calibration

The main calibration step is the JES calibration [11] computed using MC simulation. In this step the jet pile-up corrected jet energy is calibrated with respect to truth jets. As truth jets are not defined on data, the calibration is calculated purely with MC simulated jets and then applied to data jets. As MC simulation also include a simulation of the detector, it also models the detector issues biasing the jet energy. In Figure 3.4 a simulation of the offline jet response at pile-up corrected EM scale in comparison to truth jet energy with respect to $\eta$ for jets with different energies is shown. The various detector effects are inducing a strong $\eta$ dependency on the measured energy. As example, the $\eta$ regions with an accumulated amount of inactive material in between the detector components (e.g. in the transition range $1.4 < |\eta| < 1.6$) are indicated by

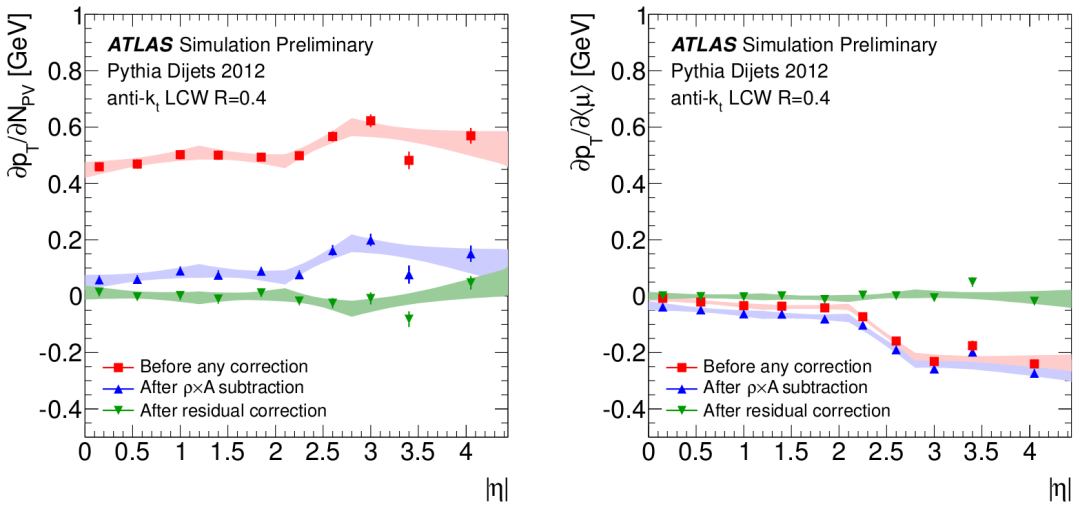


**Figure 3.3:** Transverse momentum dependency on the number of primary vertices (left) and the average number of additional interactions per bunch crossing (right), without any correction (red), after the jet area subtraction (blue) and after the residual correction (green). Taken from [12].

a drop within the resolution curve. In general, the response of jets with lower energies is worse than for jets with higher energies.

To correct for these dependencies, the energy or transverse momentum response between offline jets at pile-up corrected EM scale and truth jets is calculated in bins of truth energy (or transverse momentum) and $\eta_{det}$ using MC simulation, as shown in Figure 3.4. This response is employed to derive a correction factor depending only on the offline energy.
For the calculation, all offline and truth jets have to be matched within the distance $\Delta R = \sqrt{(\Delta\eta)^2 + (\Delta\phi)^2} < 0.3$ of each other and isolated (no jet of the same type within $\Delta R = 1$).
In the first step, the response between offline and truth jets is calculated in each $E^{\text{jet}}_{\text{truth}}$ bin i and in each $\eta_{\text{det}}$ bin j. The response in each bin (i, j) is fitted with a Gaussian distribution to derive the mean response $\left\langle R^{\text{jet}}_{\text{EMS}} \right\rangle$. As can be seen from Equation 3.3, the response depends on the energy of the truth jets. The correction depends on the energy of offline jets though. Hence, in each bin (i, j) the mean energy of offline jets $\left\langle E^{\text{jet}}_{\text{offline, EMS}} \right\rangle$ is determined from the mean of the $E^{\text{jet}}_{\text{offline, EMS}}$ distribution. A mapping in each bin i is done and yields in a response depending on the energy of offline jets in each bin j:

$$\left\langle R^{\text{jet}}_{\text{EMS}} \right\rangle \left( \left\langle E^{\text{jet}}_{\text{offline, EMS}} \right\rangle \right) \tag{3.8}$$

For the final JES energy calibration, Equation 3.8 is fitted in each bin j with an empirical function:

$$\frac{1}{c_{JES}} = F_{\text{calib, j}}(E^{\text{jet}}_{\text{offline, EMS}}) = \sum_{i=0}^{N_{\text{max}}} a_i (\ln(E^{\text{jet}}_{\text{offline, EMS}}))^i \tag{3.9}$$

where $a_i$ are free parameters, and $N_{\text{max}}$ chosen between 1 to 6 depending on the goodness of the fit.

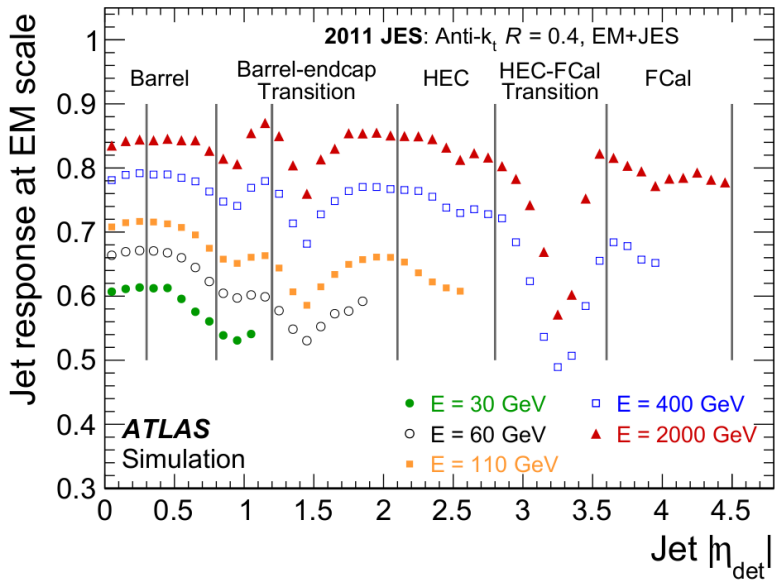


**Figure 3.4:** Jet energy response of jets with different energies as a function of $\eta$ for offline jets with pile-up subtraction and origin correction applied. Taken from [14].

The correction value $c_{JES}$ in each $\eta$-bin j is multiplied to the jet energy in each bin i. More details about the JES calibration can be found in [11]. After applying the calibration to offline jets an average uniform energy response over the total $\eta$ range is reached and the offline jets are calibrated to EM+JE scale.

### 3.2.6 Global Sequential Calibration

The global sequential calibration (GSC) is a correction calculated using MC simulation, which is applied in addition to the JES calibration to improve the jet energy resolution. The resolution of the jet energy is rather broad as the shape of a jet varies from jet to jet. Different shapes of jets can mean many things for the jet measurement. For example, if a jet is wider, it consists of more hadrons, and the energy per hadron is smaller in comparison to a jet of an equal total energy but with less hadrons. As the calorimeter response to particles with less energy is worse, the energy of the broader jet is more underestimated than the energy of the narrower jet. In addition, this effect can be enhanced or reduced depending on the $\eta$ region a jet hits and which range in $\eta$ the jet covers. As a consequence, the calorimeter response of a jet depends in addition to the jet energy and $\eta$ on the jet shape, which leads to a broad resolution.
The shape of a jet depends on the different QCD processes within the shower building, but in a first approximation on the flavor of the initiating parton of the jet. Gluon-initiated jets tend to lead to broader jets and quark-initiated jets to narrower jets. Therefore, the energy measurement of gluon-initiated jets are less accurate than the energy measurement of quark-initiated jets or, in other words, the calorimeter response is sensitive to the flavor of the initiated parton.
The sensitivity to jet flavors is reduced with the GSC. The GSC calculates corrections with respect to several global jet variables describing the shape of the jets in sequences. The following variables

are used and are corrected for in the same order as here listed:

1. The fraction of the jet energy deposit in the tile zero layer, $f_{\mathrm{Tile0}}$. A larger fraction indicates a jet deeply penetrating the detector. Those jets are mostly narrow.

2. The fraction of the jet energy deposit in the third LAr calorimeter layer, $f_{\mathrm{LAr3}}$. A larger fraction indicates a jet, which penetrates the detector shallowly. Those jets are mostly broader.

3. The number of tracks associated to a jet, $n_{\mathrm{trk}}$. A large number indicates a broad jet.

4. The width of a track jet, $width_{\mathrm{trk}}$. Wide track jets associated with a jet indicates a broad jet.

5. The number of associated muon segments, $N_{\mathrm{segments}}$. A large number indicates a high probability that the jet is not contained within the calorimeters. The energy is underestimated. This effect is also referred to as "leakage" or "punch-through".

The corrections are calculated using MC simulations in sequences. The energy response in bins of $E^{\mathrm{jet}}_{\mathrm{truth}}$ and $\eta_{\mathrm{det}}$ is calculated with respect to one of the global variables. Then, similar to the JES calibration, a correction factor is calculated by fitting the response distributions and inverting the Gaussian mean. This correction factor is applied to the jets with respect to the $E^{\mathrm{jet}}$, $\eta^{\mathrm{jet}}$ and the respective global variable. Then, the next correction is calculated with respect to the next global variable. As the corrections are calculated and applied in sequence, the variables have to be not correlated. For a detailed description of the GSC calculation see [15].
In Figure 3.5 the relative resolution ($\frac{\sigma_R}{R}$, with $\sigma_R$ the resolution and $R$ the response) of offline jets at EM+JE scale within $|\eta| < 0.3$ with respect to $p^{\mathrm{jet}}_{T,\mathrm{truth}}$ is shown. The response is shown without the GSC applied (black), with the GSC calculated with calorimeter variables applied (variable 1 and 2, red), with the GSC calculated in addition with tracking system variables applied (variable 2 and 3, green) and with the GSC calculated with all global jet variables applied (blue). The total GSC improves the resolution up to 10% to 30% for jets with a momentum in between 30 GeV to 400 GeV [15].

The GSC reduces the energy sensitivity to the flavor of the partons initiating a jet, and therefore also the jet energy uncertainty contributions due to "flavor-fluctuations". Flavor-fluctuations describes a change in the composition of jets initiated by gluons and quarks in different samples, data as well as MC simulation. As the JES calibration was calculated with a certain jet composition in the MC simulation sample, these corrections applied on a sample with a different composition would induce a bias in the jet energy. The exact bias is not known, as the flavor composition within a data sample is not known. Therefore the flavor fluctuation is estimated and taken as uncertainty with respect of the calorimeter sensitivity to the flavor. The GSC reduces the sensitivity to the flavor of a jet initiating parton, therefore the uncertainty is reduced.
The same principle works for the punch-through uncertainty. The mis-calibration of jet energies due to particles not measured within the calorimeters is not known and taken as uncertainty. The GSC reduces the sensitivity to punch-trough effects by deriving a correction with respect to $N_{\mathrm{segments}}$. And thus, the GSC reduces the punch-through uncertainty.

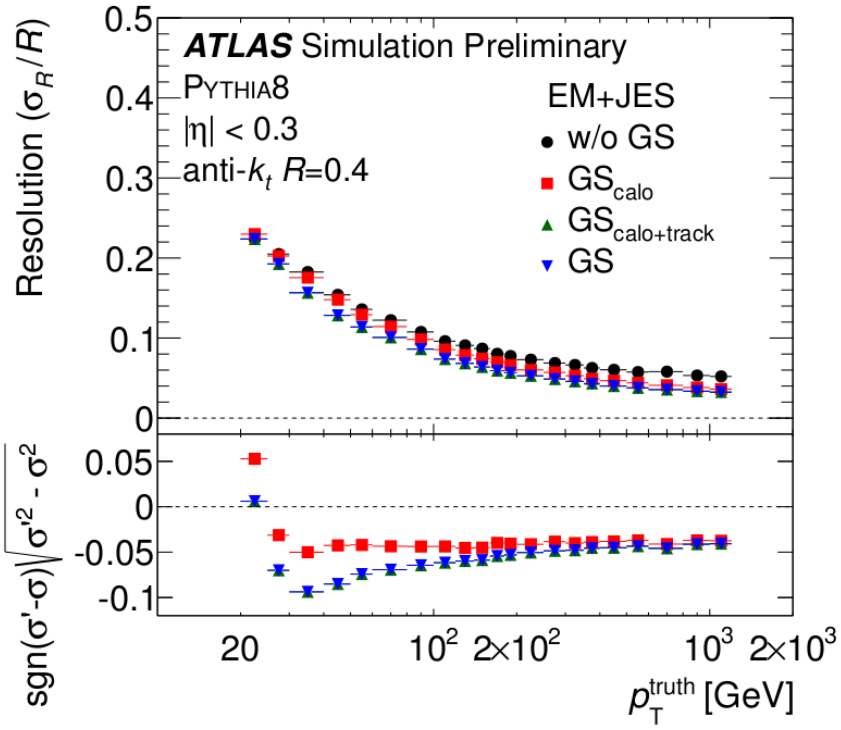


**Figure 3.5:** Resolution with respect to $p_T^{\text{truth}}$ for offline jets located in the central detector region ($|\eta| < 0.3$) at EM+JE scale (black), with the GSC calculated with calorimeter variables applied (red), with the GSC calculated in addition with tracking system variables applied (green) and with the GSC calculated with all global jet variables applied (blue). The lower plots shows the quadratic resolution deviation of the different GSC steps to resolution without GSC correction. Plot taken from [15].

### 3.2.7 In Situ Calibration

The previous calibration steps are all purely obtained using MC simulations. The simulations used in ATLAS, for the generation of events and the detector interactions, are very reliable and well produced. Still, neither are perfect. The detector simulation of e.g. inactive material is quite complicated, and the jet energy response of jets within an $\eta$ region with an increased amount of inactive material is overestimated. In addition, the detector simulation models only interactions of events produced by MC simulations. If those include other physical processes than present in data (like flavor fluctuations or new physics phenomena), the actual detector response might be different.
Further, MC simulations are only able to model physical processes to a certain degree of accuracy. These limited degree of accuracy affect the prediction of hard scatter process or the collinear splitting processes, that are included in the event simulation. Even more complicated to model is the hadronisation. These differences mainly induces slight biases for jets with low momenta, but also for the shape of jets. Events which are affected by the mis-modeling of either physical processes or detector interactions are biasing the calibration of the jet energy. To compensate for the effects introduced by the mis-modeling, the $\eta$-intercalibration and absolute in situ calibration are applied.

#### $\eta$-intercalibration

The $\eta$-intercalibration, or relative in situ calibration, accounts for mis-modeling of detector effect by calibrating jets in the forward region using jets in the well calibrated (and modeled) central-region. The simple approach exploits the dijet balance technique [14].
In the dijet balance technique, the momentum of a probe jet is compared to the momentum of a reference jet in a dijet event. In a dijet event only two energetic jets are created and both jets have the same transverse momentum due to transverse momentum conservation. Therefore, the mean asymmetry A

$$A = \frac{p_T^{\text{left}} - p_T^{\text{right}}}{p_T^{\text{avg}}} \tag{3.10}$$

is supposed to be zero. Under the assumption that the forward region is modeled worse, any deviation from zero indicates a wrong or missing correction in the forward region. The asymmetry is used to compute the response of the probe jet with respect to the reference jet and is calculated in bins of $\eta^{\text{jet}}_{\text{probe, det}}$ and $p_T^{\text{avg}} = (p_T^{\text{probe}} + p_T^{\text{ref}})/2$:

$$\frac{1}{c^{\text{probe}}} = \frac{2+A}{2-A} = \frac{p_T^{\text{left}}}{p_T^{\text{right}}} \tag{3.11}$$

The factors $c^{\text{probe}}$ is the $\eta$-intercalibration correction factor. If the asymmetry is zero, the correction is equal to one, as it is in the central region.
In ATLAS the jets are compared to truth jets, therefore the correction factors are calculated in MC simulation and data, and the ratio $f(p_T, \eta) = c^{\text{data}}/c^{\text{MC}}$ is applied to the energy of data jets for the final calibration.
In the simple approach, one of the leading jets has to be within $|\eta| < 0.8$, which reduces the amount of events significantly, especially for probe jets in the forward region. This increases the

uncertainty on the correction factors. Therefore, the matrix method [14] is used instead. In this method all jets are calibrated with each other, regardless of their location within the detector. This approach leads to different $\eta$-intercalibration factors $c$, but the data-to-MC simulation ratio $f(p_T, \eta)$ of the correction factors is equal to the dijet-balance method ratio [14].

The main challenge for a reliable and valid $\eta$-intercalibration is the definition of a pure dijet data sample as well as to obtain enough events in all $\eta$ and $p_T$ regions (with $p_T > 7$ GeV). Only events with jets calibrated to EM+JE+GSC scale, that fulfill all standard jet quality requirements (see section 3.3) are used. Most importantly, only "real" dijet events have to be used: if a third jet is produced in an event, the balance between the first two jets is distorted and the fundamental assumption of the dijet-balance method or matrix method is not valid. The same holds for jets not produced in a proton interaction (e.g. cosmical rays) or with additional energy due to pile-up events.

#### Absolute In Situ Correction

The "absolute" in situ correction [16] accounts for mis-modeling of physic effects that are affecting the response of jets. In here, the response between a jet and a recoiling object is measured, similar to the dijet balance method used for the $\eta$-intercalibration, and the ratio of the responses in data and MC simulation is applied as a correction to the energy of data jets. In this way, the effect of different modeling of e.g. FSRs is accounted for, as these would disturb the balance of two recoiling objects. The recoiling object is chosen depending on the jet energy. For jets with $20 \leq p_T \leq 200$ GeV the balance to well calibrated Z bosons, for jets with $30 \leq p_T \leq 800$ GeV the balance to photons and jets with $300 \leq p_T \leq 1700$ GeV the balance to many (in situ corrected) jets with lower transverse momenta is exploited.
The calculation of the corrections depend on the quality of the data sets used, as fake jets or third jet radiations would distort the balance between the recoiling objects artificially. The jets within the data set used are calibrated with all preceding calibration steps in the calibration chain. These methods are all called absolute in situ calibration.

### 3.2.8 Jet Energy Scale Uncertainties

The jet energy scale uncertainty is the dominant uncertainty contribution for many measurements using jets. The reason for this is the power law of the jet cross sections: the differential cross section follows the function form $E^{-\alpha}$ with $\alpha \propto 4$ to 7. Thus, even small uncertainties on the jet energy lead to large uncertainties on the cross section.
Many sources contribute to the JES uncertainty, all estimated with in situ methods. The in situ corrections account for differences between MC simulation and data, and therefore the only remaining uncertainties on the JES calibration are the uncertainties regarding the in situ methods. The uncertainties can be grouped into detector based (e.g. material uncertainties), model based (e.g. influence of kinematic selections or difference between MC generators), based on a mix of these sources (e.g. uncertainty regarding the baseline of the photon energy scale) and statistical uncertainties. In total, 23 systematic sources and 35 statistical sources from in situ methods

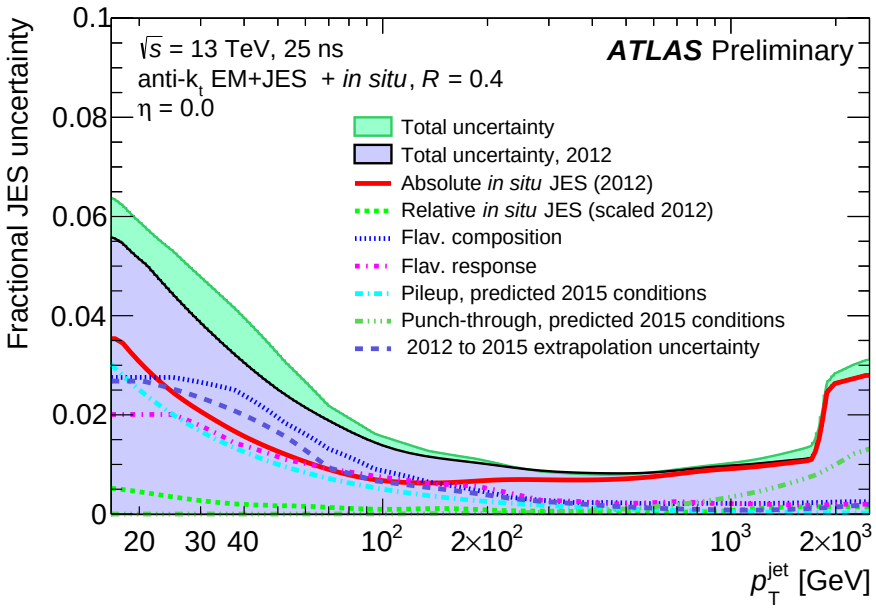


**Figure 3.6:** The total JES uncertainty for offline jets within $|\eta| < 0.8$ in a dijet data sample. Taken from [13].

contribute to the JES uncertainties [16].
In addition to the systematic and the statistical sources, the in situ methods depend on the jet-flavor composition as well as the pile-up condition within the data sample used for the calculation. As these can be different within the data sample used for the analysis, the calibration constants would not be ideal for the jets used in the analysis. The differences regarding the flavor composition and the pile-up conditions within the different samples is estimated and taken as uncertainty.
A last uncertainty contribution is attributed to jets with $p_T > 1700$ GeV jets, that cannot be correct with in situ methods. These uncertainties are calculated with the single-hadron response [16], another in situ method in which a single hadron of a jet is balanced to its associated tracks. The main idea is that the quality of a simulated jet depends on the simulation of its constituents. Deviation between MC simulation and data are used as uncertainty for jets with high $p_T$.
The JES uncertainty and its main contributions for a dijets-sample recorded in 2015 for offline jets within $|\eta| < 0.8$ is shown in Figure 3.6. The uncertainty is highest for low $p_T$ (6%), moderate for 200 GeV$< p_T <$ 1800 GeV (1%), and increased for $p_T >$ 1800 GeV (3%).

## 3.3 Quality Selection

In a jet measurement, only jets created in the current hard scatter event are of interest. Pile-up jets and "fake" jets created by electrical noise, cosmic ray or beam background, would bias any measurement and need to be removed. Pile-up jets are subtracted at cell level and in the calibration, and fake jets are removed during the event and the jet quality selection.

### 3.3.1 Event Quality Selection

The event quality selection removes the number of events in which major problem within the detector or within the beam occurred. The quality selection recommended by the ATLAS collaboration [9] contains of the Good Run List (GRL), which list all events recorded with a stable beam, and criteria indicating a fake or corrupted event due to calorimeter malfunctions.
One possible malfunction in calorimeters are noise bursts. These bursts happen in calorimeter cells, which then record high voltages independent to a signal, because of pollution in the detector or electrical failures. The energy reconstruction of a cell with large noise is not possible, and therefore events containing a high ratio of noisy cells, are marked with a flag (LArTimeVeto). Noise burst only occur in LAr calorimeters.
Events during which other malfunctions within the LAr and tile calorimeters occur are marked by flags as well. In total, the following flags indicate calorimeter malfunctions:

- LArError: This flag is set,
    1. when the event is recorded during a time in which a noise bursts or other data corruptions have been observed in the LAr calorimeter(LArTimeVeto).
    2. when the information of relevant LAr cells are missing (LArBadFebMasking).
- TileError: This flag is set, when the read out of the tile detector is incomplete.

If any of these flags are set, the event is likely to be of poor quality and should be excluded from any analysis. A last quality criteria for a hard scatter event is based on the number of primary vertices ($N_{PV}$). All proton-proton interactions create a PV, so an event without PV needs to be excluded.

### 3.3.2 Jet Quality Selection

The jet quality selection is done in each event for every jet. Each jet has to pass a quality selection to reduce the non-collision background. The quality selection is based on variables with discriminating power between "good" collision jets and "bad" fake jets. A good jet deposits at least a small fraction of energy $f_{EM}$ in the EM calorimeter with associated tracks. Further, the shape of a signal pulse in a calorimeter cell is well defined. Fake jets behaves differently.
Beam background events, beam gas or beam halo interactions, are interactions of protons within the beams, that interact with the accelerator tunnels or other particles outside the designed interaction point. Muons created in these interactions reach the detector, and while they seldom pass the tracking system, they deposit energy in the calorimeters. By requiring a fraction of the jet energy (of charged particles) to be deposit in the tracking system $f_{ch}$, their influence is reduced.
For fake jets produced by cosmic rays, the tracking system is rarely hit as well, and they tend to deposit their energy in one calorimeter layer only. A restriction on the maximal energy fraction of a jet inside one calorimeter layer ($f_{max}$) is applied.
Another source of fake jets are noise bursts. If too many cells are noisy, the event is already excluded in the event quality selection. Otherwise, a noise burst can be clustered into an own topo-cluster and consequently into an individual fake jet or it can be clustered to a good jet, which would increase the energy immensely. If this noise burst is permanently or very pronounced, they

are either seen in the number of jets inside the $\eta - \phi$ plane (occupancy plots) or in the mean jet energy in the same plane as strong deviations. If those deviations are seen in a cell, the cell is called a "hot cell" and masked, which means they are excluded from the jet reconstruction.
Sporadic, not too noisy bursts are still contained in the jets and need a special quality selection. As the induced signal is produced by an electrical malfunction, these cells in the EM calorimeters can be distinguished from good jets by the shape of the distorted pulse. To decide, if a cell is biasing the jet energy, an average jet quality $\langle Q \rangle$ (from 0 to one, with 0 meaning good quality) variable is introduced, which is calculated during data taking and takes various jet information about the calorimeter cell pulse into account. If the quality of the bad jet is too low and the jet energy fraction in a poorly shaped LAr cell ($f_Q^{EM \text{or} HEC}$) is too large, the jet is excluded. The quality criteria for the electromagnetic and hadronic LAr calorimeters are different and depend on the fraction of energy deposit in the layers ( $f_{HEC} > 0.5$ or $f_{EM} > 0.95$). As noise bursts produce also negative energy, an other criteria is the amount of negative energies $E_{neg}$ included in the jet. These different cuts are summed up in the quality criteria. As not all measurements are sensitive to fake jets, whose rate is rather low to begin with, differently strong criteria for the quality exist. The used criteria for offline jets is the "BadLoose Cleaning". Jets fulfilling the following criteria are bad jets and should not be used for a jet analysis [9]:

1. $f_{HEC} > 0.5$ and $|f_Q^{HEC}| > 0.5$ and $\langle Q \rangle > 0.8$
2. $|E_{neg}| > 60$ GeV
3. $f_{EM} > 0.95$ and $|f_Q^{LAr}| > 0.8$ and $\langle Q \rangle > 0.8$ and $|\eta| < 2.8$
4. $f_{max} > 0.99$ and $|\eta| < 2$
5. $f_{EM} < 0.05$ and $f_{ch} < 0.05$ and $|\eta| < 2$
6. $f_{EM} < 0.05$ and $|\eta| \geq 2$

The first two criteria reduce the noise induced background. The third criteria reduces jets due to large coherent noise or pathological cells in the LAr calorimeters. And the last three more general criteria reduce the beam background and cosmic ray events.

# Chapter 4

# Monte Carol Simulation and Data Samples

For the different studies and tests presented in this thesis, I used data recorded in 2015 between June and November and data recorded in 2016 between April and November, as well as MC simulations. In this chapter a short overview over the different samples is given.

### Data Samples

All test that are based on data, are performed using main stream data containing jet events either recorded in 2015 or 2016. The used 2015 data amount to an integrated luminosity of $\int \mathcal{L} = 3.3$ fb$^{-1}$[18]. The used 2016 data amount to an integrated luminosity of $\int \mathcal{L} = 33.9$ fb$^{-1}$. For tests with 2016 data, the samples are differentiated by run periods and single runs (chapter 2). The data used are:

- run 300800, a run of period F - representing $\int \mathcal{L} = 0.81$ fb$^{-1}$
- period F - representing $\int \mathcal{L} = 3.0$ fb$^{-1}$

### Monte Carlo Simulation

The MC simulation samples created in 2015 are used for various tests and cross checks in this thesis. They are generated by the LO event generator Pythia8 [32]. This generator models hard and soft interactions, parton distributions, ISR and FSR parton showers, multiparton interactions, fragmentation and the decay of particles. A higher jet multiplicity in an event is only archived through FSR and ISR. For the hard scatter and the hadron shower description the LO parton distribution function NNPDF2.3 [32] is exploited. Geant4 is used for the detector simulation.

# Chapter 5

# 2015 Trigger-Object Level Analysis

The concept of looking for new particles decaying into a pair of jets is historically well established. Simple dark matter theories, for example, often predict a new boson, which would interact with quarks and thus generate a resonance in the dijet mass spectrum (section 1.2). The sensitivity of these searches at higher masses (above 1 TeV) are limited by the number of dijet-events with respectively high invariant masses produced in the LHC. But for searches for low mass mediators the prescale factors on the jet triggers, which need to be applied due to large QCD contributions and a restricted bandwidth capacity, is the limiting factor. Only a fraction of all dijet events at lower invariant dijet masses are recorded. This prevents standard offline searches to probe the dark matter theories with lower coupling strengths.
The Trigger-object Level Analysis (TLA) is a search for new physics at low dijet masses with a new strategy to bypass the limitation. This strategy uses only information about the online reconstructed jets and some jet structure variables based on calorimeter information. An event containing only this information is written out to a special data stream with only 10 kB/event. The rate of events written to the data scouting (DS) stream is ten times as big as the rate of events selected by all single jet trigger combined (see Figure 5.1). This increase in rate is not only valuable for the TLA, but for any jet measurement at lower energies.

In 2015, the TLA was performed successfully for the first time in ATLAS . Even though no resonance was found, new limits where set and, which is most important, the eligibility of HLT jets for physical analysis was demonstrated. A summary of the 2015 TLA is given in this chapter, starting with a description of the main challenge in the TLA, the missing information in the DS stream. Further, the signal region, the calibration scheme of HLT jets in 2015 and the search strategy are described. Finally, the results of the TLA are summarized.

## 5.1 Information in the Data Scouting Stream

The rate of the DS stream is coupled to the size of information saved in there. Any tracking or detailed calorimeter information to be written out increase the event size such that a reduction

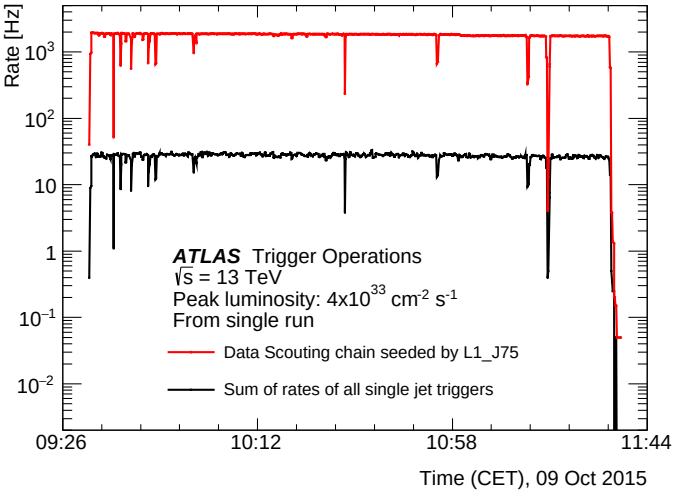


**Figure 5.1:** Trigger rate for the DS chain seeded by L1-J75 compared to the sum of the rates of all prescaled and unprescaled central single jet triggers during a single data run. Taken from [18].

of rate becomes necessary. Hence, only information about the reconstructed jets at trigger-level (section 2.6), the HLT jets, are stored. These information include the four-momentum of the HLT jets and some variables with information of the detector in the relevant range, like timing of the signal, quality of the jet and some structure variables (e.g. fraction of the jet energies in certain calorimeter layers) are saved.

The small amount of information is the key to higher statistics in the low (dijet-)mass region in ATLAS, but it is also the main challenge of the TLA. The reconstruction, quality selection and calibration of offline jets is well established and validated, but needs information about the cells included in the jet, the muon system and the tracking system. Consequently, HLT jets can not be reconstructed and calibrated the same way as offline jets and the quality criteria has to be modified.

The challenge is to validate the performance of HLT jets. The simple approach is to compare HLT jets to offline jets. Both are reconstructed with the anti-$k_T$ algorithm and topo-clusters. Small differences in reconstruction and quality selection might cause discrepancies, and need to be evaluated. However, the biggest discrepancy is caused by the calibration. The TLA calibration scheme follows the offline calibration scheme as close as possible, but some calibration steps are impossible with only calorimeter information. Therefore, HLT jets are additionally calibrated to offline energy scale via data derived scale factors to account for missing calibration steps.

The differences in reconstruction and quality selection is discussed in chapter 6. This section includes an overview of the calibration scheme in the 2015 TLA. The calibration scheme for the 2016 TLA and my validation study is discussed in chapter 7; the calibration schemes are slightly modified, reacting to a difference in the jet reconstruction as well as a GSC specifically calculated for HLT jets.

## 5.2 Signal Region of the TLA

The TLA is a new physics search using dijet events. Jets are selected using the BadLoose Quality criteria adapted for HLT jets (see chapter 6) and the L1-J75 trigger.
Events fulfilling the following requirements are selected ([18]):

1. $N_{\text{jets}} \leq 3$ (number of jets)
2. $|\eta| < 2.8$ for leading and subleading jet
3. $p_T > 185$ GeV for leading jet
4. $p_T > 85$ GeV for subleading jet
5. $p_T > 50$ GeV for third-leading jet

These criteria are optimized to suppress (QCD) background and pile-up events. In addition, two different requirements regarding the angular separation of the two leading jets $y^* = (y_1 - y_2)/2$ are set to define two different signal regions: $y^* < 0.6$ OR $y^* < 0.3$. The angular separation criterion ensures that the selected events are dijet events in the central region.
The selection of the leading jet ensures that the trigger efficiency of the L1-J75 trigger is above 99.5% (see section 2.6). I determined this point by fitting the efficiency curve of the L1-J75 with respect to L1-J15. The efficiency curve is determined by dividing the number of events passing the L1-J75 and L1-J15 by the number of events passing the L1-J15 only. The fit function depends strongly on the range of the curve. As the turn-on point is the main interest, the fit range is optimized to describe the area around 100% efficiency, from $130 - 285$ GeV, and not the total efficiency curve. In Figure 5.2 the curve plus fit and the fit range are shown. The fit function returns $p_T = 182.513$ GeV as point for the 99.5% efficiency point. For the cut on the leading jets $p_T$ the value was rounded up to 185 GeV.

A selection on the leading jet $p_T$ biases the invariant mass distribution of two jets, as shown in Figure 5.3 and the biased region has to be excluded from the TLA signal region. I estimated the lower limit of the unbiased mass region by comparing $m_{jj}$ distributions of MC simulations for HLT jets with (purple) and without leading jet $p_T$ cut (green). The jets were selected with the $y^* < 0.6$ criterion. A lower mass limit of 443 GeV was found. Consequently, the TLA investigates the invariant mass distribution of dijets in a range of 443 to 1236 GeV.

## 5.3 HLT Jet Calibration Scheme in 2015

The TLA was performed on data recorded in 2015 for the first time. The calibration scheme of HLT jets includes the following steps:

1. jet area pile-up subtraction
2. dedicated JES calibration
3. offline $\eta$-intercalibration
4. data derived scale factors

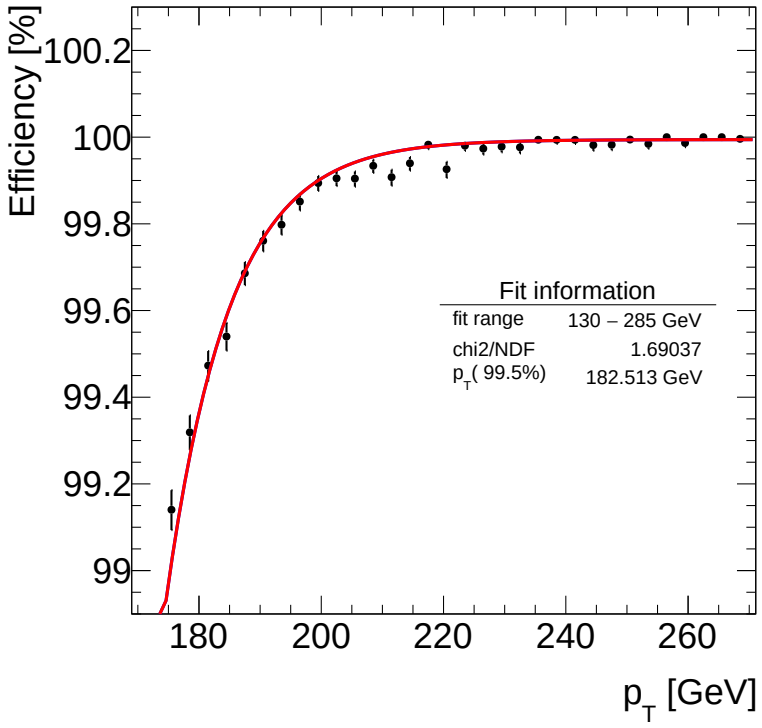


**Figure 5.2:** Fitted efficiency curve of trigger L1-J75 with reference trigger L1-J25.

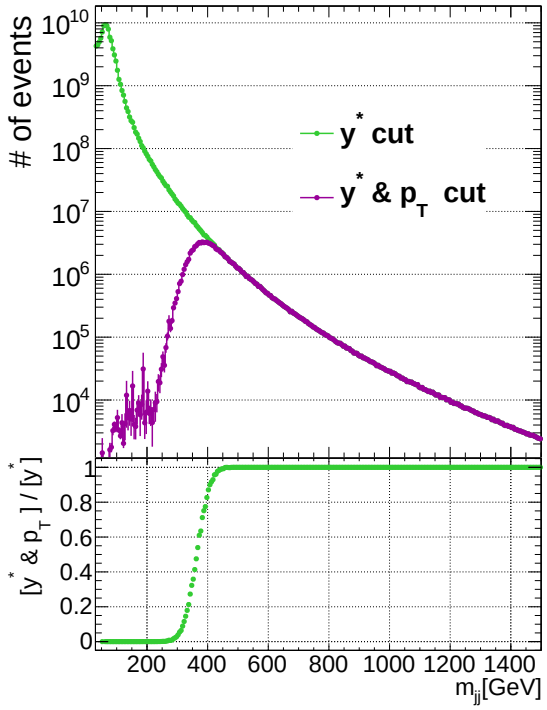


**Figure 5.3:** MC simulated dijet invariant mass distribution for HLT jets selected with a $y^*$ cut and with (purple) and without (green) a leading jet $p_T$ cut of 185 GeV. The lower plot shows the ratio of both $m_{jj}$ distributions.

5. offline absolute in situ corrections

The TLA calibration follows as close as possible the procedure of the offline calibration. Due to the missing information from the tracking system and the muon chambers, no residual offset correction, no origin correction and no GSC ([18]) can be applied. In addition, due to the less efficient pile-up subtraction and a looser quality criteria (explained in more details in chapter 6 and chapter 7), no HLT dedicated absolute or relative in situ corrections are applied. Instead, the offline calibrations and a new calibration step, the data derived scale factors are applied.
Out of the three missing calibration steps, the residual offset correction is the only one that affects the jet energy scale. The others would improve the jet energy resolution, but as the TLA is not a precision search, the absence of the GSC or the origin is no serious problem for the TLA. The residual offset correction influences jets in the forward region greatly, but HLT jets contained in the TLA signal region only slightly. In here the regions mostly influenced are at low jet $p_T$, where more HLT jets are expected and inside the transition region, which is due to the higher amount of dead material in the calorimeter more sensible to pile-up events.
The data derived scale factors, which correct the HLT jets to offline energy scale, is derived: For this purpose all preceeding calibration steps are applied to HLT jets and all respective calibration steps are applied to offline jets (including GSC). The response of matched HLT and offline jets is inverted and smoothed to calculate the scale factors. These scale factors are then applied to the energy of each HLT jet. In data recorded in 2015, the difference between HLT and offline jet energy is about 4%.
The following absolute in situ correction addressing theory biases in MC simulations are not calculated specifically for HLT jets, because HLT and offline jets are at this step at the same energy scale. In Figure 5.4 the response of HLT and offline jets after applying the respectively calibration chain are shown. Both responses show an agreement better than 1%. This proofs, that HLT jet are successfully calibrated to the same energy as offline jets and therefore validates the TLA calibration chain.

## 5.4 HLT JES Uncertainties

The energies of HLT jets are similar to energies of offline jets, therefore the uncertainties of offline jets are used for HLT jets. In addition, because of the missing calibration steps, the offline jets uncertainty is calculated with these changes:

- **pile-up uncertainty:** An additional pile-up uncertainty is included for HLT jets to account for the missing residual calibration step.
- **flavor uncertainty:** The GSC reduces flavor sensitivity in the calorimeter response. As this correction was not applied on HLT jets, a different flavor composition in the data sample with respect to the MC simulations are a major uncertainty (subsection 3.2.6).
- **punch-through uncertainty:** The GSC also accounts for jets not contained within the calorimeters. The number of jets in the TLA signal region which would be corrected by this correction is negligible ([18]).

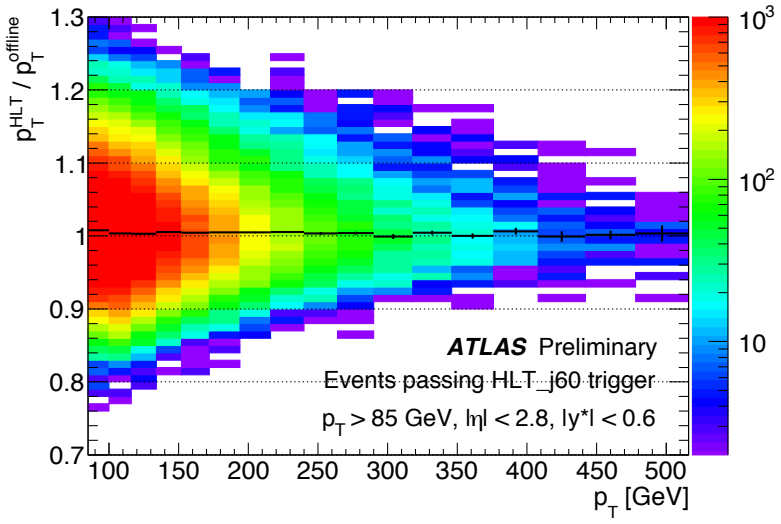


**Figure 5.4:** Transverse momentum of HLT jets compared to offline jets as a function of $p_T$ in range $|\eta| < 2.8$. Events are selected by HLT-j60 and by requiring a leading jet with $p_T > 185\,\text{GeV}$

- **non-closure uncertainty:** As the calibration scheme for HLT jets is new, eventual miscalibrations are possible and result in a non-closure between HLT and offline jets. An uncertainty of the same magnitude as the data derived scale factors, which are also an estimate for the biased induced due to the TLA calibration chain, are applied as a conservative contribution to the jet energy scale.

The JES uncertainty for HLT jets is shown in Figure 5.5 in comparison to offline absolute JES uncertainty (light green). The main uncertainty in 2015 is the flavor uncertainty.

## 5.5 Signal Search Strategy

The TLA searches new physics in the dijet invariant mass spectrum, similar to more familiar searches at high dijet masses [33]. The SM prediction for the invariant dijet mass spectrum is a smoothly falling distribution. An additional process like the creation of dark matter mediator particles would cause a deviation from the SM background. Such a deviation would be visible as a resonance in the mass spectrum.
The SM background is determined with a global fit over the mass range 443 to 1236 GeV with the four parameter $p_i$ function

$$f(z) = \frac{p_1}{z p_2} e^{-p_3 z - p_4 z^2} \tag{5.1}$$

with $z = m_{jj}/\sqrt{s}$.
The function and seven others were evaluated of their capability to describe the SM background using MC simulations. Equation 5.1 was found to be the most stable one and used for the search phase in data.
A resonance in the mass distribution is searched for with the "BumbHunter algorithm". The performance is tested by examining whether the algorithm finds a resonance, whether a signal is included or whether an artificial resonance is created due to statistical fluctuations or a mis-

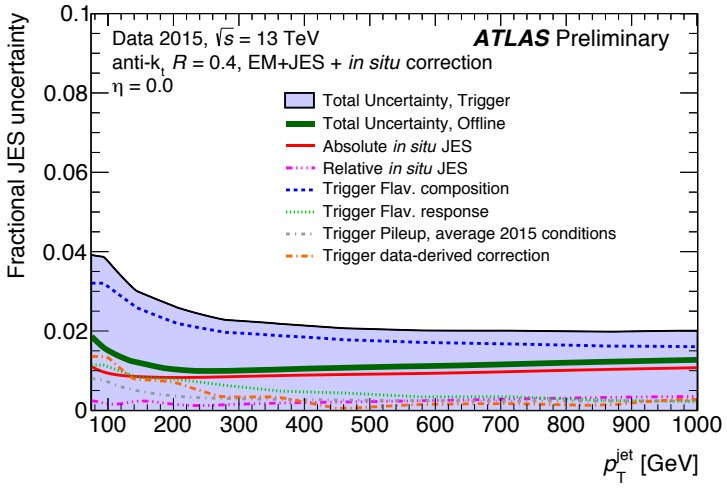


**Figure 5.5:** Jet energy uncertainties for central HLT jets ($\eta = 0$) compared to offline jet energy uncertainties. "Absolute in situ JES" refers to in situ uncertainties and "relative in situ" refers to $\eta$-intercalibration uncertainties. Taken from [18].

calibration. As a example, I tested whether a mis-calculation of the scale factors would result in a fake resonance. The test is described in Appendix A.

## 5.6 Results of the 2015 analysis

The TLA is the first ATLAS search which has successfully used HLT jets containing only calorimeter information. No new particles, dark matter mediators or other particles creating a Gaussian resonance on top of the dijet mass spectrum, were found. Instead, new limits for signals of new physics are set: At 95% credibility level, dark matter particles and any kind of new particles creating a Gaussian like signals on top of the dijet mass distribution in the TLA signal region with cross sections ranging from approximately 3 pb for masses of 450 GeV, to 9 pb for masses of 600 GeV, to 0.7 pb for masses of 850 GeV region are excluded [18]. The analysis is redone using data recorded in 2016 with more luminosity and an improved calibration scheme for HLT jets.

# Chapter 6

# High-Level-Trigger Jet Reconstruction and Quality Criteria

The use of HLT jets in a new physics search is a new concept, and the reconstruction, quality selection and calibration has to be validated. The validation was done before with respect to data recorded in 2015, but for data recorded in 2016, a new feature for the HLT jet reconstruction is introduced. The change in the jet reconstruction propagates to a change in the TLA jet calibration scheme. Therefore, the new 2016 TLA calibration scheme for HLT jets is discussed in this and the next chapter.
The 2016 TLA is not yet published, and in following only my work and for my studies relevant work of the 2016 TLA are presented. This chapter discusses the differences in jet reconstruction, event and jet quality criteria used for DS stream data recorded in 2016 in comparison those used for main stream data and their effects on the HLT jet energy measurement in the TLA. First, the new feature of the reconstruction of jets is presented: the BCID dependent pile-up correction. The remaining differences, the timing and energy calculation for the tile calorimeter are introduced next. Then, the event quality for DS stream data is presented and validated. Finally, some jet quality variables and methods that are not contained in the DS stream are discussed with respect to the quality of HLT jets: the calorimeters flags, the primary vertex cut and the hot cell masking.

## 6.1 Reconstruction of HLT Jets in 2016

HLT jets are reconstructed during data taking and can not be redone after data taking with DS stream information. The offline jet reconstruction is done after data taking with slight changes in the calorimeter energy reconstruction. These changes differentiate the HLT jet reconstruction to the offline jet reconstruction.
In 2015, these changes consisted of the BCID dependent pile-up subtraction and the pedestal correction of the tile calorimeter cell. In 2016 though, the BCID dependent pile-up correction is applied for the first time in HLT jet reconstruction and the only difference remaining is the

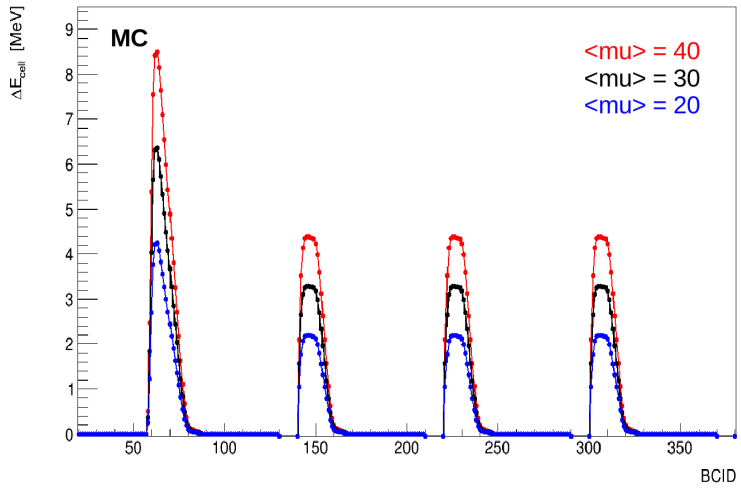


**Figure 6.1:** BCID dependent energy correction for one calorimeter cell for different number of additional interactions per bunch crossing $\langle\mu\rangle$. Taken from [22].

pedestal correction in tile.

### BCID dependent Pile-Up Subtraction

The BCID dependent pile-up subtraction calculates the average BCID dependent pile-up per calorimeter cell (section 2.4) over the respective calorimeter layers, and subtracts it from the cell energies during the cell energy reconstruction. In Figure 6.1 a simulated BCID dependent energy correction of a LAr cell is illustrated over a few bunch trains for different numbers of additional interactions per bunch crossing. As can be seen, this pile-up effect only influences the first bunch crossings in each bunch train, where the bipolar pulse shapes are not (yet) averaged out. However, this effect is reduced when the distance between bunch trains is shorter than the pulse shape as the negative parts of signals from the previous bunch trains dampens the effect. Hence, the energy correction is largest in the first bunch trains. The BCID dependent pile-up correction has to be calculated for each calorimeter layer, as the bipolar pulse form is adapted to the different amount of expected pile-up effects.

### Tile Calorimeter - Energy and Timing Calculation

In the tile calorimeter a signal pulse is shaped with constant weights (see section 2.4). The energy of the pulse is proportional to the amplitude of the pulse. The amplitude is calculated depending on the noise pedestal inside the cell. The timing of the signal corresponds to the phase of the pulse and the phase is calculated within the same algorithm as the energy depends on the pedestal and on the amplitude. In the HLT, the tile cell energy is reconstructed with a constant pedestal, taken from the database. However, the tile cell offline energy is reconstructed using a pedestal that is calculated in situ to account for pile-up fluctuations and recalculated for every event.
As consequence, the reconstructed energy and the timing of a tile cell is different in the online and offline reconstruction, as both variables depend on the pedestal value. As the timing depends more

strongly on the pedestal value, the difference between online and offline timing is very significant, while the energy difference between online and offline reconstruction is negligible. As consequence to this difference, the TLA is not using the timing information in any cross checks. The slight changes within the energy, which are not expected to be significant, are still corrected for by the TLA calibration scheme with data derived scale factors (subsection 7.4.2).

## 6.2 Event Quality Selection for the DS Stream

In the ATLAS detector technical problems can occur. Most of them are minor ones (like noise bursts) but some are more grave and distort or fake data. The event quality selection removes these events. However, the DS stream only contains calorimeter information concerning jets directly, so the standard offline event quality selection as described in subsection 3.3.1 can not be applied. For example, the LArError and the TileError flags are calorimeter information not connected to the jets and the $N_{PV}$ cut requires tracking system information.
For the events written to the DS stream, only the Good Run List and a noise-burst-time-veto (TLALArError) are applied. In order to validate this event quality selection for the DS stream, I studied the number of events excluded through standard offline quality selection and compared them with number of events excluded by the event quality selection of the DS stream. The tests are performed on 2015 data containing dijet events. It is assumed, that there is no significant different behavior between 2015 and 2016 data with respect to the rate of poor quality events, thus the results shown in the following are assumed to be valid for 2016 data as well. Similar tests performed on 2016 data are currently in progress.
The first test I performed studied the effect of the missing LArError. For the DS stream a partial replacement for the LArError, which marks corrupted or missing events in addition to events that coincide with many noisy cells, is created. The TLALArError excludes all events that coincide with a noise burst by comparing the time stamps of the noise bursts, that are written to the database during data taking, and the event time stamp. In Figure 6.2, the number of events excluded by LArError and TLALArError (top-right), the number of events excluded by LArError but not TLALArError (bottom-right), and the number of events not excluded by either of the vetos (bottom-left) are compared to each other. Only 41 events out of 14890 events are not excluded by the TLALAr but by the LArError. Which means that only 0.2% of all LArErrors are not induced by noise bursts but by missing data within cells. By applying the TLA signal criteria (chapter 5) the number of events excluded by the LArError but not TLALArError are reduced to 3 events in total. This means that the fraction of events with missing LAr calorimeter cell data that contributes to the TLA is below 1E-10 and consequently negligible.

For the TileError flag this test was not redone, as the high-mass dijet analysis [33] already estimated the fraction of poor quality events. Less than 0.01% events exhibit data corruption in the tile calorimeters. Hence, the fraction of bad quality events due to tile calorimeter malfunctions is deemed negligible for the TLA.
The last event quality criterion that is not applied to the DS stream data, is to have at least one PV in an event. To estimate the fraction of events with less than one PV, I have studied the signal region of the TLA in data recorded in 2015. The result is shown in Figure 6.3, which shows the

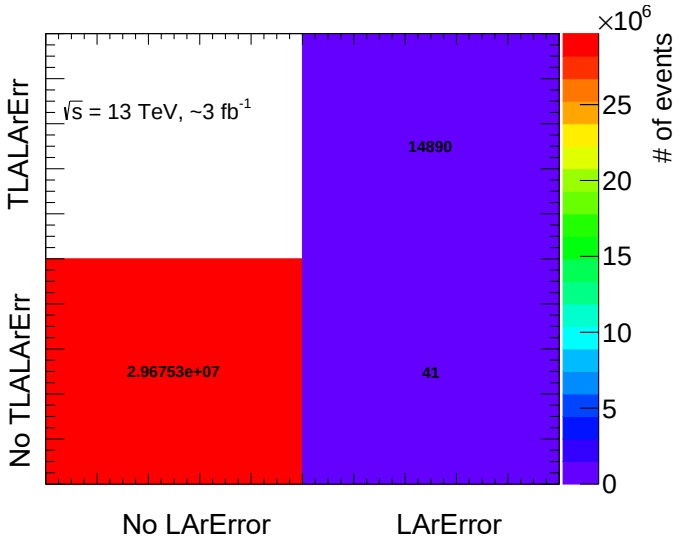


**Figure 6.2:** Comparison of LArError and TLALArError with main stream data.

leading jet $p_T$ and the leading jet $\eta$ distribution of events with at least one PV (light purple) and with less than one PV (dark purple). Less than 0.01% of all events have no PV. The effect of the missing NPV selection is therefore assumed to be negligible.
To summarize, due to the missing quality criteria some poor quality events are still used for the TLA. The fraction of these events is negligible though, and they have no significant effect on the shape of the jet energy and $p_T$ distributions.

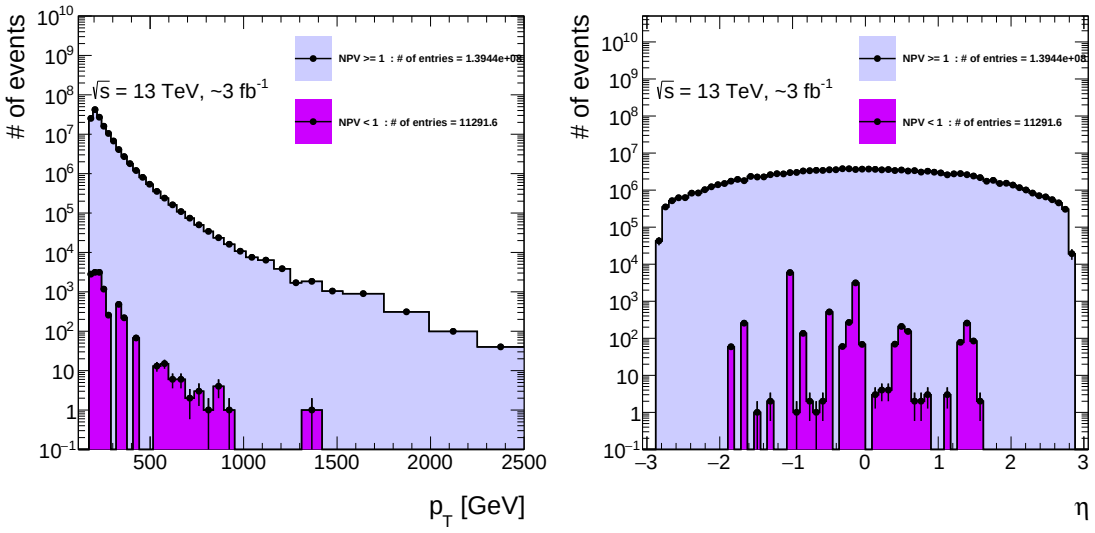


**Figure 6.3:** Leading offline jet $p_T$ (left) and the leading offline jet $\eta$ distribution (right) of events with at least one primary vertex (light purple) and with less than one primary vertex (dark purple). All events passed the TLA signal selection.

## 6.3 HLT Jet Quality Selection

The offline BadLoose quality criteria without the charged fraction criterion ($f_{EM} < 0.05$ and $f_{ch} < 0.05$) is applied to HLT jets to reduce the non-collision backgrounds (see section 3.3). This slimmed quality criteria is the HLT jet quality criterion. The tests to ensure that no large bias is induced due to the missing quality criteria were done in the course of the 2015 TLA [18].

### Hot Cell Masking

An issue not discussed in the 2015 TLA are hot cells. As mentioned in section 3.3, cells that fire due to electrical failures, are called hot cells. As they can fake jets or bias the energy of good jets, hot cells are usually masked before the jet reconstruction. As this masking is only done offline, it is not included in the reconstruction of HLT jets.
For offline reconstruction, hot cells are found via the express stream. $\eta - \phi$ maps of offline jets are filled in the express stream with the HLT-j25 trigger [3] and if a hot cell is seen, it is masked before the bulk reprocessing (subsection 2.6.3). Figure 6.4 shows the jet occupancy, i.e. the number of measured jets, as a function of $\eta$ and $\phi$, in the express stream of the data run 300800. A hot cell at ($\eta \approx -1.8$, $\phi \approx 1.6$) is dominating the occupancy plot after the express processing (left). After the bulk processing (right) the cell is not included in the jet reconstruction anymore. The amount of reconstructed jets at ($\eta \approx -1.8$, $\phi \approx 1.6$) is reduced from $70 \times 10^3$ to $4 \times 10^3$.
In Figure 6.5, the mean jet transverse momentum as a function of $\eta$ and $\phi$, in the express stream

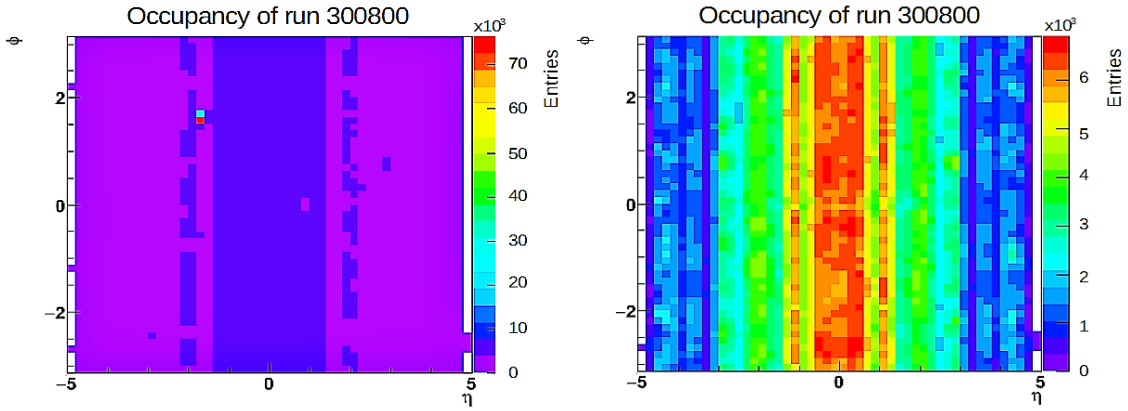


**Figure 6.4:** Occupancy plot after the express reprocessing (left) and the bulk reprocessing (right) for run 300800, events are triggered by the HLT-j25. Taken from [4].

of the data run 300800 is shown. After the express reprocessing (left) the maximal mean $p_T$ is around 45 GeV, while after the bulk reprocessing (right) the maximal mean $p_T$ is around 40 GeV. In here no strong hot cell is, seen only a slight increase of $p_T$ around 5 GeV in the same bin as the hot cell located in the occupancy plot is visible.
The observation that the hot cell in run 300800 has an effect on the occupancy of jets, but rarely on the average $p_T$ indicates that the hot cell was caused by permanent noise. If a hot cell is caused by sporadic but strong noise, a more prominent effect on the average $p_T$ map is expected and less in the occupancy plot.

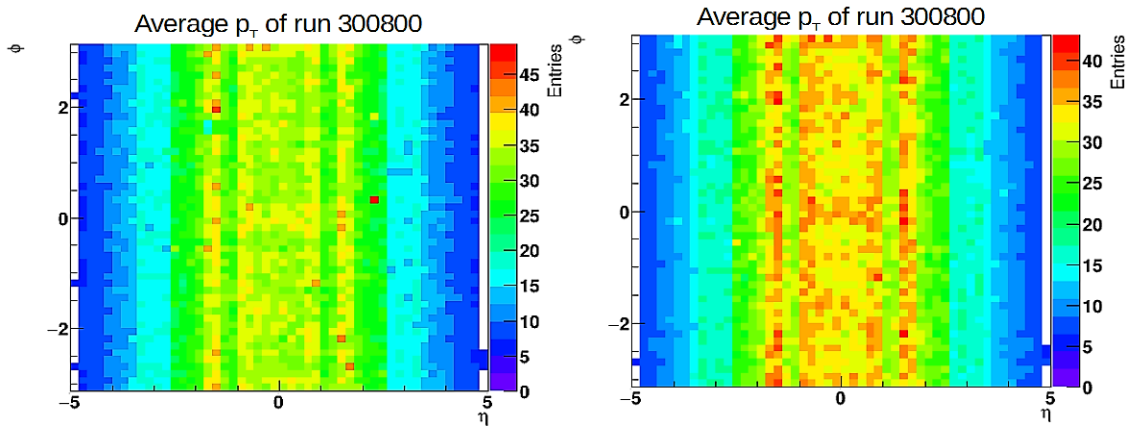


**Figure 6.5:** Occupancy plot after the express reprocessing (left) and the bulk reprocessing (right) for run 300800, events are triggered by the HLT-j25. Taken from [4].

In the DS stream the jet reconstruction is not redone and thus hot cells are not masked. Because of that, I investigated the influence of hot cells on the jet energy and coordinates further. As hot cells occur only rarely and in the 2015 TLA [18] no evidence for a hot cell induced bias within the kinematic distribution of the HLT jets was seen, no significant effected is expected. In addition, as part of the HLT jet quality selection, jets with high energy fraction in a cell with distorted pulses are removed if the energy is mainly located in an EM calorimeter layer (section 3.3). Hence, as noise distorts the pulse shape, most jets biased by a coherent hot cells are likely to be removed. As a test, I looked at the run 300800. Here, jets biased by a coherent hot cell are visible in the occupancy plots, as well as in the the $\eta$ and the $\phi$ distribution. In Figure 6.6 the $\phi$ distribution with events selected by the HLT-j110 trigger and with a leading jet with a $p_T$ of at least 150 GeV is shown without (left) and with jet quality selection applied (right). The jets biased by the hot cell are very prominent before the jet quality selection is applied, but afterward these jets are efficiently reduced.

The jet quality selection does not catch all jets biased by coherent hot cells, though. In another run, as for example run 300863, a small excess in the $\phi$ distribution remains even after the quality selection. But as a coherent hot cell mainly creates fake jets with low $p_T$, as otherwise a huge effect on the mean jet $p_T$ map would be observed, a selection regarding the jet $p_T$ should be sufficient to remove these jets. In the TLA analysis only three jets with at least 50 GeV are required in addition to the HLT jet quality criteria, the effect of coherent noise is assumed to be negligible. As sporadic but strong noise are only creating a couple of fake jets within the run they are spotted, otherwise they would be seen within the jet occupancy, the effect on $p_T$ distribution shape is also assumed to negligible.

To summarize, HLT jets are reconstructed without hot cell masking, but biased or fake jets due to coherent hot cells are mostly removed by the jet quality selection, while sporadic noises are assumed to have no significant effect on the jet energy distributions. Further studies are still in progress to decide whether in the TLA performed on data recorded in 2017 a hot cell masking should and could be included.

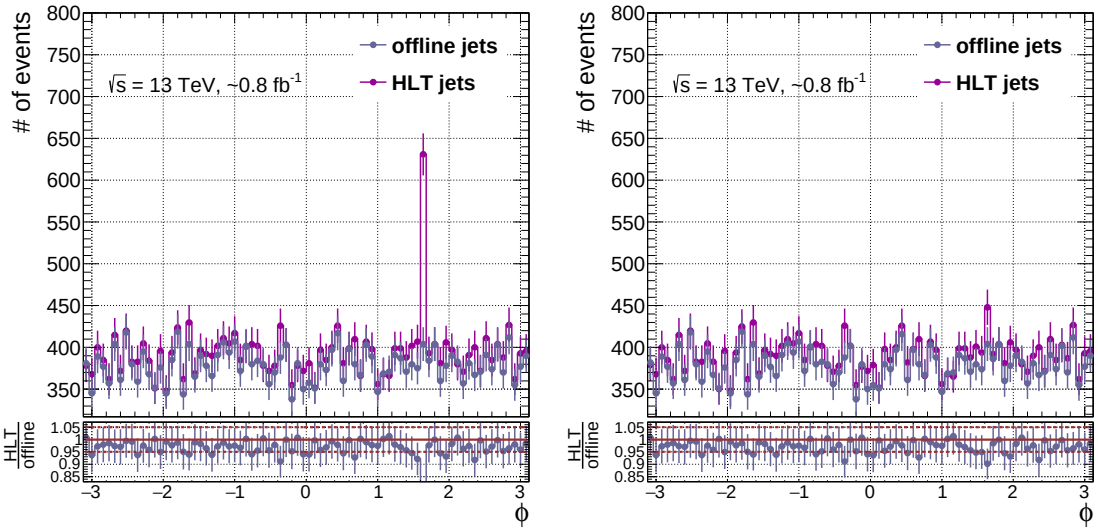


**Figure 6.6:** $\phi$ distribution of jets in run 300800 at EM scale with jet area pile-up correction. Events are selected with a HLT-j110 trigger (left) and in addition with the quality jet selection (right).

# Chapter 7

# High-Level-Trigger Jet Calibration

In ATLAS, only a fraction of the jet energy is actually measured, so calibration is required to obtain the full energy of a jet. This makes the jet energy calibration the most important task for every analysis measuring jets. The TLA is the first analysis that is using HLT jets and DS stream data. As DS stream data only contain calorimeter information, the HLT jet energy calibration is not done with the well established offline calibration scheme (section 3.2), which relies on calorimeter, tracking system and muon chamber information. Instead HLT jets are calibrated with the TLA calibration scheme - a calibration scheme specifically developed for the TLA.
In this chapter, the TLA calibration chain for HLT jets used on data recorded in 2016 and the validation of the calibration performance are presented: First, an overview of the TLA calibration in comparison to the offline calibration is given. Next, the main steps of the calibration scheme and their validation are described. In the end, a small summary is given.

## 7.1 The Trigger-Object Level Analysis Calibration Scheme

The TLA calibration scheme is a sequence of different calibration steps to correct HLT jet energies to the hadronic scale. The aim is that the energy of fully calibrated HLT jets is at the same scale as the energy of fully calibrated offline jets. Therefore, the strategy pursued in the TLA calibration is to use the same calibration strategy as in the offline calibration scheme whenever it is possible. In Figure 7.1 a comparison of the offline calibration chain (left side) and the 2016 TLA calibration scheme (right side) is given. In the following, the differences between the offline and TLA calibration chain are discussed in greater detail.

### Origin Correction

The origin correction modifies the jet coordinates to point to the physical interaction point instead of to the designed interaction point in the center of the detector. As this correction requires information about vertices reconstructed with the tracking system, it can not be applied on DS stream data. The origin correction is therefore the first difference between the TLA and the offline calibration scheme. However, the origin correction only modifies the jet coordinates and

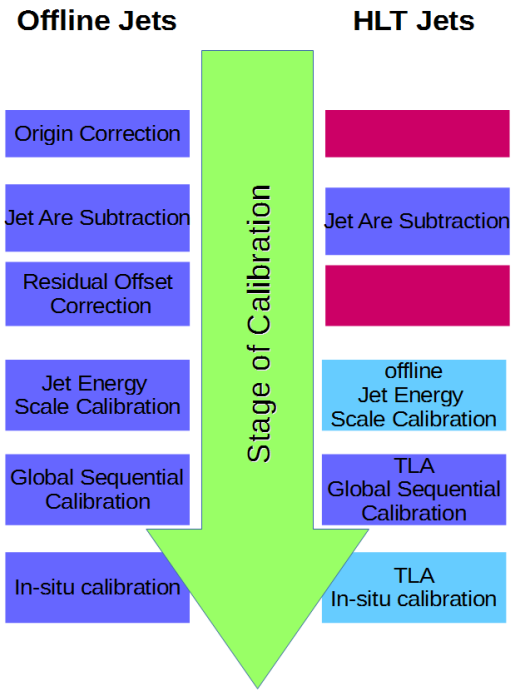


**Figure 7.1:** Offline calibration scheme compared with the 2016 TLA jet calibration scheme.

thus improves the pseudorapidity resolution, but it does not modify the jet energy. Therefore, for the purpose of the TLA, the missing origin correction has a negligible impact.

### Pile-Up Subtraction

The pile-up subtraction contains two steps: the jet area subtraction and the residual offset correction. The jet area subtraction corrects for a uniform distributed amount of pile-up events. It only requires calorimeter information and information saved in the database (e.g. $\langle\mu\rangle$) and is therefore calculable using DS stream data. The second pile-up correction, the residual offset correction, explicitly corrects for in-time and out-of-time pile-up event. It requires information about the tracking system to calculate the number of primary vertices. Therefore, only the jet area subtraction but not the residual offset correction is applied to HLT jets.
The approach of the jet area subtraction is not suitable for jets located in the forward region and therefore the energy of (HLT) jets in the forward region remain biased by energy of pile-up events. Also in the central region small contributions of pile-up jets remain (discussed previously in section 3.3). The TLA signal region does not cover the forward region, and the small bias in the central region, mostly at low transverse momentum, is corrected in the dedicated in situ calibration. Therefore, the missing residual offset correction is no issue for the TLA calibration.

### Remaining Calibration Steps

The next calibration step is the JES calibration derived with MC simulation. For data recorded in 2016, the TLA team decided to use the offline JES calibration instead of a JES calibration

dedicated to HLT jets. My studies leading to this decision are presented in section 7.2.
The following calibration step in the TLA scheme is the GSC. This correction is derived specifically for HLT jets for the first time in DS stream data recorded in 2016. The dedicated GSC is a slimmed version of the offline GSC, that only depends on calorimeter information. The method is discussed in section 7.3.
The last calibration step is the in situ calibration. In the offline calibration scheme this step consists of an offline $\eta$-intercalibration and an offline absolute in situ corrections. In the TLA scheme, the dedicated in situ calibration consists of the offline $\eta$-intercalibration, the data derived scale factors and the offline absolute in situ correction. The scale factors calibrate the energy of HLT jets with respect to the energy of offline jets and effectively account for calibration steps left out, e.g. the residual offset correction. More information is given in section 7.4.

## 7.2 Jet Energy Scale Calibration of High-Level-Trigger Jets

The JES calibration derived using MC simulation adjusts jet energies from the pile-up corrected EM scale to hadronic scale [13]. The JES calibration for HLT jets can be derived specifically as was done for the 2015 TLA [18] or the JES calibration for offline jets can be applied to HLT jets to follow the offline calibration. However, this second option is only reasonable, if the energies of HLT and offline jets calibrated to pile-up corrected EM scale are in a good agreement.
Because of the different preceeding calibration steps (Figure 7.1) and the slightly different reconstruction of HLT jets in comparison to the reconstruction of offline jets (section 6.1), the pile-up corrected EM scale describes different energy scales for HLT and offline jets. In comparison to data recorded in 2015 though, the difference between HLT and offline jet reconstruction is smaller. To determine whether the offline JES calibration can be used for HLT jets or not, I have studied various kinematic distributions and responses at EM scale. As the remaining difference at hadronic scale is around 5% in the 2015 TLA, an agreement in energy scale within 5% is considered tolerable. Due to the BCID dependent pile-up correction applied to offline as well as HLT jets in data recorded in 2016, the energy scales are in a better agreement. Therefore, in the 2016 analysis, it is possible to use the offline JES calibration instead of a dedicated JES calibration. In the following, my studies of the kinematic variables and the responses of HLT, offline and truth jets are presented.

### 7.2.1 Study of Kinematic Variables at Electromagnetic Scale

Significant differences between kinematic HLT and offline distributions (e.g. $p_T$, $\eta$ or $\phi$), indicate a mismatch between offline and HLT jets after reconstruction and pile-up subtraction. Those differences would imply that the offline jet calibration can not be used for HLT jets. Comparing the performance of kinematic variables at pile-up corrected EM scale in data and MC simulation for HLT and offline jets is therefore an important test to estimate whether the offline JES calibration can be applied to HLT jets. This study is presented here.
The study uses data representing the run period F and MC simulation (chapter 4). Events are selected with the standard offline quality selection and with the HLT-j110 trigger. The trigger is

prescaled and selects events containing a leading jet with $p_T$ of at least 110 GeV, though it is only fully efficient for leading jets with $p_T$ of at least 150 GeV. Therefore, events are required to have a leading jet $p_T > 150$ GeV.

I studied the following kinematic variables: transverse momentum ($p_T$), pseudorapidity ($\eta$) and azimuthal angle ($\phi$) of the leading jets, the subleading jets and of all jets with $p_T$ of at least 20 GeV; the angular separation ($y^*$) and the invariant mass ($m_{jj}$) between leading and subleading jets. I investigated the behavior of all these variables in slices of $\eta$ and $E$.

The results for $p_T$ and $\phi$ of all jets and the $m_{jj}$ distribution of the two leading jets are presented in Figure 7.2 - Figure 7.5. Each frame consists of four panels. The upper left panels shows the distribution for jets over all $\eta$ regions ($|\eta| < 4.5$). The upper right panel shows the distributions for jets located in the central region ($|\eta| < 1.0$). The lower left panel shows the distribution for jets in a region between forward and central, the "middle" region ($1.0 < |\eta| < 2.0$), which also covers the transition region $1.4 < |\eta| < 1.6$. The lower right panel shows the distributions for jets in the forward region ($2.0 < |\eta|$). Each of these panels consists of three plots. The top plot presents the distribution of the chosen variable for MC simulations (green - offline jets, red - HLT jets), and data (blue - offline jets, pink - HLT jets). The middle plots presents the ratio of the HLT jet distribution to the offline jet distribution (offline-to-HLT ratio) for MC simulations (green) and data (blue). The lower plot presents the double ratio, the ratio of the data ratio to the MC simulation ratio, that are shown in the middle plot.

In the figures, MC simulation and data do not correspond to the same luminosity. Therefore, differences seen in the distributions (upper plot) of MC simulation and data are without meaning for my studies, though the ratios of offline and HLT jets in MC simulations still agree to ratios in data.

The distributions are not normalized. This means that the offline-to-HLT ratio (middle plot) expresses the relative difference in numbers of jets per bin and not only the differences in shape. The difference in numbers of jets are most obvious in the $\phi$ distributions (Figure 7.2): In data, the generally flat $\phi$ distributions show a surplus of HLT jets of about 3% over the total $\eta$ range, which increases up to 5% in the central and middle region (with large contributions from the transition region). The ratio shows a surplus of offline jets about 5% in forward region. In MC simulation, the inclusive $\phi$ ratio is centered nicely around one, indicating equal numbers of HLT and offline jets. In the central and the middle region a moderate surplus of HLT jets of 2% is visible, while the forward region shows a surplus of offline jets as large as in data.

A similar offset as in the offline-to-HLT ratio can also be seen in other distributions, e.g in Figure 7.3. In addition to the offset, a peak in the ratio distribution at the lowest $p_T$ (20 - 55 GeV) bins is visible in Figure 7.3. In this bin, the ratio measured using data is 8% lower in the inclusive region (-8%, which means 8% more HLT jets than offline jets are contained in this bin), -14% in the central, -15% in the middle and +9% in the forward region. For MC simulation the values in the inclusive, the central and the middle region are less pronounced (+0.5%, - 4%, -3%), while the forward region is more pronounced (+11%). The remaining $p_T$ bins show a constant ratio well within 5% (+5% for forward region, -5% for all other regions).

This behavior of the $\phi$ and the $p_T$ distribution can be explained with the additional pile-up events, which are subtracted less effectively for HLT jets than for offline jets. In the forward region, the pile-up mainly leads to additional energy to hard scatter jets and in the central and

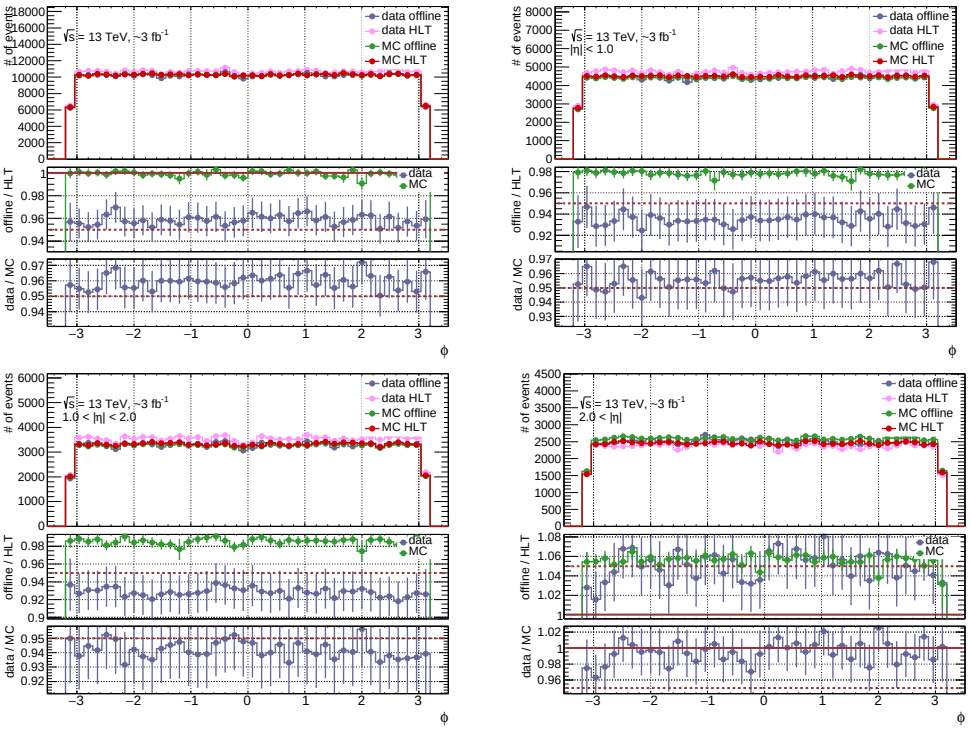


**Figure 7.2:** Inclusive offline and HLT jet $\phi$ distributions for MC simulation and data and their ratios in different $\eta$ regions at EM scale. The upper left panel shows jets inclusive over all $\eta$ regions, the upper right panel jets in region $|\eta| < 1.0$, the lower left panel jets in region $1.0 < |\eta| < 2.0$ and the lower right panel jets in region $2.0 < |\eta|$. Events are selected by HLT-j110 and a leading jet $p_T$ requirement of at least 150 GeV. In each panel, the top plot presents the jet $\phi$ distributions for MC simulations (green - offline jets, red - HLT jets), and data (blue - offline jets, pink - HLT jets). The middle plots presents the offline-to-HLT ratio for MC simulations (green) and data (blue). The lower plot presents the double ratio of the offline-to-HLT ratios shown in the middle plot.

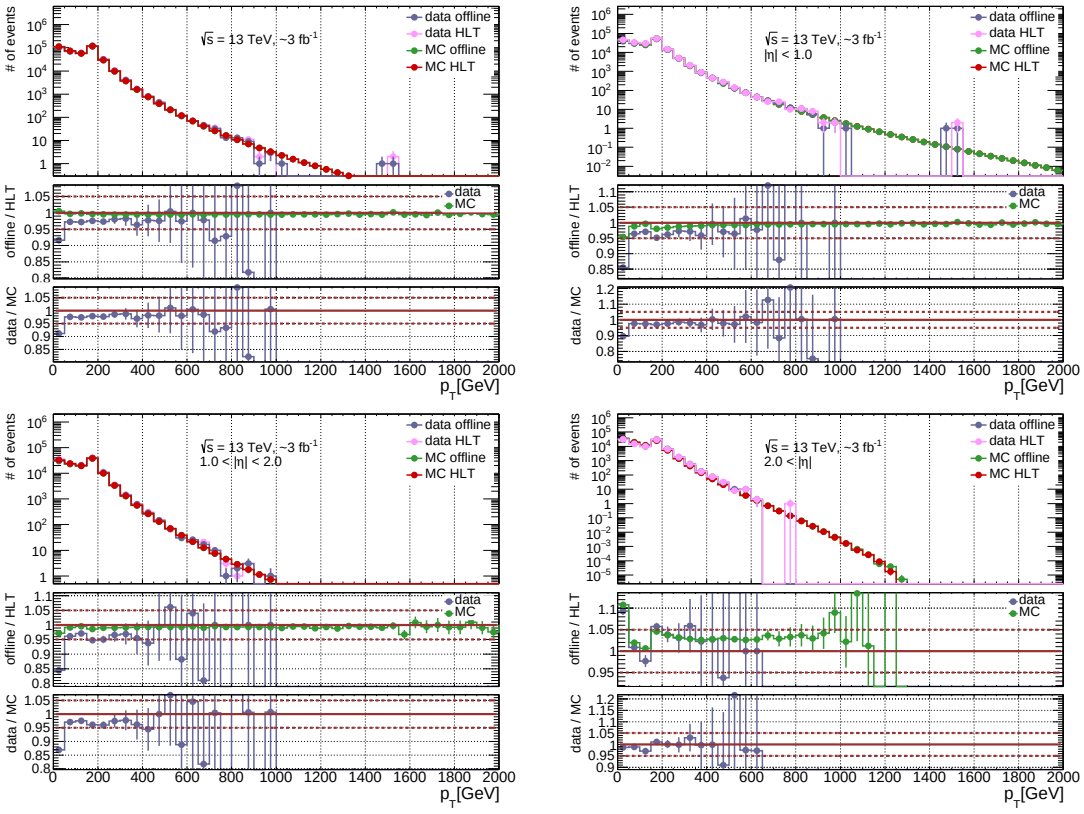


**Figure 7.3:** Inclusive offline and HLT jet $p_T$ distribution for MC simulation and data and their ratios in different $\eta$ regions at EM scale. See caption of Figure 7.2 for more details.

middle region to additional pile-up jets (section 3.2). Pile-up jets have mostly low $p_T$ and thus contributes in the lowest $p_T$ bin increasing the offline-to-HLT ratio.

At the same time more pile-up events are expected in the forward region. To counter this, the calorimeter cells bipolar pulse shape is designed to have a lager (negative) amplitude, which increases the sensitivity to out-of-time pile-up (section 2.4). This sensitivity is characterized by a negative energy contribution to the jet energies, which consequently are too low to pass the 150 GeV selection on the leading jet. In the offline calibration, this feature is corrected by the residual offset correction. In addition, less pile-up jets are generated in the forward region due high cell occupancy (subsection 3.2.4). Hence, less HLT jets than offline jets are expected in the forward regions. The residual offset correction reduces the pile-up while in all other regions more HLT jets are expected.

The MC simulation distributions show the same behavior of the ratios (middle plots), but apart from the forward region, the additional pile-up contributions for HLT jets are modeled less pronounced than seen in data. Especially in the transition region the deviation in the ratio predictions shows a 10% difference, as is shown in the inclusive $\eta$ distribution in Figure 7.4. Here, in addition to the general mis-modeling of pile-up jets in central and middle region, the poor instrumentation in the transition region contributes. In MC simulation the response of the calorimeters in the transition region is overestimated. In all $\eta$ regions, the MC simulation is reasonable within a tolerable 5% deviation. A better result at pile-up corrected EM scale is not expected.

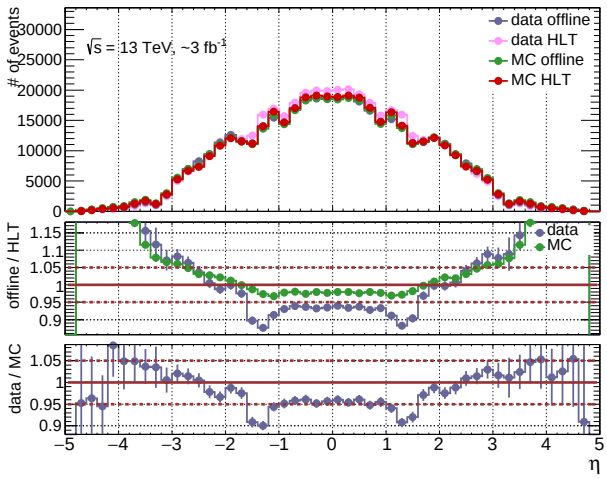


**Figure 7.4:** Inclusive offline and HLT jet $\eta$ distribution for MC simulation and data and their ratios at EM scale. The top plot presents the jet $\eta$ distributions for MC simulations (green - offline jets, red - HLT jets), and data (blue - offline jets, pink - HLT jets). The middle plots presents the offline-to-HLT ratios for MC simulations (green) and data (blue). The lower plot presents the double ratio of HLT and offline jets ratio, that are shown in the middle plot.

Outside the enriched pile-up regions (jets with low $p_T$ and jets located in the forward regions), and taking the behavior of the ratios into account, the kinematic distributions show constant ratios within 5%. The invariant mass distribution is shown as another example (Figure 7.5). Apart from masses below 200 GeV[1], the ratios are mostly constant within 5%. At masses above 1500 GeV, statistical fluctuations are distorting the ratios but the ratios still remain within the 5% range within their uncertainties.

To summarize the kinematic behavior of HLT and offline jets outside pile-up enriched regions, the Figures 7.2 tso 7.4 indicate that:

- in general, the offline-to-HLT ratio are in an agreement of 5% with each other within their uncertainties for all kinematic variables.

- for some observables the shape of the distributions differ largley between MC simulation and data (see Appendix B). The shape difference is caused partly by the mis-modeling of pile-up in MC simulation, as well as mis-modeling of detector effects in MC simulation. Still, the ratios between offline and HLT jets are comparable and also the double ratio is within 5% within their uncertainties.

- the distributions of jets with low energies (at low-$E$) or high energies (at high-$E$) are in phase space areas where the largest pile-up contribution is expected, as low-$E$ regions correspond to low-$p_T$ jets located in the central region and high-$E$ regions to more high-$p_T$ jets located in the forward region. In these regions a disagreement of up to 15% is observed. The

[1]The invariant mass depend on the four-momenta of the first two leading jets - therefore lower momenta contribution from the subleading HLT jet include pile-up contributions, which can lead to a bias in the higher mass regions up to 200 GeV.

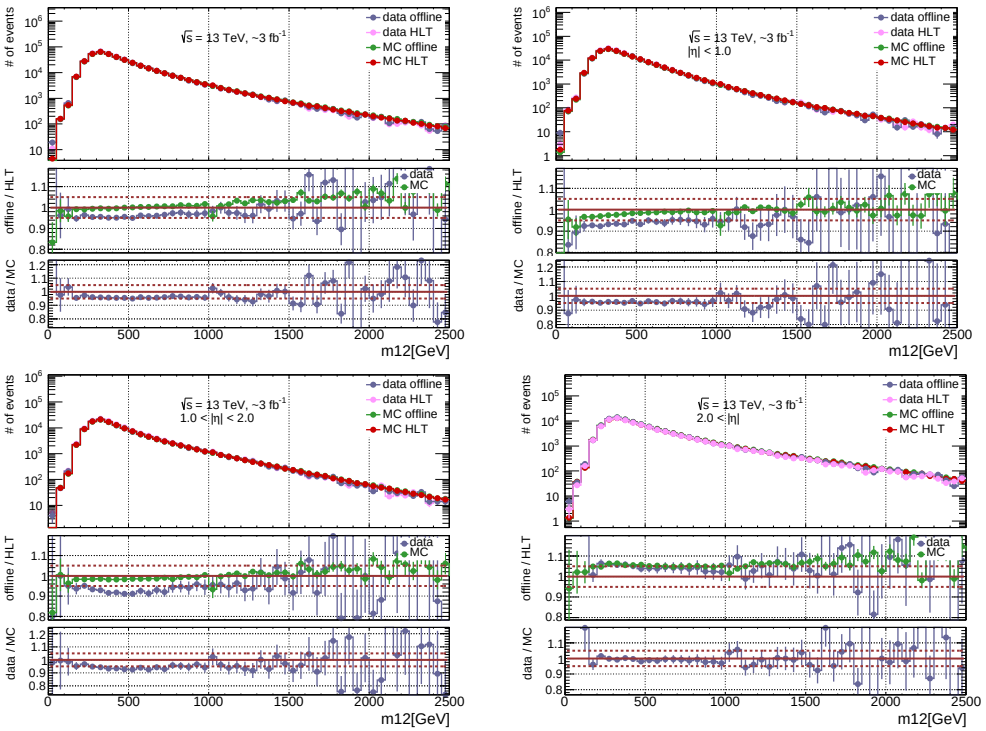


**Figure 7.5:** Inclusive offline and HLT jet $m_{jj}$ distribution for MC simulation and data and their ratios in different $\eta$ regions at EM scale. See caption of Figure 7.2 for more details.

distributions showing the $\eta$ and $E$ and $p_T$ correlation and some more kinematic distributions can be found in Appendix B.

### 7.2.2 Study of Jet Responses at the Electromagnetic Scale

The comparison of the kinematic variables shows the general agreement between offline and HLT jets. To ensure the agreement of the jet energy scales, I have studied jet momentum responses in MC simulation and data at pile-up corrected EM scale. For this study main stream data of period F is used with events selected by HLT-j110 and leading jet $p_T$ of 150 GeV and including all jets with $p_T$ >50 GeV.
I studied three different responses:

- HLT/offline response

$$R^{\mathrm{HLT/offline}}(p_T^{\mathrm{offline}}, \eta^{\mathrm{offline}}) = \frac{p_T^{\mathrm{HLT}}(p_T^{\mathrm{offline}}, \eta^{\mathrm{offline}})}{p_T^{\mathrm{offline}}(p_T^{\mathrm{offline}}, \eta^{\mathrm{offline}})} \tag{7.1}$$

- HLT/truth response

$$R^{\mathrm{HLT/truth}}(p_T^{\mathrm{truth}}, \eta^{\mathrm{truth}}) = \frac{p_T^{\mathrm{HLT}}(p_T^{\mathrm{truth}}, \eta^{\mathrm{truth}})}{p_T^{\mathrm{truth}}(p_T^{\mathrm{truth}}, \eta^{\mathrm{truth}})} \tag{7.2}$$

- offline/truth response

$$R^{\text{offline/truth}}(p_T^{\text{truth}}, \eta^{\text{truth}}) = \frac{p_T^{\text{offline}}(p_T^{\text{truth}}, \eta^{\text{truth}})}{p_T^{\text{truth}}(p_T^{\text{truth}}, \eta^{\text{truth}})} \tag{7.3}$$

In all cases, jets are matched by requiring them to be within a distance of $\Delta R = 0.4$ to each other. No isolation criteria is applied, and the jets are matched to the jets within the shortest distance. This leads to a few mismatches due to radiation processes. The mis-matches contribute as fluctuation in the tails of the response distributions, but does not influence the mean of the response and therefore not the following discussion of the results.
The HLT/offline response is the direct comparison between the energy scales of offline and HLT jets. In order to apply the offline JES calibration constants to HLT jets, this response needs to show good agreement within 5%. As the calibration constants are calculated using MC simulation only, the agreement has to be seen in data and in MC simulation.
The other two responses studied here use truth jets as reference. These responses can only be defined in the MC simulation. HLT and offline jets are taken at pile-up corrected EM scale while truth jets are by definition on truth scale. Hence, these responses are a good estimate of the responses used to calculate the JES calibration constants[2] (see section 3.2). Comparing HLT/truth and offline/truth responses provides a comparison of offline JES calibration constants to calibration constants specifically calculated with HLT jets and this provides another way to show the compatibility of HLT and offline jet energy scales.

**Deriving Response Maps**

A response map is a two dimensional histogram in $p_T$ and $\eta$ filled with the mean values of the response distribution calculated in each bin. The response distributions of matched jets are derived as described in Equation 7.1/7.2/7.3. An example for an HLT/offline response distribution in data for jets with $p_T$ between 240 GeV to 318 GeV and for $\eta$ between $-0.8$ to 0 is shown in Figure 7.6. The original response distribution (purple) is rearranged (blue) until the optimal bin size in the distribution is achieved (see Appendix C). Around the mean of the rebinned histogram a truncated Gaussian distribution is fitted. The mean of this fit result is taken as response in the respective bins and filled into the response map. More details about the fitting procedure is given in Appendix C.

The challenge for fitting a response is the definition of a good fit. While in MC simulation the response fits are well behaved because of good statistics and rather Gaussian like response distributions, there are certain issues for fitting data. Data responses are not expected to behave Gaussian like, due statistical fluctuations in the tails of the distributions and therefore neither the $\chi^2$ or the precision of the fit mean are meaningful. Especially at high $p_T$ regions, where the number of jets decreases, the fit performs worse or fails. To avoid this, I only use fit results resulting in a converted fit with a precision ($\frac{\text{mean uncertainty}}{\text{mean}}$) better than 0.8%. For my studies here, this simple approach is sufficient. For other purposes, for example to calculate calibration constants more

[2]The JES calibration is actually calculated with energy responses. Energy and transverse momentum responses only vary from each other at low $E$ or $p_T$.

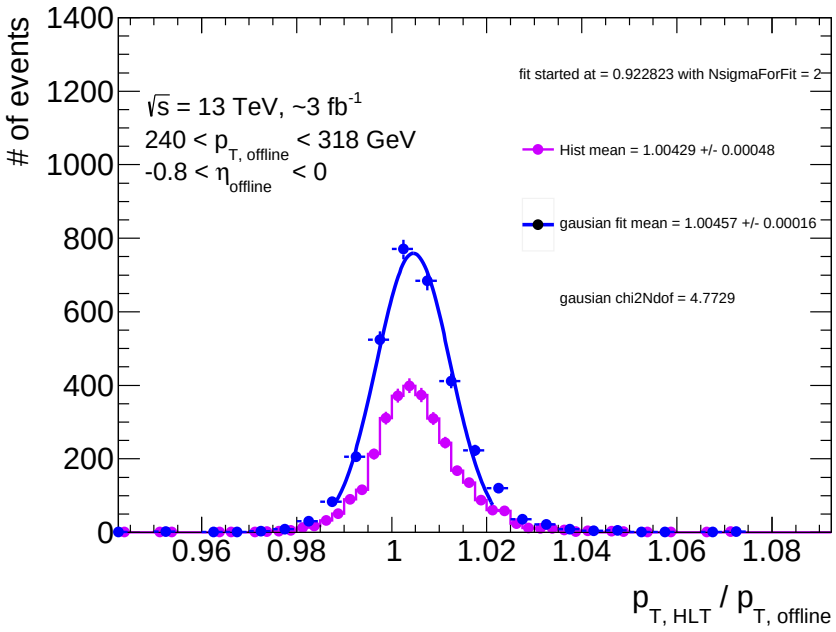


**Figure 7.6:** Response distribution of matched HLT and offline jets in data with jets with $240 < p_T < 318$GeV and within the region $-0.8 < \eta < 0.0$. The original distribution is drawn in purple, while the rearranged distribution and the fit result are shown in blue. HLT and offline jets are at pile-up corrected EM scale and are matched within $\Delta R < 0.4$. All events passed the `HLT_j110` trigger and a leading jet $p_T$ selection of 150 GeV.

sophisticated approaches are needed. So far, no universal definition of a good response fit is found.

### Response Maps at Pile-Up Corrected Electromagnetic Scale

The data HLT/offline response map is presented in Figure 7.7. The white areas at high $p_T$ mark the areas where either the number of events in data is insufficient for fitting or the fit does not meet the requirements explained before. The response map includes mean responses for jets with transverse momenta within 55 GeV to 780 GeV, located in the range $-2.8 < \eta < 2.8$. The most pile-up enriched regions, as described before, are therefore not included.
The pile-up corrected EM scale of offline and HLT jets are within a 3% agreement. The most problematic $\eta$ region is the transition region ($1.4 < |\eta| < 1.6$) for jets with $p_T < 100$ GeV. This region is sensitive to out-of-time pile-up. To compensate the increased amount of inactive material in the transition region, higher calibration amplitudes for the bipolar pulse shape in the calorimeter cells are used, so the positive energy contributions are not compensated in the first bunch crossings in the bunch train. The BCID dependent pile-up correction is less effective here, as the correction is calculated for total barrel region. Hence, without the residual offset correction some differences remain and the HLT jet response is overestimated.
The response for jets in the range $|\eta| > 2.0$ is underestimated. In this range the sensitive region to out-of-time pile-up starts due to the reduced granularity and higher cell occupancy (which is the same argument as for why less HLT jets are included in the forward region). The HLT response

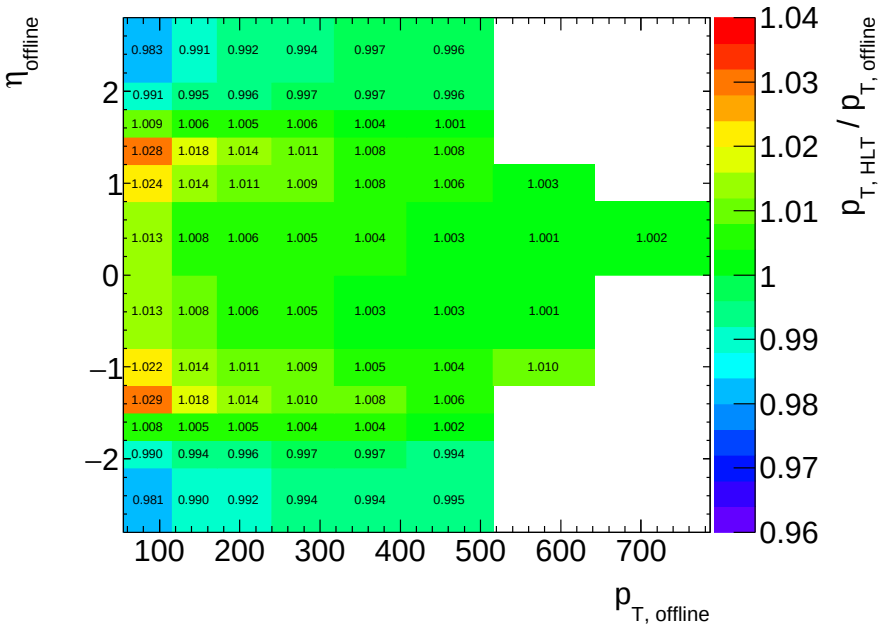


**Figure 7.7:** Transverse momentum response map of HLT jets and offline jets in data at pile-up corrected EM scale. They are matched with a $\Delta R < 0.4$. All events passed the HLT-j110 and a leading jet $p_T$ selection of 150 GeV.

for jets with $p_T < 100$ GeV is underestimated by 2% in this range. In general, with increased transverse momentum the agreement of the HLT and offline jet energy scales improves.
The response plots using MC simulation are shown in Figure 7.8 and Figure 7.9 for HLT/offline, HLT/truth and offline/truth. The HLT/offline responses show an agreement of 0.5%, apart from jets with $p_T < 100$ GeV, where the agreement is within 2%. The agreement in the range $|\eta| < 2.0$ shows the mis-modeling of pile-up events in the MC simulation, as a worse agreement is seen in data responses. The truth response maps show values ranging from 0.55 to 0.8, showing the non-compensating nature and inactive material in the detector, but agree with each other within 2%.

To summarize, the comparison of HLT and offline jet energies at pile-up corrected EM scale is showing a reasonable agreement. In data, HLT jets have a 3% difference in transverse momentum from offline jets in pile-up sensitive regions (transition range and range $|\eta| > 2.0$ at low-$p_T$). This difference is tolerable and will be corrected by the data derived scale factors, calculated at a later calibration step. In MC simulation, HLT jets have only a 2% derivation to offline jets. The truth response maps show that the JES calibration constants calculated with HLT jets would differ only by 2% from the offline JES calibration constants. The uncertainty of the JES calibration constants is around 2% [13] and hence this difference is negligible.
The study of the response maps at pile-up corrected EM scale supports the results of the study of the kinematic variables: Offline and HLT jets behave similarly and their energy scales are in a reasonable agreement. An HLT-dependent JES calibration is not necessary, thus the offline JES calibration derived with MC simulation is used for HLT jets.

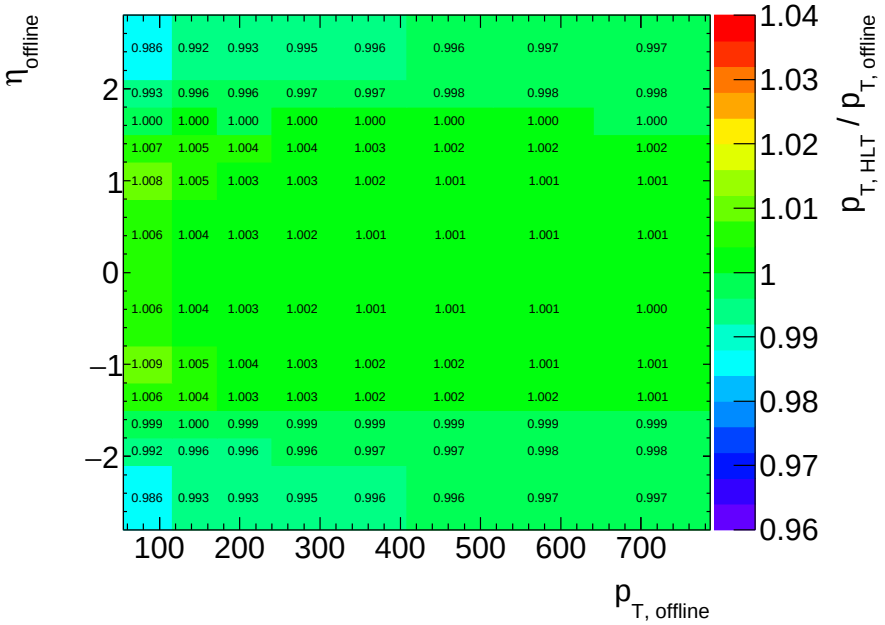


**Figure 7.8:** Transverse momentum response as a function of $\eta$ and $p_T$ of HLT jets and offline jets in MC simulation at EM scale. HLT jets are corrected for pile-up effects and offline jets for pile-up effects and origin. They are matched with $\Delta R < 0.4$. All events passed the HLT-j110 and a leading jet $p_T$ selection of 150 GeV.

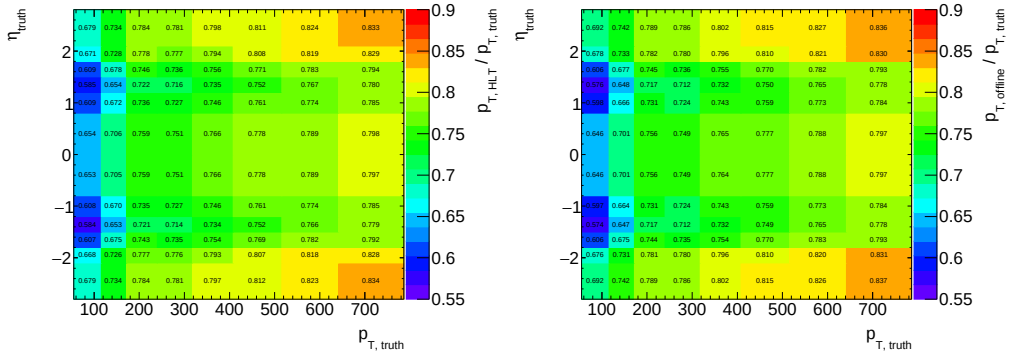


**Figure 7.9:** Transverse momentum response as a function of $\eta$ and $p_T$ of HLT jets and truth jets from MC simulation (left) and offline jets and truth jets (right) at EM scale. HLT jets are corrected for pile-up effects and offline jets for pile-up effects and origin. They are matched with $\Delta R < 0.4$ to truth jets. All events passed the HLT-j110 and a leading jet $p_T$ selection of 150 GeV.

### 7.2.3 Study of Response Maps at Jet Energy Scale

To validate that the offline JES calibration is applicable to HLT jets, the response maps for jets at EM+JE scale (jet energy after applying the offline JES calibration to jet energies at pile-up corrected EM scale) using data and MC simulation are derived. For this the offline JES calibration from the central ATLAS recommendations is applied to the HLT and offline jets. Events are selected by HLT-j110 and a leading jet with $p_T > 150$ GeV is requested.

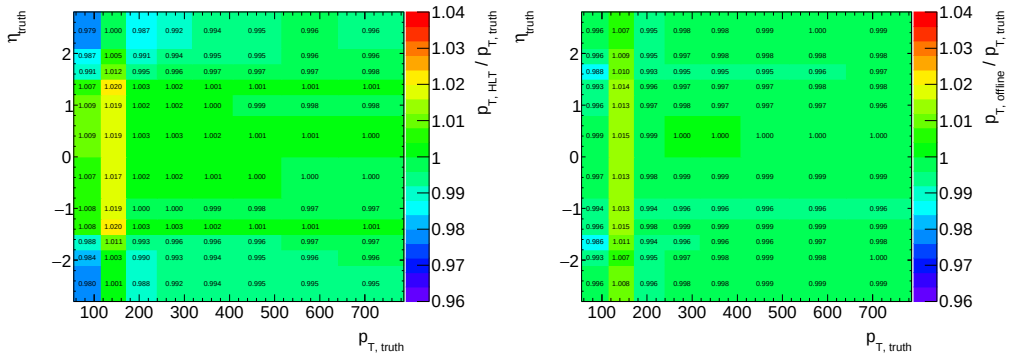


**Figure 7.10:** Transverse momentum response of HLT jets and truth jets in MC simulation (left) and offline jets and truth jets (right), after applying the JES calibration derived from offline jets to offline and HLT jets. They are matched with a $\Delta R < 0.4$ to truth jets. All events passed the HLT-j110 and a leading jet $p_T$ selection of 150 GeV.

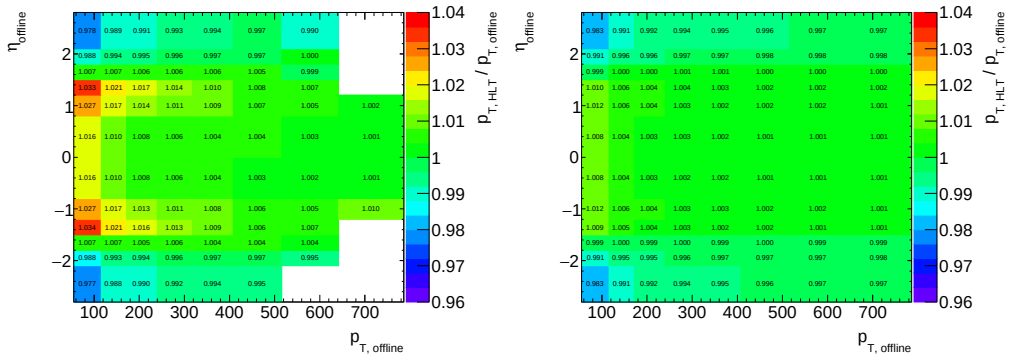


**Figure 7.11:** Transverse momentum response as a function of $\eta$ and $p_T$ of HLT jets and offline jets in data (left) and in MC simulation (right), after applying the JES calibration derived from offline jets to offline and HLT jets. Jets are matched with $\Delta R < 0.4$. All events passed the HLT-j110 and a leading jet $p_T$ selection of 150 GeV.

With the offline JES calibration applied, jets are calibrated to truth scale (EM+JE scale in data) and especially the offline/truth response map is designed to show a uniform distribution. But as the calibration corrections are derived using a different MC simulation sample containing different selection criteria, no perfect agreement is expected.
In Figure 7.10 the HLT/truth and offline/truth response are presented. The offline/truth response map at EM+JE scale shows an agreement of 0.5% but only above $p_T > 180$ GeV. Below 180 GeV a worse agreement of 1.5% is observed. A similar behavior is seen for the HLT/truth response.

Above 180 GeV an agreement within roughly 1% is observed as is expected due to the difference between offline and HLT jet energy scale at pile-up corrected EM scale. Also the underestimation in the range $|\eta| > 2.0$ is expected. Below 180 GeV the difference worsens to 2%.
The deviations below 180 GeV are most likely caused by flavor fluctuations. The events used for the computation of the responses have leading jets with a $p_T$ of at least 150 GeV, but the JES calibration constants applied are derived in MC simulation without this specific selection. As this selection on a steeply failing leading jet $p_T$ distribution, changes the number of quark- and gluon-initiated jets, which are differently measured within the detector, the average response of offline and HLT jets is biased by this selection applied (subsection 3.2.6). Hence, the JES calibration constants over-correct the $p_T$ of HLT and offline jets that have a leading jet $p_T$ selection applied. This results in an overestimation of the response with respect to truth jets around 1.5% for offline jets and 2% for HLT jets. This effect is later covered by the GSC (see section 7.3).
All in all, the offline/truth and HLT/truth response maps show an agreement within the uncertainties of the calibration constants and confirm that no bias is induced by applying the offline JES calibration to HLT jets.
The HLT/offline response maps are presented in Figure 7.11 with the data response map on the left side and the MC simulation response map on the right side. The energy scale between HLT and offline jets is supposed to be unchanged in comparison to the response maps at pile-up corrected EM scale as the same constants are applied to both jets. The deviations between HLT and offline jets is most pronounced at low-$p_T$ though, especially in the transition region ($1.4 < |\eta| < 1.6$). The offline JES calibration constants are therefore over-correcting the HLT jet $p_T$ in the $|\eta| < 2.0$ range and under-correct the HLT jet $p_T$ in the region $|\eta| > 2.0$. The deviations are enhanced by applying the offline JES calibration.
In data, the HLT/offline jet response at EM+JE scale is worsened with respect to the HLT/offline response at pile-up corrected EM scale around 1% in the transition region and around 0.5% elsewhere. In MC simulation, the jet response is worsened around 0.5% over the total $\eta$ region, because of the better agreement of HLT and offline jet energy at pile-up corrected EM scale over the total $\eta$ range. In total, the EM+JE scale of HLT and offline jet energies agree within 4% in data, and within 2% in MC simulation.
The results presented here shown that the offline JES calibration is applicable to HLT jets. This approach does not introduce a systematic bias, nor does it enhanced the disagreement between HLT and offline jet energy scale unreasonably. The differences between HLT and offline jet energy scale is tolerable and is corrected for in the dedicated in situ calibration step.

## 7.3 Dedicated Global Sequential Calibration

The next calibration step for both offline and HLT jets is the GSC. This correction is derived using MC simulation and uses several global jet variables to improve the jet energy resolution and reduce the jet energy dependence on the flavor of the jet initiating parton. Without the GSC the unknown flavor composition in a data sample has to be taken as uncertainty on the final jet energy. In the offline calibration, the global jet variables require calorimeter but also tracking system and muon chamber information (section 3.2). As the DS stream contains only calorimeter information, a dedicated GSC derived using calorimeter information only is created to improve

the HLT jet energy resolution and to reduce the flavor uncertainty. The flavor uncertainty is the dominant uncertainty in the 2015 TLA (chapter 5). The following calorimeter based variables are used to calculate the dedicated GSC:

1. $f_{Tile0}$, the fraction of jet energy deposited in the first tile layer
2. $f_{EM3}$, the fraction of jet energy deposited in the third EM calorimeter layer
3. $N_{90Constituents}$, the number of constituents carrying 90% of the jet energy

The first two variables are well established GSC variables (section 3.2), whereas $N_{90Constituents}$ is a variable specially employed in the TLA calibration.
The number of constituents carrying 90% of the jet energy is a replacement for the number of tracks associated to a jet, $n_{\text{trk}}$, which is used in the offline GSC. The number of constituents depends on the width of a jet and has therefore the potential to reduce the sensitivity of the calorimeter response to the jet shape and hence the flavor of the initiating parton.
The calorimeter based GSC is calculated using the same procedure as for the offline GSC: The HLT jets are matched to truth jets within $\Delta R < 0.3$ and an isolation requirement is applied before the corrections are calculated in sequences for bins in $p_T$, $\eta$ and the respective global variable. The dedicated GSC improves the resolution similar to the offline GSC and an illustration of the resolution improvements can be seen in the offline resolution Figure 7.13[3]. The dedicated GSC improves the resolution around 20% for jets within 20 GeV $< p_T <$ 250 GeV.
I validated the GSC with respect to the HLT jet energy scale by studying the response maps of data and MC simulation for HLT, offline and truth jets with HLT and offline jets at EM+JE+GSC scale (after correcting for pile-up, applying the offline JES calibration constants and the respective GSC). As the GSC is not derived to correct the jet energy but the jet energy resolution, any lager change in the jet responses with respect to jet responses at EM+JE scale are indicating a mis-calibration.
The MC simulation responses are created without any selections applied on the leading jets $p_T$ to be able to see purely calibration induced effects. For data responses, the main stream data of period F are selected with the HLT-j110 trigger and a leading jet $p_T$ requirement of at least 150 GeV.
In Figure 7.12 the response maps of HLT/truth (left) and offline/truth (right) are presented. The offline/truth response shows an agreement within 1% over the full $\eta$ range. The HLT/truth response shows an agreement within 1% in the range $|\eta| < 1.8$ and within 3.5% in the range $1.8 < |\eta| < 2.8$. The underestimation of the HLT jet $p_T$ in the more pile-up sensible region is enhanced by 0.5%. Why the agreement gets worse in the higher $\eta$ range is not yet fully understood, investigations are still ongoing. However, as the results in the central region are unchanged with respect to the results at EM+JE scale, no systematic bias is expected by applying the dedicated GSC.
The HLT/offline responses in MC simulation and data are shown in Figure 7.13. The MC simulation response (right) shows an agreement between HLT and offline jet energy within 1% in the range $|\eta| < 1.8$ and within 3% in the range $1.8 < |\eta| < 2.8$. In data, the general agreement is around 4%, especially in the out-of-time pile-up sensible regions (at low-$p_T$ and in the range

[3]Due to ATLAS privacy rules, the resolution plot for the dedicated GSC can nor be shown.

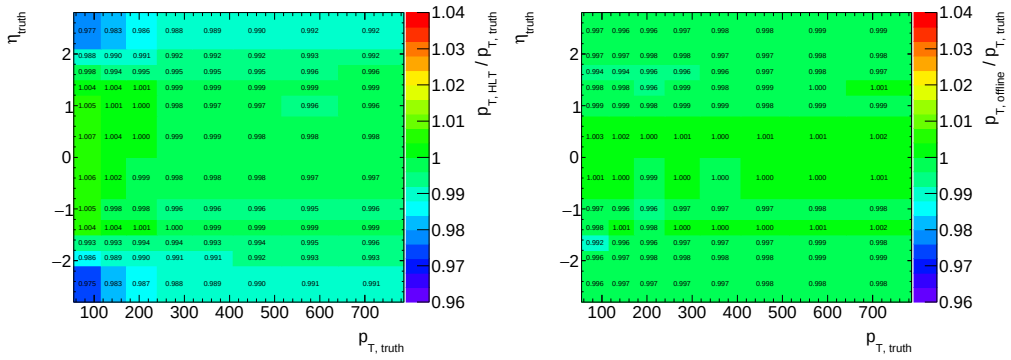


**Figure 7.12:** Transverse momentum response as function of $\eta$ and $p_T$ of HLT and truth jets (left) and offline and truth jets (right) at EM+JE+GSC scale. Jets are matched with a $\Delta R < 0.4$.

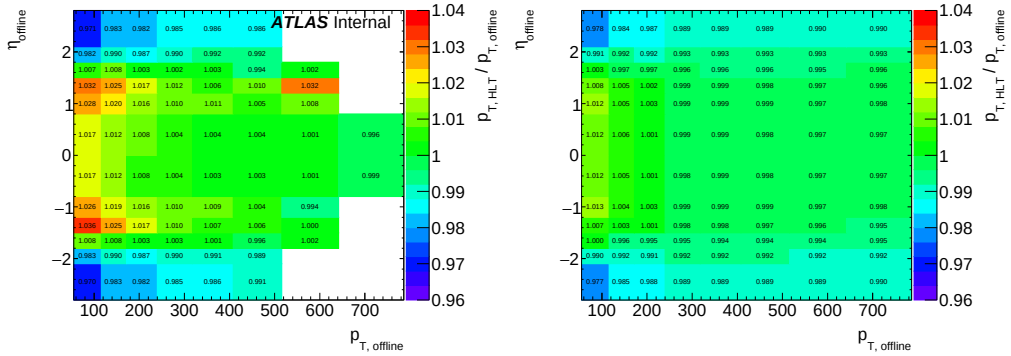


**Figure 7.13:** Transverse momentum response as function of $\eta$ and $p_T$ of HLT and offline jets at EM+JE+GSC scale in data (left) and in MC simulation (right). Jets are matched with $\Delta R < 0.4$. Events in data are selected by HLT-j110 trigger and require a leading jet with $p_T > 150$ GeV.

$1.4 < |\eta| < 1.6$), as it was in the EM+JE scale response map. In the range $1.8 < |\eta| < 2.8$ for $p_T > 150$ GeV the agreement is 1% worse than at EM+JES. This is the same effect already seen in the truth responses and not yet understood.

To summarize, the total agreement of the HLT and offline jet energies at EM+JE+GSC scale is as good as at EM+JE scale. Only in the range $1.8 < |\eta| < 2.8$ the agreement is worsen in comparison to the preceeding calibration step results. This effect is still tolerable though, and will be accounted for by the following in situ calibrations. As the HLT jet resolution is improved by 20%, the flavor uncertainty is reduced and the total agreement between HLT and offline jets is unchanged, the dedicated calorimeter based GSC is applied to HLT jets.

## 7.4 Dedicated In Situ Calibration

The in situ calibration steps derive correction factors using data. The calibrations are the $\eta$-intercalibration, the data derived scale factors and the absolute in situ calibration.

### 7.4.1 $\eta$-Intercalibration of HLT Jets

In the $\eta$-intercalibration, detector issues not modeled in MC simulations are accounted for by calibrating jets located in the range $|\eta| > 0.8$ with well calibrated jets in the central $\eta$ range. The procedure is described in section 3.2.

In principle, the $\eta$-intercalibration correction can be derived for HLT jets in the same way as for offline jets. However, the pile-up suppression is less efficient for HLT jets and as the $\eta$-intercalibration is sensitive to third jet radiation and to pile-up jets, a dedicated $\eta$-intercalibration is too unstable. Therefore, the offline $\eta$-intercalibration is applied to HLT jets, if the correction constants are within the statistical and systematical uncertainties to the dedicated correction constants. In data recorded in 2016, this requirement is fulfilled and the offline $\eta$-intercalibration is applied to HLT jets.

To validate that the offline $\eta$-intercalibration can be applied to HLT jets, I looked at the HLT/offline response in data at "intercalibration" scale (offline and HLT jet energies after applying the $\eta$-intercalibration[4] on top to the preceeding calibrations in the respective calibration schemes). The response is shown in Figure 7.14. Data representing the period F are used with events selected by HLT-j110 and a leading jet $p_T$ with at least 85 GeV.

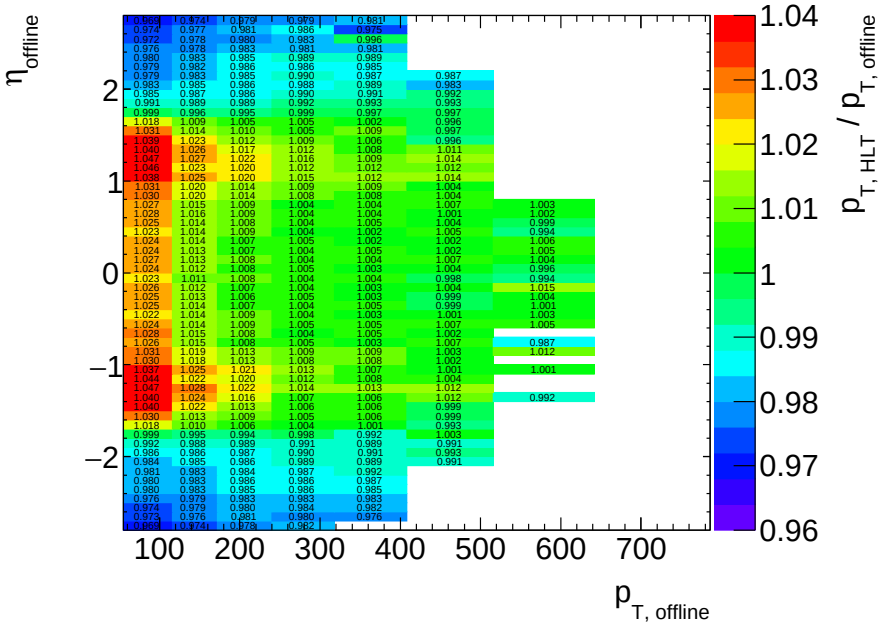


**Figure 7.14:** Transverse momentum response of HLT and offline jets in data at intercalibration scale. They are matched within $\Delta R < 0.4$. All events passed the HLT-j110 and have a leading jet with $p_T > 85$ GeV.

The trigger requirement, the leading jet $p_T$ selection and the $\eta$ binning are changed in the HLT/offline response map, because the jet momentum responses at intercalibration scale are used for the calculation of the data derived scale factor calculation. Therefore, the response map is

[4]The $\eta$-intercalibration applied here is a preliminary version. My results presented are mostly invariant to changes in the $\eta$-intercalibration as I am comparing offline to HLT jets with the same $\eta$-intercalibration applied.

not directly comparable to response maps at EM+JE+GSC scale. Still, no new differences are spotted. The general agreement between HLT and offline jet energies at the intercalibration scale is within 4%, with largest discrepancies at low-$p_T$ in the transition range ($1.4 < |\eta| < 1.6$) and the range $2.0 < |\eta|$. The offline $\eta$-intercalibration is applicable to HLT jets.

### 7.4.2 Data Derived Scale Factors

Scale factors are derived from main stream data to calibrate the HLT jet energy to offline jet energy. The scale factors are derived at intercalibration scale, and by aligning the HLT jet energy to offline energy scale. All missing steps in the TLA calibration scheme and the later enhancements by offline calibrations applied to HLT jets as well as the small differences in the jet energy reconstruction are accounted for in this step. Scale factors are only applied to data, because in MC simulation HLT/offline responses are in a good agreement within 2%, which is covered by the uncertainties of the JES calibration.
The response map after applying the $\eta$ intercalibration in Figure 7.14 is a good estimate of the inverted scale factors[5]. In fact, the scale factor calculation starts with the same response distributions. The responses are fitted using a truncated Gauss distribution to get the (Gaussian) mean of the response distribution, before the scale factors are derived via a numerical inversion plus smearing.
The fitting procedure is similar to the one I am using to calculate the response maps, but it includes an additional quality criteria and an algorithm, which describes what to do with bad quality fits. As the fit is smoothed afterward, these regulations are necessary. The additional criteria and the regulation are described here:

- Only response distributions with at least 25 events are fitted, otherwise the response value is set to one.
- If the fit has a Gaussian mean uncertainty greater than 0.8%, the fit result is replaced by the fit result of the next lower $p_T$ bin.
- In $p_T$ bins higher than 1200 GeV the fit result is replaced by the fit result of the next lower $p_T$ bin.
- In $p_T$ bins lower than 70 GeV the fit result is replaced by the fit result of the next higher $p_T$ bin.

To increase the number of events for the scale factors, more than one jet trigger are selecting the events. If the $p_T$ range is above the 99% efficiency point of a jet trigger, a higher trigger with less prescale is used to select the events (e.g. at 100 GeV the HLT-j60 trigger with a 99% efficiency point of 85 GeV is used, but for bins with e.g. 200 GeV the HLT-j110 trigger with a 99% efficiency point of 150 GeV is used.)
The response histograms are binned in offline jet $p_T$ and $\eta$. In order to calibrate the HLT jets, their energy is multiply with the scale factors $\frac{1}{R^{\mathrm{HLT/offline}}}$. The scale factors are applied as a function,

[5]Due to ATLAS privacy rules, the final scale factor plot can not be shown.

which depends on the HLT jet $p_T$:

$$p_T^{\text{offline}} = \frac{1}{R^{\text{HLT/offline}}(p_T^{\text{offline}}, \eta^{\text{offline}})} \cdot p_T^{\text{HLT}} \tag{7.4}$$

$R^{\text{HLT/offline}}(p_T^{\text{offline}}, \eta^{\text{offline}})$ is the HLT/offline response, calculated as described above. As Figure 7.14 shows, the response values are rather small with a small slope in positive $p_T$ direction. Therefore with a fine $\eta$ binning, a linear function as in Equation 7.4 is sufficient to calculate smoothed scale factors. The scale factors are smoothed to not introduce binning dependency within the calibration.

The calculated scale factors are applied to the HLT jets such that the energies of HLT jets are at the offline intercalibration scale, or simply, HLT jet energies are at the same scale as the offline jet energies used to calculate the scale factors: the hadronic scale[6].

In Figure 7.15, the HLT/offline response map at the hadronic scale is shown. The response map is derived with data of period F and events selected with HLT-j110 and a leading jet $p_T$ with at least 85 GeV. The agreement of the HLT and offline jet energies within the TLA $\eta$ range ($|\eta| < 2.8$) is within 1.0% apart from the transition range in the lowest $p_T$ bin. In this range, the agreement worsen to 1.5%, though this is an effect introduced by using jets below 70 GeV for the response map. The scale factors are not calculated explicitly for jets below 70 GeV and the lowest $p_T$ bin in the response map covers the region $50 < p_T < 110\,\text{GeV}$. Instead, the scale factor of the next higher bin is taken. This $p_T$ bin is therefore overestimated, which is only visible in the transition region, where the highest deviations in the agreement were seen over all scales. These bins in the low $p_T$ transition region are not further referred to.

The HLT/offline jet response maps at hadronic scale shows an agreement of 1.0%, which is covered by the uncertainty on the jet energy. All pile-up sensitive ranges, which were visible by an enhanced disagreement in HLT and offline jet energies, are corrected for by this calibration step. The scale factors are behaving as expected.

### 7.4.3 Absolute In Situ Validation of High-Level-Trigger Jets

The offline in situ calibration (see section 3.2) is the final calibration step in the offline and TLA calibration chain and used for validation of the hadronic scale of the HLT jet energies. Hence, the offline in situ calibration is a validation for the TLA calibration scheme. Only the $\gamma$ - jet balance technique is used for the final calibration.

After employing the scale factors to HLT jets, they are on the same scale as offline jets. Hence, the $\gamma$-jet balance derived using offline jets can also be applied to HLT jets. If the scale factor derivation and all previous calibration steps in the TLA calibration scheme worked as discussed, the HLT/offline response at in situ corrected hadronic scale is supposed to show the same agreement as before at hadronic scale.

While the final validation of the energy scale of HLT jets for the TLA will be done with the invariant mass response of the two leading jets, for my purpose the response of the momenta is sufficient. In Figure 7.16 the HLT/offline jet energy response at in situ corrected hadronic scale is

[6] In principle, HLT and offline jet energies are at the hadronic scale after applying the offline JES calibration. But as the additional calibrations improve the jet energies further, I chose to call the scale only now hadronic scale.

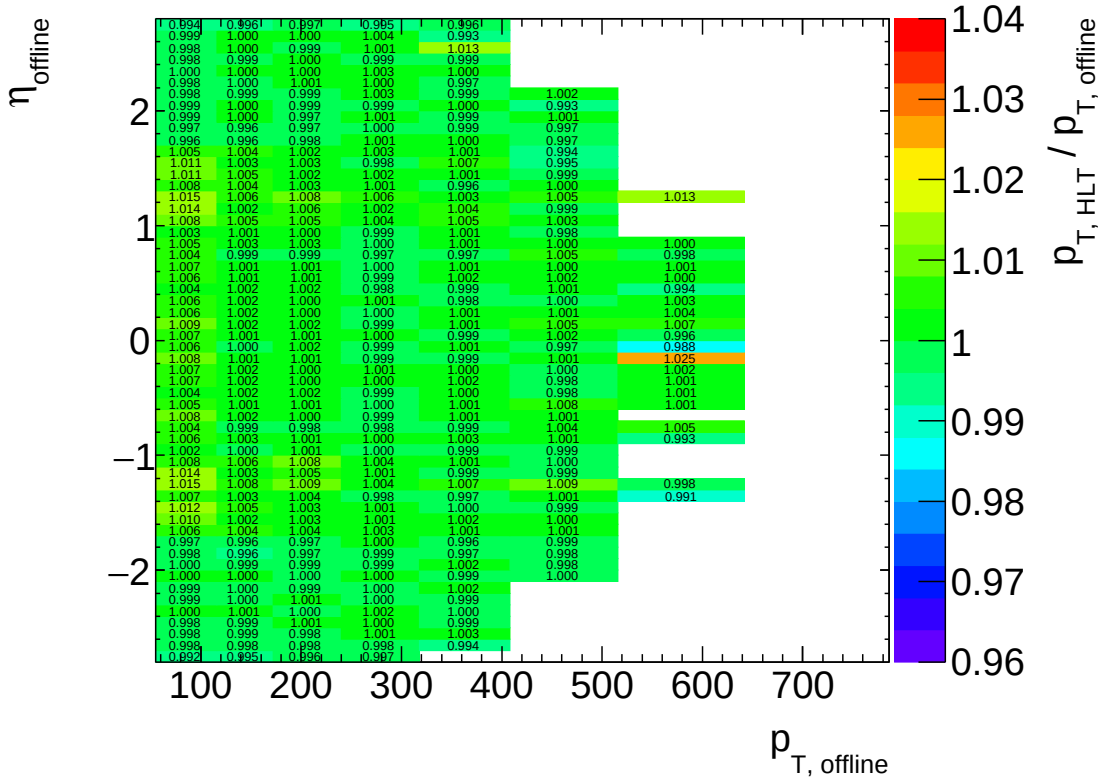


**Figure 7.15:** Transverse momentum response as a function of $\eta$ and $p_T$ of HLT jets and offline jets in data at hadronic scale. They are matched with $\Delta R < 0.4$. All events passed the HLT-j110 and a leading jet $p_T$ of at least 85 GeV.

shown. For this plot the data recorded in period F is used with events selected by HLT-j110 and leading jet $p_T$ requirement of at least 85 GeV. The agreement of HLT and offline jet energies is the same as the agreement at hadronic scale: within 1%.

With this last correction step applied, the HLT jet energies are fully calibrated to the in situ corrected hadronic scale. The HLT jet energies are validated by the comparison to the offline jet energies at in situ corrected hadronic scale, which shows that the energy scales agree with each other within 1%, which is within the HLT jet energy uncertainty. This means the TLA calibration scheme is validated. For the HLT jet energy uncertainty, the offline jet energy uncertainty is used, though in addition a conservative uncertainty corresponding to the values of the scale factors for non-closure and an additional pile-up uncertainty is taken into account (as described in chapter 5). Due to the dedicated GSC, no additional flavor uncertainty is taken into account and hence, the HLT jet energy uncertainty is comparable to the offline jet energy uncertainty. The jet energy resolutions are also comparable, also as consequence to the dedicated GSC. To summarize, my studies showed that HLT jets are well calibrated objects and usable for the TLA.

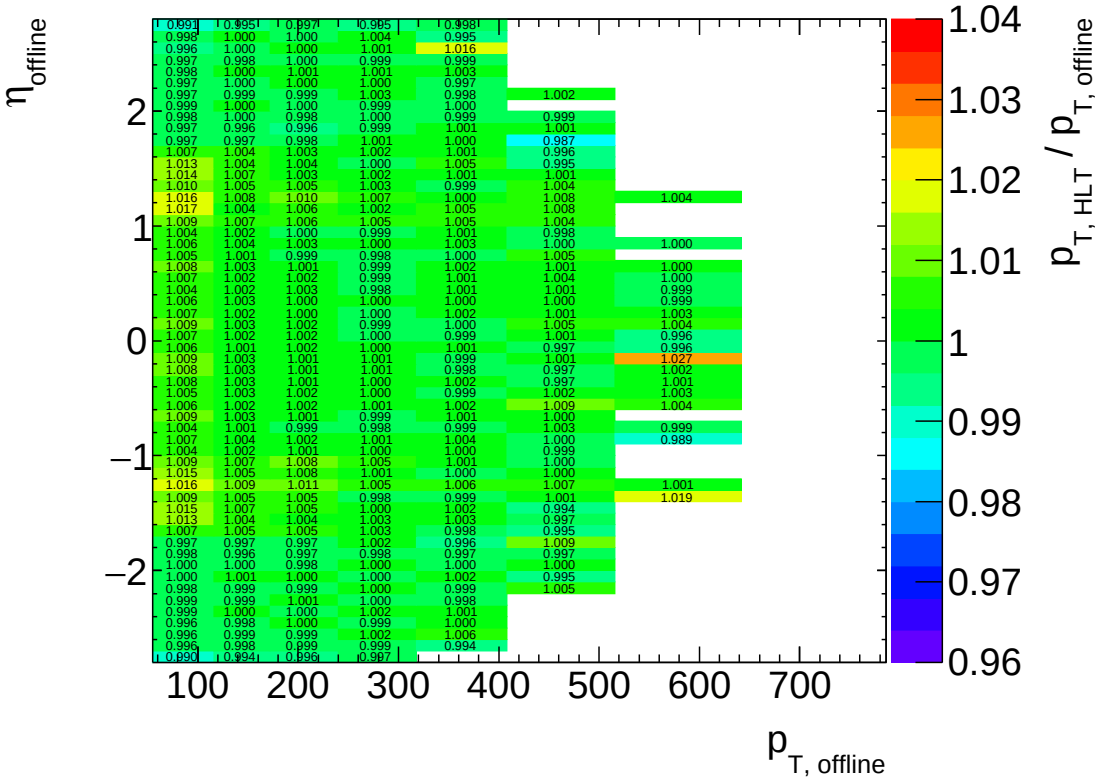


**Figure 7.16:** Transverse momentum response as function of $\eta$ and $p_T$ of HLT jets and offline jets in data at in situ corrected hadronic scale. They are matched within $\Delta R < 0.4$. All events passed the HLT-j110 and a leading jet $p_T$ selection of 85 GeV.

# Chapter 8

# Conclusion

In this thesis, I provided an overview of the standard jet reconstruction and calibration used in ATLAS, and compared them to the reconstruction and calibration used in the TLA. As the TLA relies only on calorimeter information, the calibration of the HLT jets does not include all the corrections that are applied in the standard offline calibration. To be able to account for the missing steps and validate the performance of the calibration scheme, HLT jets are calibrated to offline jet energy scale.

I showed that the deviations between HLT and offline jet energies are due to the missing residual pile-up correction. Furthermore, I showed that the deviations within the TLA signal regions are small and the average correction in $p_T$ and $\eta$ bins towards the offline jet energy is sufficient to correct for them without increasing the uncertainties much: The data derived scale factors are within 4% only. After applying the scale factors to HLT jets, the HLT jet energy is within 1% of the offline jet energy with comparable resolution and uncertainties. Even further, the offline derived in situ corrections applied to HLT jets proofed the stability of the calibration principle. With this, the performance of the TLA calibration scheme is validated, and HLT jets are usable in the TLA.

For the data-taking in 2017/2018, the ATLAS collaboration plans to employ a new technology, the "fast trackers". This technology would allow the reconstruction of tracks in HLT during data-taking, which would have a tremendous effect on the HLT jet energy scale. The residual-offset corrections could be applied to HLT jets. This would improve the agreement between HLT and offline jet energies, especially in the pile-up sensitive $\eta$ regions ($1.4 < |\eta| < 1.6$ and $2.0 < |\eta|$). Consequently, the scale factors would be reduced and therefore the HLT jet energy uncertainty would improve. Other studies might arise, using HLT jets for precision searches at low dijet-masses.

# Bibliography


[1] A. Valero and J. Abdallah and V. Castillio and others. Readiness of the ATLAS Tile Calorimeter for LHC collisions, February 2008.

[2] R. Lince Amaral Farto Abreu, A. Ashkenazi, G. Bella, et al. Data Scouting in ATLAS: Trigger, Tier0 and Analysis. Technical Report ATL-COM-GEN-2014-010, CERN, Geneva, Oct 2014.

[3] N. Anjos, S. Morais, J. Ricardo, et al. The ATLAS Jet Trigger for Initial LHC Run II. Technical Report ATL-COM-DAQ-2015-164, CERN, Geneva, Sep 2015.

[4] ATLAS Collaboration. Atlas data quality monitoring. `https://atlasdqm.web.cern.ch/atlasdqm/`.

[5] ATLAS Collaboration. JetVertexFraction: Selecting Jets in Pile-Pp Events using Jet-Vertex Association. `https://twiki.cern.ch/twiki/bin/view/Main/JetVertexFraction`.

[6] ATLAS Collaboration. Public liquid-argon calorimeter plots for collision data. `http://twiki.cern.ch/twiki/bin/view/AtlasPulblic/LArCaloPublicResults`.

[7] ATLAS Collaboration. Expected Performance of the ATLAS Experiment. CERN-OPEN-2008-020, 2008.

[8] ATLAS Collaboration. The ATLAS Experiment at the CERN Large Hadron Collider. *JINST*, 3, 2008.

[9] ATLAS Collaboration. Data-Quality Requirements and Event Cleaning for Jets and Missing Transverse Energy Reconstruction with the ATLAS Detector in Proton-Proton Collisions at a Center-of-Mass Energy of $\sqrt{s} = 7$ TeV. ATLAS-CONF-2010-038, 2010.

[10] ATLAS Collaboration. Readiness of the ATLAS Tile Calorimeter for LHC collisions, 2010.

[11] ATLAS Collaboration. Jet energy measurement with the ATLAS detector in proton-proton collisions at $\sqrt{s} = 7$ TeV. CERN-PH-EP-2011-191, 2013.

[12] ATLAS Collaboration. Pile-up subtraction and suppression for jets in ATLAS. ATLAS-CONF-2013-083, 2013.

[13] ATLAS Collaboration. Jet Calibration and Systematic Uncertainties for Jets Reconstructed in the ATLAS Detector at $\sqrt{s} = 13$ TeV. ATL-PHYS-PUB-2015-015, 2015.

[14] ATLAS Collaboration. Jet energy measurement and its systematic uncertainty in proton-proton collisions at $\sqrt{s} = 7$ TeVwith the ATLAS detector. CERN-PH-EP-2013-222, 2015.

[15] ATLAS Collaboration. Jet global sequential corrections with the ATLAS detector in proton-proton collisions at $\sqrt{s} = 8$ TeV. ATLAS-CONF-2015-002, 2015.

[16] ATLAS Collaboration. Monte Carlo Calibration of In-situ Measurements of Jet Energy Scale, Jet Energy Resolution and Jet Mass in ATLAS. ATLAS-CONF-2015-037, 2015.

[17] ATLAS Collaboration. Search for new phenomena in the dijet mass distribution using *pp* collision data at $\sqrt{s} = 8$ TeV with the ATLAS detector. *Phys. Rev. D*, 91:052007, Mar 2015.

[18] ATLAS Collaboration. Search for Light Dijet Resonances with the ATLAS Detector using a Trigger-object Level Analysis in LHC pp collisions at $\sqrt{s} = 13$ TeV. ATL-CONF-2016-030, 2016.

[19] C. Doglioni. *Measurement of the Inclusive Jet Cross Section with the ATLAS Detector at the Large Hadron Collider*. Springer Theses Recognizing Outstanding Ph.D. Research. Springer, 2012.

[20] M. Chala, F. Kahlhoefer, M. McCullough, et al. Constraining Dark Sectors with Monojets and Dijets. *JHEP*, 07:089, 2015.

[21] ATLAS Collaboration. Luminosity Public Results Run 2. `https://twiki.cern.ch/twiki/bin/view/AtlasPublic/LuminosityPublicResultsRun2`.

[22] D. Damazio, C. Wiglesworth. Hlt pile-up corrections. `https://indico.cern.ch/event/457180/contributions/1969237/attachments/1178080/1704355/TGM_281015.pdf`, October 2015.

[23] E. Halkiadakis. Introduction to the LHC Experiments. *ARXIV:1004.5564*, 2010.

[24] GEANT4 Collaboration. GEANT4. `http://geant4.cern.ch/index.shtml`.

[25] W. Lampl et al. Calorimeter Clustering Algorithms: Description and Performance. ATLAS-LARG-PUB-2008-002, 2008.

[26] G. Salam M. Cacciari and G. Soyez. Fastjet. `http://fastjet.fr`.

[27] M. Cacciari and G. Salam. The anti-$k_T$ jet clustering algorithm. *ARXIV:0802.1189*, February 2008.

[28] M. Thomson. *Modern Particle Physics*. Cambridge University Press, 2013.

[29] F. Müller. *Jet production measurements at the ATLAS experiment*. PhD thesis, Ruprect-Karls-Universität Heidelberg, 2013.

[30] J. Pequenao. Computer generated image of the atlas calorimeter, 2008, 2008.

[31] J. Pequenao. Computer generated image of the whole atlas detector, 2008, 2008.

[32] T. Sjostrand, S. Mrenna, and P. Skands. A Brief Introduction to PYTHIA 8.1. *Comput. Phys. Commun.*, 178:852–867, 2008.

[33] T. Akesson and J. Alison and B. Allen and others. Search for New Phenomena in Dijet Events with the ATLAS Detector at $\sqrt{s}$=13 TeV with the full 2015 dataset. Technical Report ATL-COM-PHYS-2015-1205, CERN, Geneva, Sep 2015.

[34] Wikipedia. Dark matter. `https://en.wikipedia.org/wiki/Dark_matter`.

# Appendix A

# Background Robustness Study With Respect To Scale Factors

In the 2015 TLA, resonances in the dijet mass spectrum are searched by estimating the standard model background with a global fit and comparing the fitted distribution with the recorded DS stream data. This approach can only lead to a discovery, if the background estimation is "robust". A robust background estimation ensures that:

1. If no new physic particles exist in data, no resonance is found.
2. If new physic particles exist in data, the background estimation is not biased by the resonance. By comparing data to the background estimation the resonance is found.

The background robustness study presented here belongs to the first criterion.
The TLA calibration scheme is still new, and even though the scheme is validated an additional test is done to ensure that a mis-calibration would not cause a fake resonance in the mass spectrum. The biggest deviation between the offline and TLA calibration scheme are the data derived scale factors, which calibrate HLT jet energy scale to offline jet energy scale. Hence, I tested whether the background estimation depends on scale factors.
In MC simulation, the HLT and offline jet energies are fairly comparable, and to apply the data derived scale factors to MC simulated HLT jets would result in 100% wrong energies. The mass spectrum of such calibrated HLT jets would be biased and hence a background estimation derived on this mass spectrum would represent a worst case scenario in TLA. If the global fit is able to fit this spectrum and the comparison between MC simulated data and the fitted background finds no significant peak, the background estimation is robust against wrongly derived scale factors.
First, the effect on the $m_{jj}$ distribution (and also other kinematic distributions) are studied. In Figure A.1 the MC simulated dijet mass spectrum with and without scale factors (SF) applied is shown. The scale factors mostly reduce HLT jet momenta and therefore the mass distribution with scale factors applied is shifted to a lower energetic region. The dijet-mass is underestimated. In the low-mass range (500 to 700 GeV) the mass is underestimated by 4 to 6% , and towards higher masses by 2%. This behavior reflects the behavior of the scale factors, which are larger at lower and smaller at higher $p_T$, and is therefore expected.

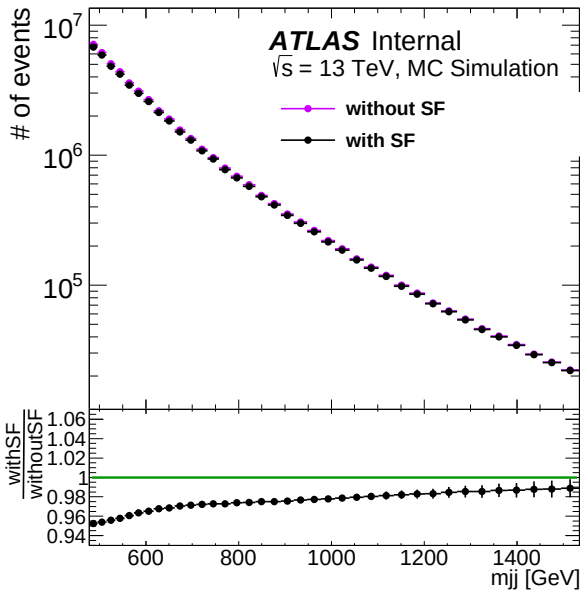


**Figure A.1:** Truth dijet mass distribution with (black) and without (pink) scale factors applied and their ratios.

The MC simulated mass spectra with and without scale factors applied are fitted and compared with the original spectrum. In Figure A.2 the results of the fit and the comparison is shown, on the left side for the mass spectrum without scale factors applied and on the right side with scale factors applied. The fit of the distribution with scale factors applied is worse than the one of the distribution without scale factors applied. A localized 3 bin excess is seen at low masses. The p-value, which indicates the likeliness that a deviation seen is caused by statistical fluctuations, worsen from 0.64 to 0.11. Though, for a significant peak, a p-value below 0.05 is needed. Therefore, no significant peak is induced by wrong scale factors.

The most problematic region regarding the agreement between HLT and offline jet energies is the transition region $1.4 < |\eta| < 1.6$. Hence, this region is regarded with large scale factors. To double check the influence of this region on the dijet-mass spectrum the test described above is redone with scale factors increased by 2% in the transition region. In Figure A.3 the mass distribution with the varied scale factors applied is shown. A maximal deviation around 7% is found at low-masses. In total, the masses are further underestimated by roughly 1% with respect to the mass spectrum with the normal scale factor applied.

The background estimation is shown in Figure A.4. The fit performance worsen and is visible in the likeliness that the seen excess between background estimation and origin mass spectrum is a statistical phenomena drops to 0.05. Still, the excess would not be interpreted as a new physics resonance. The background estimation is robust against wrongly derived scale factors.

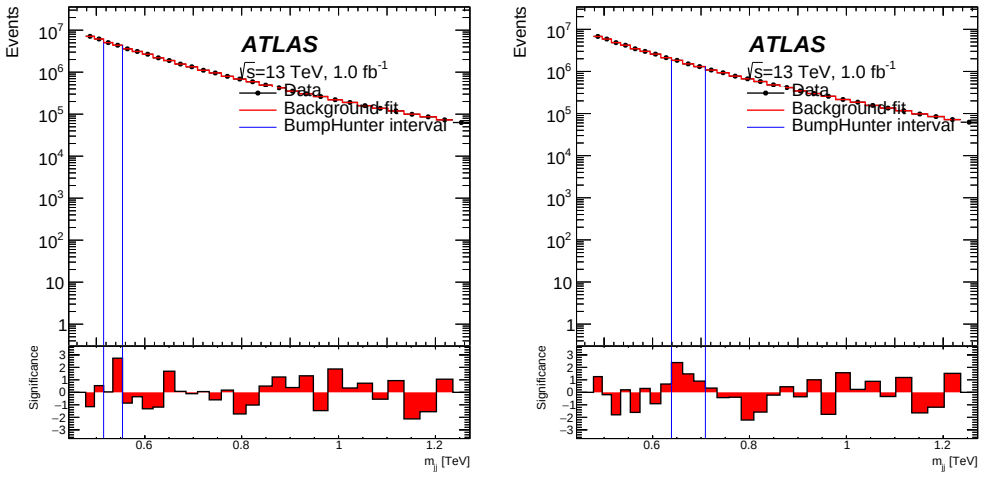


**Figure A.2:** Data like mass distribution generated with MC simulation. The distributions without scale factors applied (left) and with scale factors applied (right) are fitted by a 4 parameter function.

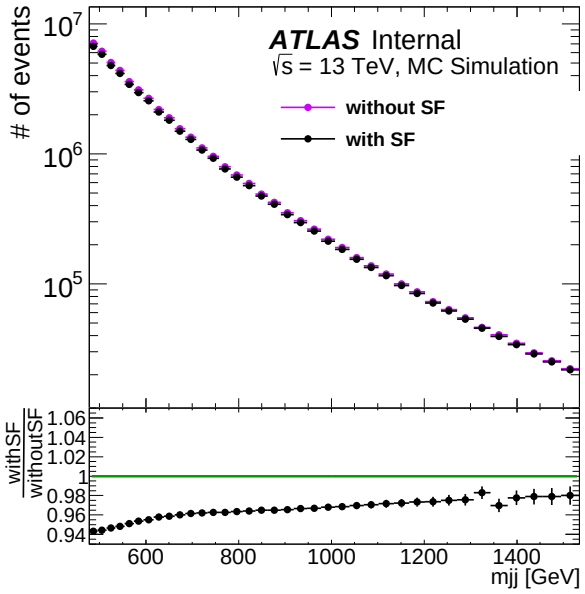


**Figure A.3:** Truth dijet mass distribution with varied (black) and without scale factors (pink) applied and their ratios.

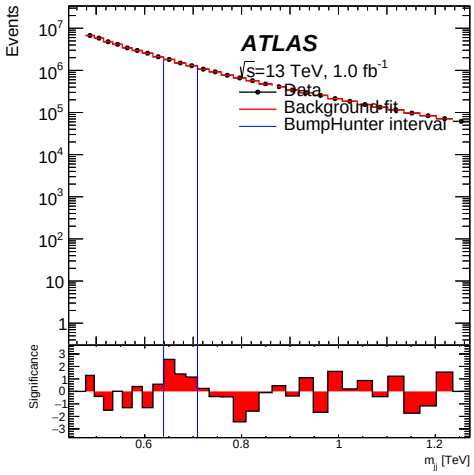


**Figure A.4:** Data like mass distribution generated with MC simulation. The distribution with varied scale factors applied is fitted by a 4 parameter function.

# Appendix B

# Kinematic Plots at EM Scale

In this Appendix additional kinematic distributions at EM scale are presented. All distributions are created with data representing period F and selected by HLT-j110 and by requiring a leading jet with $p_T > 150$ GeV. The different plots are supporting the discussion in section 7.2. The following distributions are shown:

1. leading jet $p_T$ distribution in different $\eta$ regions
2. angular separation $y^*$ distribution between leading and the subleading jet in different $\eta$ regions
3. inclusive $\eta$ distribution in different jet energy slices
4. inclusive $p_T$ distribution over all $\eta$ ranges in different jet energy slices
5. inclusive $p_T$ distribution in the central region in different jet energy slices
6. inclusive $p_T$ distribution in the middle region in different jet energy slices
7. inclusive $p_T$ distribution in the forward region in different jet energy slices
8. invariant mass $m_{jj}$ distributions over all $\eta$ regions in different jet energy slices

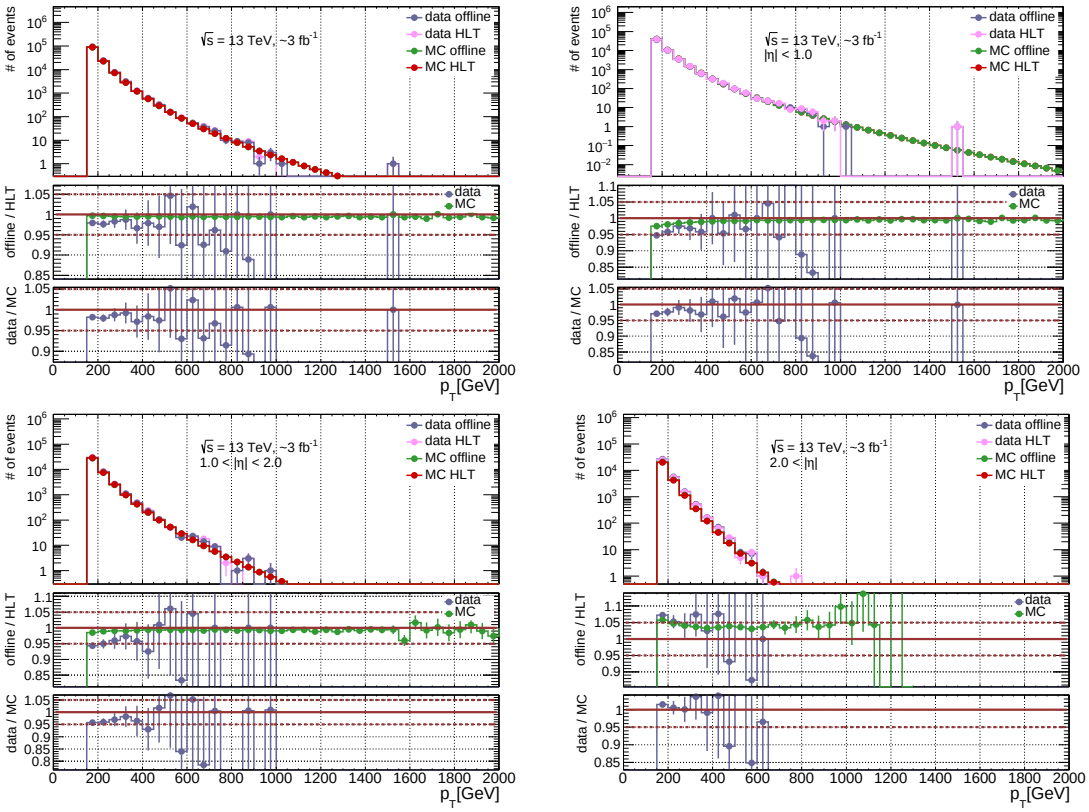


**Figure B.1:** Leading offline and HLT jet $p_T$ distribution for MC simulation and data and their ratios in $\eta$ regions at EM scale. Upper left plot contains jets inclusive over the total $\eta$ region, upper right plots contains jets in region $|\eta| < 1.0$, lower left plot contains jets in region $1.0 < |\eta| < 2.0$ and lower right plot contains jets in region $2.0 < |\eta|$. Events are selected with HLT-j110 and a leading jet $p_T$ requirement of at least 150 GeV. In each panel, the top plot presents the leading jet $p_T$ distributions in MC simulations (green - offline jets, red - HLT jets) and data (blue - offline jets, pink - HLT jets). The middle plots presents the offline-to-HLT ratio in MC simulations (green) and data (blue). The lowest plot presents the double ratio of the offline-to-HLT ratios in data and MC simulation.

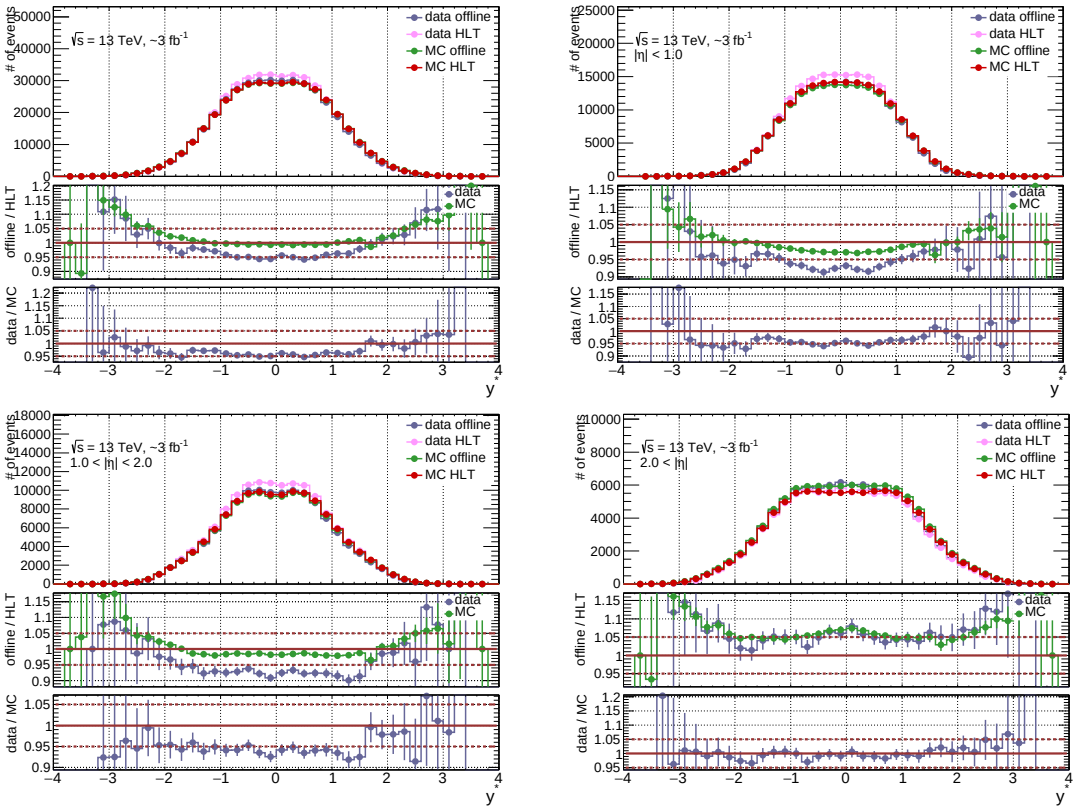


**Figure B.2:** Offline and HLT jet $y^*$ distribution for MC simulation and data and their ratios in different $\eta$ regions at EM scale. Upper left plot contains jets inclusive over the total $\eta$ region, upper right plots contains jets in region $|\eta| < 1.0$, lower left plot contains jets in region $1.0 < |\eta| < 2.0$ and lower right plot contains jets in region $2.0 < |\eta|$. Events are selected with HLT-j110 and a leading jet $p_T$ requirement of 150 GeV. In each panel, the top plot presents the $y^*$ distributions in MC simulation (green - offline jets, red - HLT jets) and data (blue - offline jets, pink - HLT jets). The middle plots presents the offline-to-HLT ratio in MC simulations (green) and data (blue). The lowest plot presents the double ratio of the offline-to-HLT ratios in data and MC simulation.

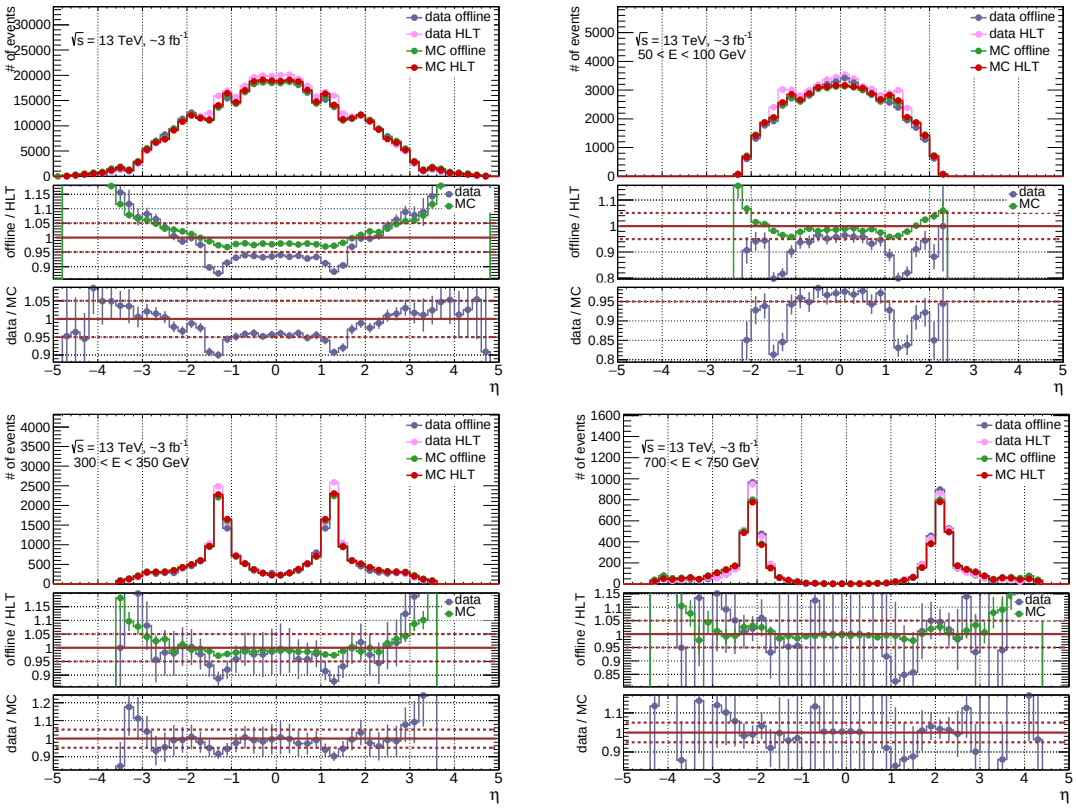


**Figure B.3:** Inclusive offline and HLT $\eta$ distribution for MC simulation and data and their ratios in different E slices at EM scale. Upper left plot contains jets with 0 GeV $> E$, upper right plots contains jets with $50 < E < 100$ GeV , lower left plot contains jets with $300 < E < 350$ GeV and lower right plot contains jets with $700 < E < 750$ GeV. Events are selected with HLT-j110 and a leading jet $p_T$ requirement of 150 GeV. In each panel, the top plot presents the jet $\eta$ distributions in MC simulation (green - offline jets, red - HLT jets), and data (blue - offline jets, pink - HLT jets). The middle plots presents the offline-to-HLT ratio in MC simulations (green) and data (blue). The lowest plot presents the double ratio of the offline-to-HLT ratios in data and MC simulation.

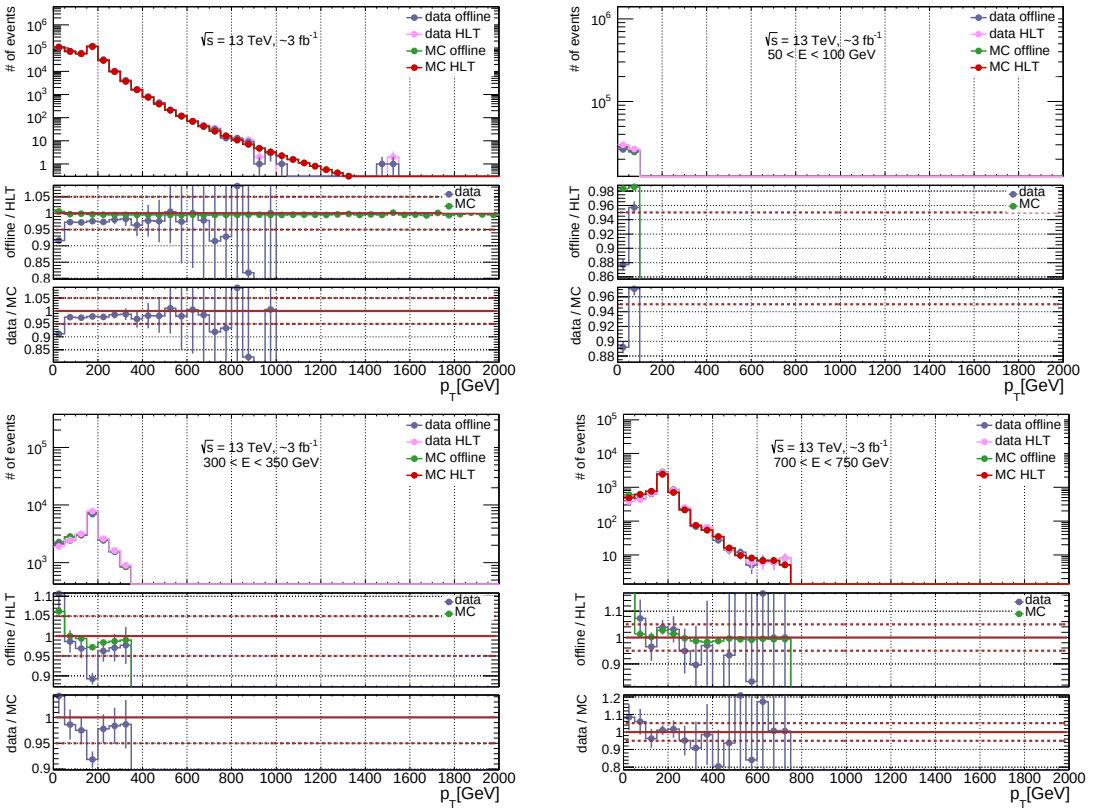


**Figure B.4:** Inclusive offline and HLT jet $p_T$ distribution for MC simulation and data and their ratios in different E slices at EM scale. Upper left plot contains jets with 0 GeV $> E$, upper right plots contains jets with $50 < E < 100$ GeV , lower left plot contains jets with $300 < E < 350$ GeV and lower right plot contains jets with $700 < E < 750$ GeV. Events are selected with HLT-j110 and a leading jet $p_T$ requirement of 150 GeV. In each panel, the top plot presents the jet $p_T$ distributions in MC simulations (green - offline jets, red - HLT jets), and data (blue - offline jets, pink - HLT jets). The middle plots presents the offline-to-HLT ratio in MC simulations (green) and data (blue). The lowest plot presents the double ratio of the offline-to-HLT ratios in data and MC simulation.

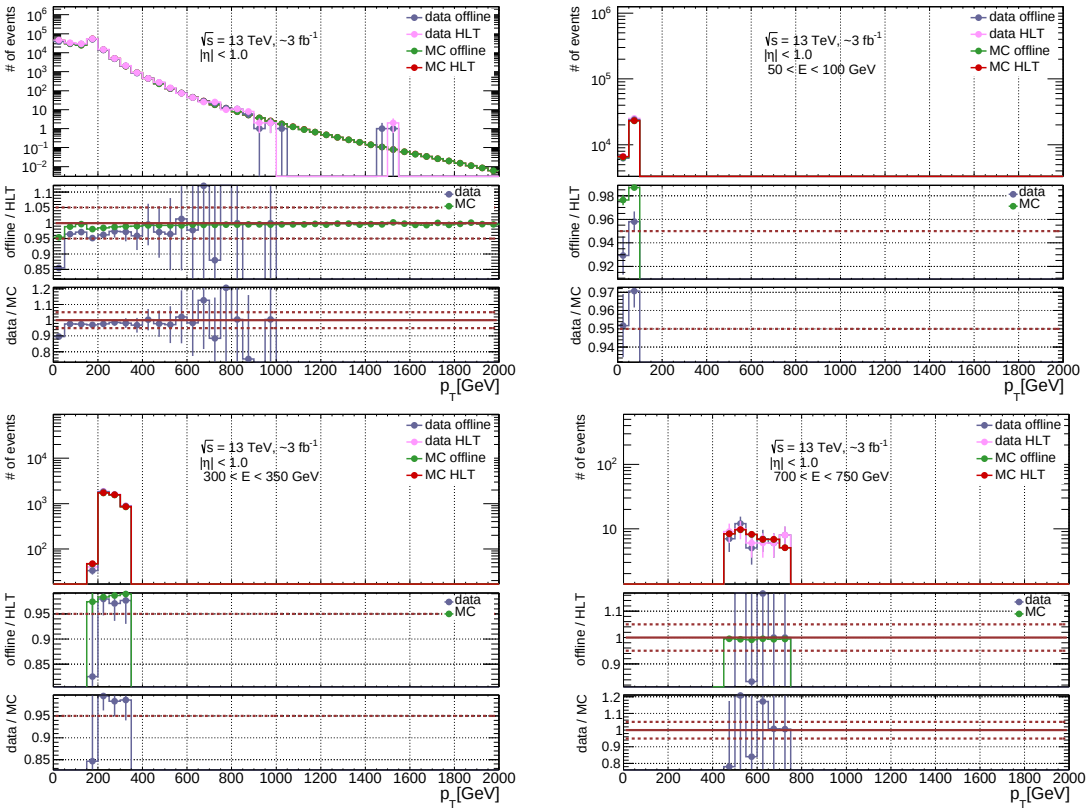


**Figure B.5:** Inclusive offline and HLT jet $p_T$ distributions in MC simulation and data and their ratios in E slices at EM scale. All jets are located in region $\eta < 1.0$. Upper left plot contains jets with 0 GeV $> E$, upper right plots contains jets with $50 < E < 100$ GeV , lower left plot contains jets with $300 < E < 350$ GeV and lower right plot contains jets with $700 < E < 750$ GeV. Events are selected with HLT-j110 and a leading jet $p_T$ requirement of 150 GeV. In each panel, the top plot presents the jet $p_T$ distributions in MC simulation (green - offline jets, red - HLT jets) and data (blue - offline jets, pink - HLT jets). The middle plots presents the offline-to-HLT ratio in MC simulation (green) and data (blue). The lowest plot presents the double ratio of the offline-to-HLT ratios in data and MC simulation.

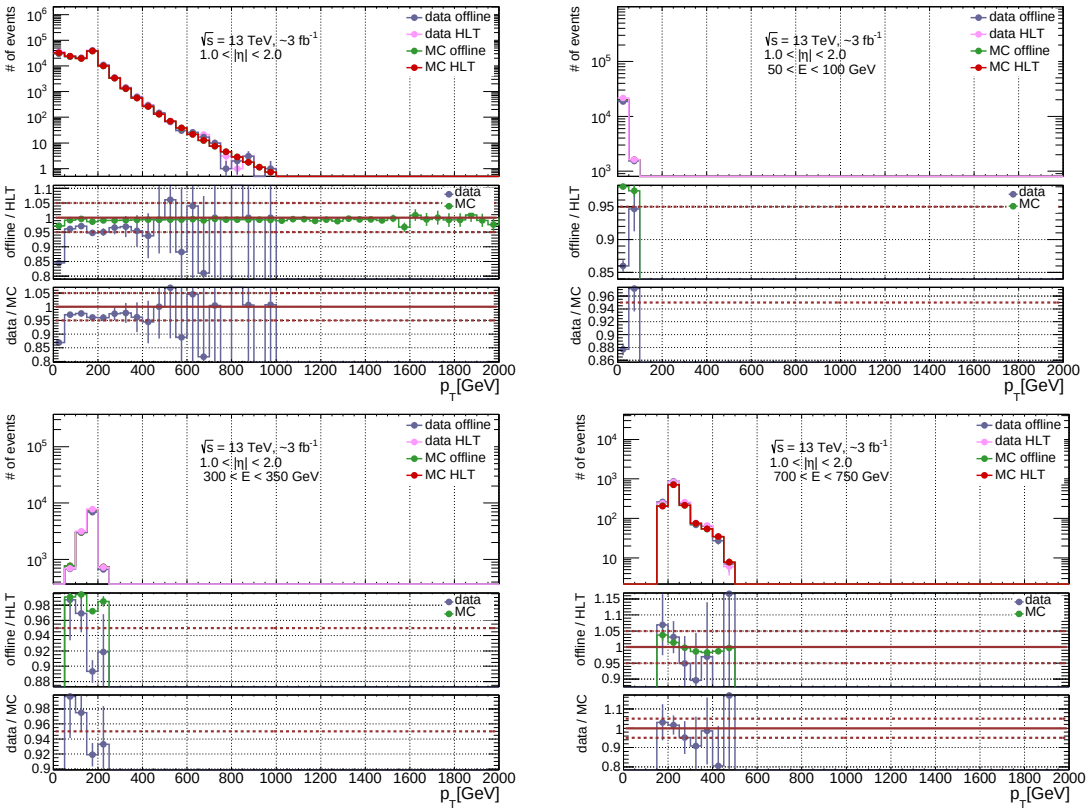


**Figure B.6:** Inclusive offline and HLT jet $p_T$ distributions in MC simulation and data and their ratios in different E slices at EM scale. All jets are located in region $1.0 < |\eta| < 2.0$. Upper left plot contains jets with 0 GeV $> E$, upper right plots contains jets with $50 < E < 100$ GeV , lower left plot contains jets with $300 < E < 350$ GeV and lower right plot contains jets with $700 < E < 750$ GeV. Events are selected with HLT-j110 and a leading jet $p_T$ requirement of 150 GeV. In each panel, the top plot presents the jet $p_T$ distributions in MC simulation (green - offline jets, red - HLT jets) and data (blue - offline jets, pink - HLT jets). The middle plots presents the offline-to-HLT ratio in MC simulation (green) and data (blue). The lowest plot presents the double ratio of the offline-to-HLT ratios in data and MC simulation.

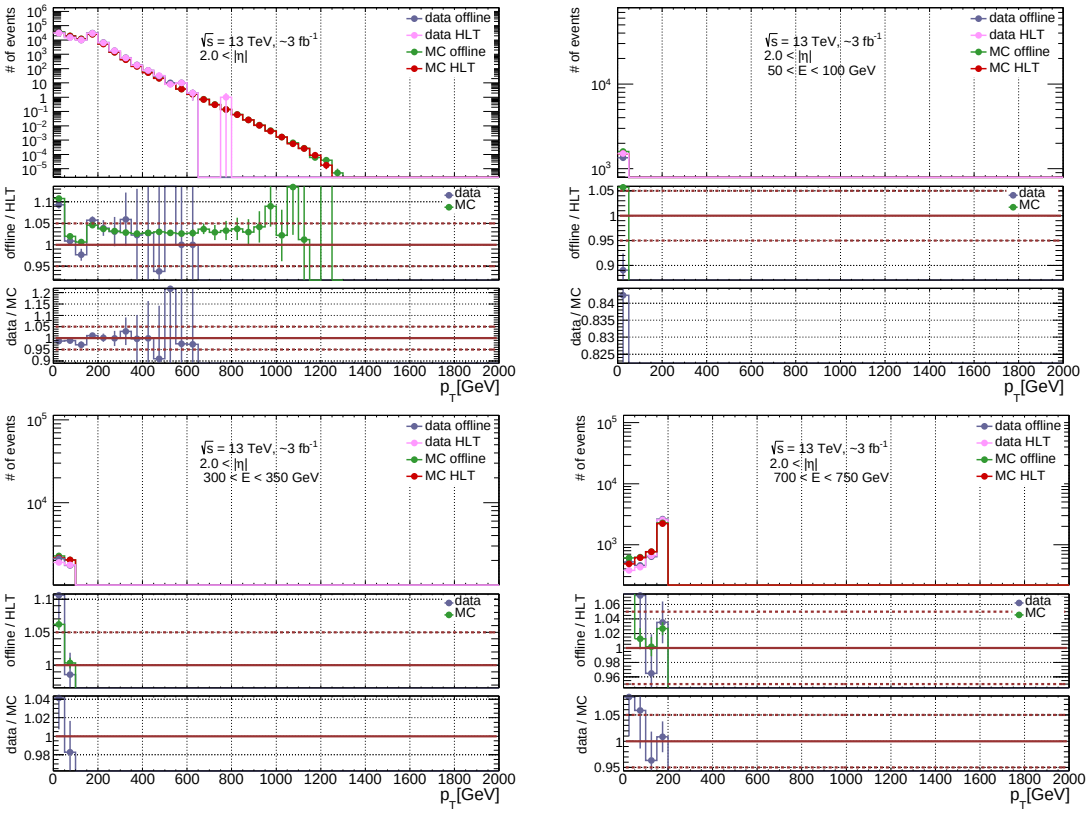


**Figure B.7:** Inclusive offline and HLT jet $p_T$ distributions in MC simulation and data and their ratios in different E-slices at EM scale. All jets are located in ragion $2.0 < |\eta|$. Upper left plot contains jets with 0 GeV $> E$, upper right plots contains jets with $50 < E < 100$ GeV , lower left plot contains jets with $300 < E < 350$ GeV and lower right plot contains jets with $700 < E < 750$ GeV. Events are selected with HLT-j110 and a leading jet $p_T$ requirement of 150 GeV. In each panel, the top plot presents the jet $p_T$ distributions in MC simulation (green - offline jets, red - HLT jets) and data (blue - offline jets, pink - HLT jets). The middle plots presents the offline-to-HLT ratio in MC simulation (green) and data (blue). The lowest plot presents the double ratio of the offline-to-HLT ratios in data and MC simulation.

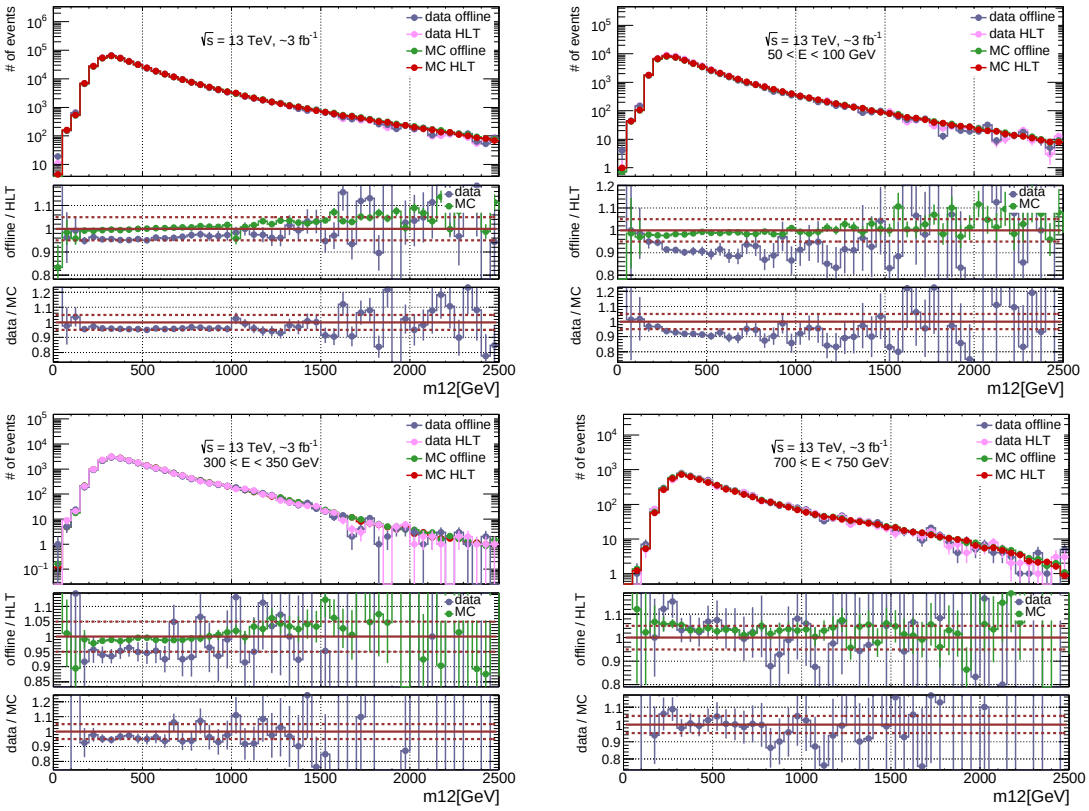


**Figure B.8:** Inclusive offline and jet HLT $m_{jj}$ distribution for MC simulation and data and their ratios in different E slices at EM scale. Upper left plot contains jets with 0 GeV $> E$, upper right plots contains jets with $50 < E < 100$ GeV , lower left plot contains jets with $300 < E < 350$ GeV and lower right plot contains jets with $700 < E < 750$ GeV. Events are selected with HLT-j110 and a leading jet $p_T$ cut of 150 GeV. In each panel, the top plot presents the jet $m_{jj}$ distributions in MC simulations (green - offline jets, red - HLT jets) and data (blue - offline jets, pink - HLT jets). The middle plots presents the offline-to-HLT ratio in MC simulation (green) and data (blue). The lowest plot presents the double ratio of the offline-to-HLT ratios in data and MC simulation.

# Appendix C

# Fitting Responses

The shape of jet response distributions depends on the jet momentum. In general, a peak in the distribution is observed, because the jets are matched and describe the same object. This peak represents the average difference in momentum or energy between the jets. The distribution also contains statistical fluctuations in the tail and these fluctuations can bias the mean of the distribution, which would no longer align with the peak observed. Therefore, response distributions are fitted around the peak with a truncate Gaussian distribution. In this Appendix a more detailed description of my fitting method is given.

I only fit response distributions with at least three events inside the fit range in three iterations. The range of the fits depends on the $p_T$ range the response distribution covers[1]: The shape of HLT jet response distributions with respect to offline jets vary for different $p_T$ ranges, as shown in Figure C.1. In a low-$p_T$ momentum range (55 to 116 GeV), the shape of the peak is more distorted due to additional pile-up jets. Only a small area around the peak can be described with a Gaussian distribution. At higher-$p_T$ ranges (e.g. $p_T > 400$ GeV) the peaks are more pronounced and cover enough bins. A wider range around the mean is chosen. Taken these into account, I chose to start the first iteration of fits for response distributions including jets with $p_T < 240$ GeV are fitted in a range $2.4 \times \sigma$ around the mean. Distributions including jets with $p_T > 240$ GeV are fitted in a range $3.0 \times \sigma$ around the distribution mean. For the second and third iteration, the fits are done around the mean of the preceeding Gaussian fit in a range $1.4 \times \sigma_{Gauss}$ and $2.0 \times \sigma_{Gauss}$ respectively for the different jet $p_T$ included in the distributions.

Before the first fit, the bin size of the response distribution is reevaluated. The bin size is optimized to a width in which the physical relevant structure of the response distributions are visible without being distorted by small statistical fluctuations. The optimal bin size is determined with

$$\frac{3.5RMS}{N^{-3}} \tag{C.1}$$

, where RMS is the root-mean square of the original distribution and N the number of events. The distributions are rearranged to match this criterion as good as possible. In cases with few events this criterion results in a rearrange distribution without a clear peak shape, even though before a peak was visible. Then, the fit fails or results in a fit with a chi2/NDF = $\infty$, with the

[1] The response distributions are calculated in different $p_T$ and $\eta$ bins.

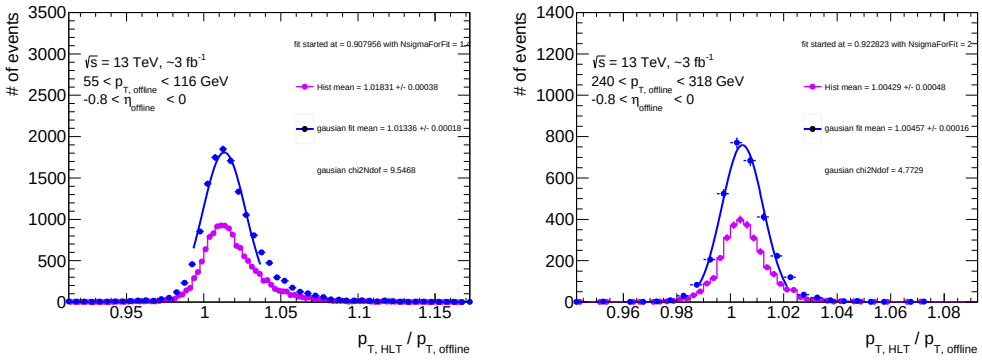


**Figure C.1:** Response distributions of jets within $0 < \eta < 0.8$ and $55 < p_T < 116$ GeV (left) and $240 < p_T < 318$ GeV (right). The original histogram is drawn in purple, while the fit result and rearranged distribution for the fit is shown in blue. HLT and offline jets are calibrated to their respective EM scale. They are matched within $\Delta R < 0.4$. All events passed the `HLT-j110` trigger and contain leading jets with $p_T$ of at least 150 GeV.

number of degrees of freedom NDF. Fits with such a chi2/NDF are redone, but without rearranging the original response distribution. If the fit still fails or results in a chi2/NDF $= \infty$, no mean response value is accounted to the respective $p_T$ and $\eta$ range of the response distribution. No further requirement on the chi2/NDF is set as the distribution fitted are not Gaussian like due to statistical fluctuations. Still, a fit result is discarded, if the fit precision, which is measured with the Gaussian mean error divided by the Gaussian mean, is worse than 0.8% .

The criteria chosen are not excluding all fits of poor quality, but a stricter selection would remove too many usable results. This compromise is chosen to have a stable fit of mostly good quality, especially as even poor quality fits can refer to a reasonable mean. Only in one or two high-momentum ranges (e.g. 642 to 786 GeV) the fits of the response distribution results in an unreliable Gaussian mean as cross checks with the mean of the original distribution indicate. In these cases the Gaussian mean is a few percent different than in adjacent ranges, and therefore visible. As the response distribution fits are used for validation tests of the calibration schemes, the quality criteria chosen are sufficient.

**Acknowledgements**

This last year, I had the great pleasure of working in an interesting and amazingly nice analysis group, the TLA, while surrounded by friends and colleagues in Heidelberg. For this great opportunity, I want to thank my supervisors:
Many thanks to Dr. Monica Dunford, who while experience a very exciting year herself, still found the time to advise and support me. Thank you for taking care of me and introducing me to the TLA.
Many thanks to Pavel Starovoitov, for always offering advice and explaining topics patiently. Thank you, especially for the last few weeks for proof reading this thesis.
Many thanks to Dr. Caterina Doglionio, for always being reachable via mail, Skype or Slack, and explaining and discussing my results or general analysis questions with so much enthusiasm with me.
For the great atmosphere over this year and for the fun while working (which can sometimes be quite frustrating, if a bug pops up):
Many thanks to the TLA-group members - I have felt very welcomed in this group, and working with you all was an interesting, challenging and fun experience.
Many thanks to my office mates Hanno, Stanislav, Claire and Sebastian, who all had to suffer my moods and my loud music in the office. Thank you for being around, it was fun!
Many thanks to the Heidelberg ATLAS group of Dr. Prof. Schultz-Coulon, who took me in for this year. You are great! I feel very comfortable here, valued and included. Thank you for this great year. Many thanks to Valerie, Julia, Jan and Hanno for proof reading, and simply because you are who you are.
Last but not least, many thanks to all my friends and family - inside and outside the Heidelberg group. I hope you all know that I value each of you very much.

You all took great care of me and helped me creating this thesis. Thank you so much!

Erklärung:

Ich versichere, dass ich diese Arbeit selbstständig verfasst habe und keine anderen als die angegebenen Quellen und Hilfsmittel benutzt habe.

Heidelberg, den 02.02.2017 .....